UNIVERSITY OF OTTAWA
M.A.SC. THESIS

Designing Subwavelength Grating Devices for the AlGaAs-on-insulator Platform

Author:
Fatemeh Sadat MOUSAVI KARIMI

Supervisor:
Prof. Ksenia DOLGALEVA

Thesis submitted to the University of Ottawa in partial fulfillment of the requirements for the Master of Applied Science in Electrical and Computer Engineering



Ottawa-Carleton Institute for Electrical and Computer Engineering
Faculty of Engineering
University of Ottawa

© Fatemeh Sadat Mousavi Karimi, Ottawa, Canada, 2026

Abstract

The first demonstration of subwavelength grating (SWG) waveguides on the silicon-on-insulator (SOI) platform has led to the emergence of several SWG devices in silicon photonics. These devices, which include waveguides, couplers, sensors, and ring resonators to name a few, leverage the refractive index and dispersion engineering inherent to SWG waveguides to enhance their performance. Despite the demonstrated success of SWG waveguides in silicon photonics, these engineering techniques have yet to be widely used in combination with III-V semiconductors which are already extensively used for laser sources and nonlinear applications. Thus, the focus of this study is using aluminum gallium arsenide on insulator (AlGaAs-OI) to design subwavelength grating devices.

In this thesis, I present the design and computational simulation of subwavelength grating photonic components utilizing the $Al_{0.18}Ga_{0.82}As$-OI platform, while also reporting on nonlinear optical experiments conducted with novel Huygens' meta-waveguide SOI resonators. The effective medium theory, Finite-Difference Eigenmode (FDE), and Finite-Difference Time-Domain (FDTD) methods were used for calculating the photonic band-structure and dispersion characteristics of the SWG unit-cells. Using these methods, low-loss SWG waveguides were optimized for different core heights and cladding materials, achieving Floquet-Bloch mode propagation with minimal to no back-scattering. Building upon these waveguides, and by exploiting the refractive index engineering inherent to SWG structures, an ultra-compact 30 μm-long fiber-to-chip AlGaAs-OI SWG edge coupler was designed with a peak coupling efficiency of 90.2% (-0.45 dB loss) at 1550 nm for quasi-TE modes. Furthermore, AlGaAs-OI SWG microring resonators were investigated, demonstrating that a hybrid SWG-bus/solid-core ring geometry can leverage mode delocalization to relax coupling gaps while maintaining sufficient coupling and a high quality factor ($Q > 75,000$) at 1550 nm. Finally, I report the first physical observation of stimulated four-wave mixing (FWM) in a prefabricated SOI Huygens' meta-waveguide microring resonator. This work highlights the potential of AlGaAs-OI subwavelength engineered structures as promising building blocks for monolithically integrated, low-loss, and highly efficient linear and nonlinear photonic integrated circuits.

Acknowledgements

In the name of God, the Most gracious, the Most Merciful.

First and foremost, I would like to thank my supervisor Prof. Ksenia Dolgaleva for her support and guidance, and for giving me the opportunity to work on such an interesting project. I would also like to thank all of the Nonlinear Photonics Group members for our discussions and enlightening discourse, with special thanks to Dr. Gabriel Flizikowski and Garen Simpson. I would also like to thank Dr. Flizikowski for his help with the four-wave mixing experiments discussed in Chapter 5, and for providing the linear characterization data for the devices under study. I would also like to thank our collaborators at the National Research Council (NRC): Dr. Pavel Cheben and Dr. Jens Schmid for their helpful comments and guidance, and Dr. Jianhao Zhang for his help with the SWG ring resonator simulations.

Finally, I wish to thank my family. I am profoundly grateful to my husband for being my steadfast support and keeping me grounded throughout this journey. I am equally grateful to my parents for their unwavering belief in me, and for instilling a lifelong curiosity for the sciences and learning as a whole.

Contents

Abstract ii

Acknowledgements iii

1 Introduction 1
- 1.1 Motivation . . . 1
- 1.2 Nonlinear Optics in a Nutshell . . . 3
- 1.3 Waveguide Optics . . . 8
- 1.4 Fundamental Photonic Components . . . 16
  - 1.4.1 Waveguide Geometries . . . 16
  - 1.4.2 Optical Couplers . . . 17
    - Directional couplers . . . 18
    - Edge couplers . . . 19
  - 1.4.3 Ring Resonators . . . 20
- 1.5 III-V Semiconductors . . . 23
- 1.6 Meta-waveguide Structures . . . 26
  - 1.6.1 Background Theory . . . 26
    - Bragg Regime . . . 28
    - Radiation Regime . . . 29
    - Subwavelength Regime . . . 29
  - 1.6.2 Enhancements in Silicon Photonics . . . 30
    - SWG Couplers . . . 30
    - SWG Ring-resonators . . . 32
    - SWG Beam Splitters . . . 33
- 1.7 Application of III-V Semiconductors in Optical Signal Processing 34
  - 1.7.1 Nonlinear Ring Resonators . . . 34
  - 1.7.2 Wavelength Conversion and Amplification . . . 36
  - 1.7.3 Optical Modulation . . . 37
  - 1.7.4 Logic Gates . . . 38
- 1.8 Thesis Outline . . . 40

2 AlGaAs-OI Subwavelength Grating Waveguides **41**
2.1 Methodology . . . 41
2.1.1 Software and Hardware Resources . . . 41
Material Fit . . . 42
Boundary Conditions . . . 44
Convergence Testing . . . 45
2.1.2 2D Modal Analysis . . . 46
2.1.3 Photonic Band-structure Calculation . . . 49
2.2 Design and Simulation Results . . . 50

3 AlGaAs-OI Subwavelength Grating Edge Coupler **54**

4 AlGaAs-OI Subwavelength Grating Ring Resonators **61**
4.1 Design Methodology . . . 62
4.2 Design and Simulation Results . . . 67
4.2.1 Observing Different Coupling Regimes . . . 67
4.2.2 High-Q SWG AlGaAs-OI Ring Resonator . . . 71

5 Four-Wave Mixing in Silicon-OI Huygens' Microring Resonators **74**
5.1 Devices Under Study . . . 75
5.2 Experimental Setup and Results . . . 77

6 Conclusions and Future Work **84**

Bibliography **87**

List of Figures

1.1 Energy level diagrams for (a) non-degenerate and (b) degenerate four-wave mixing. Simplified illustration of (c) non-degenerate and (d) degenerate four-wave mixing processes. 4
1.2 Frequency combs have equally spaced spectral components, but the magnitude of each spectral component can be very different. . 5
1.3 Schematic energy level diagram of two-photon absorption. 6
1.4 Energy level diagram for (a) SHG, (b) SFG, and (c) DFG. 7
1.5 A simple planar dielectric waveguide illustrating wave propagation through total internal reflection ($n_{core} > n_{clad}$). 8
1.6 1D planar dielectric waveguide where the core dimension along x is finite while it expands infinitely in the y and z directions. 9
1.7 1D planar dielectric waveguide even and odd modes. Adapted from [14]. 11
1.8 Example of a channel waveguide where the guided light is confined in the transverse (x and y) dimensions, surrounded by a lower index bottom cladding and air, while it can freely propagate in the z direction. The light is effectively "channeled" through the core layer of the dielectric medium. 13
1.9 Transverse electric field mode profiles for the 1D slab waveguide ((a), (c), (e), (g)) and 2D channel waveguide ((b), (d), (f), (h)) calculated using the Lumerical FDE solver. 14
1.10 Common waveguide geometries: (a) strip, (b) embedded strip, (c) buried, (d) rib/ridge, (e) strip-loaded. 16
1.11 A simple co-directional coupler. 18
1.12 Example of the transverse electric field profile of (a) symmetric and (b) anti-symmetric supermodes of a coupled-waveguide system. 19
1.13 A simple edge coupler realized through an inverse taper. 20
1.14 (a) Simple ring resonator with two bus waveguides. (b) Illustration of a ring resonator transmission spectrum with equally spaced frequency components. 21

1.15 Energy-momentum band diagrams of (a) direct and (b) indirect semiconductors. . . . 24
1.16 Structure of a simple periodic waveguide in 2D. The hashed filling indicates the cladding layer. . . . 27
1.17 Waveguide dispersion relations in different regions of operation. Adapted with permission from [9] © Optical Society of America. . . 28
1.18 (a) SEM image of SWG coupler. (b) Low-confinement section. (c) High-confinement section. (d) Intermediate section. Reprinted with permission from [26] © Optical Society of America. . . . 31
1.19 Schematic illustration of SWG ring resonator. Adapted with permission from [9] © Optical Society of America. . . . 32
1.20 SEM image of a fabricated ultra-broadband SWG MMI. Source: [32] . . . 34
1.21 Schematic illustration for frequency comb generation in a microring resonator. Source: [7] . . . 35
1.22 Basic principle of an optical logical AND gate. . . . 38

2.1 Multi-coefficient model fit to our analytical $Al_{0.18}Ga_{0.82}As$ data in Ansys Lumerical. . . . 44
2.2 The effect of increasing cross-sectional mesh size on (a) mode effective index and (b) group index at 1550 nm using the FDE Lumerical solver. . . . 46
2.3 The effect of increasing number of PML layers in FDTD simulation for AlGaAs SWG waveguides. . . . 46
2.4 The effect of increasing mesh accuracy in FDTD simulation settings for the AlGaAs SWG waveguides. . . . 47
2.5 Schematic 2D cross-section of the SWG waveguide . . . 47
2.6 The parameter sweep results for the group effective index, mode effective index and the effective mode area when the duty cycle is 70% and 80%. The waveguide height for these simulations is 200 nm and the upper cladding is silica. . . . 48
2.7 The (a) unit cell of an SWG waveguide and (b) its simulated photonic band-structure. . . . 49
2.8 The effect of varying either the a)-d) pitch or e)-h) duty cycle . . . 50
2.9 The mode profile of the excited Bloch mode at 1550 nm at the centre of the unit cell shown in Fig. 2.7. The colourbar represents the electric field magnitude in arbitrary units. . . . 51
2.10 Bloch mode propagation in four different SWG waveguide designs. 52

3.1 A simplified illustration of an SWG edge coupler and input fiber. 54
3.2 The fiber-to-chip edge coupler can be designed in two parts: one dedicated to the taper region at the tip and one for the taper section that fully transitions the inputted mode into the integrated waveguide at the coupler output. 56
3.3 The fiber to coupler tip mode overlap calculated using Lumerical FDE and the effective medium theory approximation. The duty cycles are represented by different coloured curves. 57
3.4 The calculated modal overlap between the fiber and edge coupler tip for both TE and TM modes as a function of fiber misalignment. 58
3.5 Schematic showing the parameters used in the different segments of the edge coupler design. 58
3.6 The final results for the a) forward field propagation simulation for the fundamental TE mode of the fiber entering the nanowaveguide via the edge coupler at 1550 nm and b) the coupler efficiency as a function of wavelength. 60
3.7 The results for the a) forward field propagation of the fiber's fundamental TM mode entering the nanowaveguide via the edge coupler at 1550 nm and b) the coupler efficiency as a function of wavelength. 60

4.1 Simple illustration of two possible scenarios for SWG ring resonator designs where (a) only the bus waveguides are SWG or (b) the full device uses SWG structures. 61
4.2 Diagram of a ring resonator. Source: Adapted from [16] 62
4.3 The coupling region in the (a) FDE and (b) FDTD simulation environments. The (c) symmetric and (d) anti-symmetric supermodes of the coupled system with a SWG duty cycle of 0.8 showcases stronger coupling at a gap of 350 nm compared to the (e) symmetric and (f) anti-symmetric modes of the solid-core system. 64
4.4 The theoretical cross-coupling coefficient for a ring and bus waveguide that are both SWG with a 0.8 duty cycle ratio and 200 nm period for a wavelength of 1550 nm. 65
4.5 (a) Total bend loss calculations from 2D MODE simulations. The total loss is calculated from adding the mode mismatch losses from entering and exiting the bent waveguide with the radiative losses from propagating in the bend. Each curve corresponds to a different duty cycle. (b) Bend losses for an 80% duty cycle. 66

4.6 The transmission spectrum as observed at the through port of the SWG ring resonators with varying coupling gaps. 69
4.7 The (a) structure of the high-Q AlGaAs-OI SWG ring resonator and (b) its transmission spectrum observed at the through port. . 73

5.1 Example layout files for the fabricated ring resonators under study. 76
5.2 The geometry of the Huygens' and SWG structures used in the ring resonators under study. 76
5.3 Transmission Spectra at the through port of ring resonators with different coupling gap sizes. 78
5.4 Transmission Spectra of the two devices used for FWM measurements. 79
5.5 A simplified illustration of the experimental setup used for the FWM measurements. 79
5.6 FWM measurement results. 81
5.7 Both edges of the chip have edge couplers (EC) that couple into or out of a solid silicon waveguide section. The solid-core waveguides are connected to the Huygens' meta-waveguide (HMW) through mode-converters (MC). 82

List of Tables

1.1 Comparison of popular nonlinear photonic integrated platforms . 25
1.2 Data Rates for Signal Processing Devices 39

2.1 Summary of the AlGaAs-on-insulator SWG Waveguide designs . 53

3.1 Summary of the AlGaAs-OI SWG edge coupler design parameters 59

4.1 Performance of simulated AlGaAs-OI microring resonators with different gap sizes around 1550 nm 68
4.2 Results for the small gap size simulated with finer mesh settings . 68

List of Abbreviations

AlAs	**A**luminium **A**rsenide
AlGaAs	**A**luminium **G**allium **A**rsenide
AlGaAs-OI	**A**luminium **G**allium **A**rsenide-**o**n-**I**nsulator
CMOS	**C**omplementary **M**etal-**O**xide-**S**emiconductor
CW	**C**ontinuous-**W**ave
DFG	**D**ifference-**F**requency **G**eneration
DSP	**D**igital **S**ignal **P**rocessing
EAM	**E**lectro-**A**bsorption **M**odulator
EDFA	**E**rbium-**D**oped **F**iber **A**mplifier
EMT	**E**ffective **M**edium **T**heory
EOM	**E**lectro-**O**ptic **M**odulator
FCA	**F**ree-**C**arrier **A**bsorption
FDE	**F**inite-**D**ifference **E**igenmode
FDTD	**F**inite-**D**ifference **T**ime-**D**omain
FSR	**F**ree **S**pectral **R**ange
FWHM	**F**ull **W**idth at **H**alf **M**aximum
FWM	**F**our-**W**ave **M**ixing
GaAs	**G**allium **A**rsenide
GVD	**G**roup **V**elocity **D**ispersion
HWP	**H**alf-**W**ave **P**late
InGaAsP	**I**ndium **G**allium **A**rsenide **P**hosphide
InP	**I**ndium **P**hosphide
IR	**I**nfra**r**ed
$LiNbO_3$	**L**ithium **N**iobate
MFD	**M**ode **F**ield **D**iameter
MMI	**M**ulti-**M**ode **I**nterference
MRR	**M**icroring **R**esonator
MZI	**M**ach–**Z**ehnder **I**nterferometer
NLSE	**N**onlinear **S**chrödinger **E**quation
NRC	**N**ational **R**esearch **C**ouncil (Canada)
OEO	**O**ptical-to-**E**lectrical-to-**O**ptical
OOK	**O**n-**O**ff **K**eying
OPA	**O**ptical **P**arametric **A**mplifier
OSA	**O**ptical **S**pectrum **A**nalyzer
PAM	**P**ulse-**A**mplitude **M**odulation
PEC	**P**erfect **E**lectrical **C**onductor
PIC	**P**hotonic **I**ntegrated **C**ircuit
PML	**P**erfectly **M**atched **L**ayer
Q	**Q**uality factor

QAM	**Q**uadrature **A**mplitude **M**odulation
RAMZI	**R**ing-**A**ssisted **M**ach–**Z**ehnder **I**nterferometer
RF	**R**adio **F**requency
RZ-OOK	**R**eturn-to-**Z**ero **O**n-**O**ff **K**eying
SDM	**S**pace-**D**ivision **M**ultiplexing
SFG	**S**um-**F**requency **G**eneration
SHG	**S**econd-**H**armonic **G**eneration
Si	**S**ilicon
Si_3N_4	**S**ilicon **N**itride
SiO_2	**S**ilicon **D**ioxide
SMF	**S**ingle-**M**ode **F**iber
SOA	**S**emiconductor **O**ptical **A**mplifier
SOI	**S**ilicon-**o**n-**I**nsulator
SPM	**S**elf-**P**hase **M**odulation
SWG	**S**ubwavelength **G**rating
TE	**T**ransverse **E**lectric
THG	**T**hird-**H**armonic **G**eneration
TIR	**T**otal **I**nternal **R**eflection
TM	**T**ransverse **M**agnetic
TPA	**T**wo-**P**hoton **A**bsorption
UHNA	**U**ltra-**H**igh **N**umerical **A**perture
UNI	**U**ltrafast **N**onlinear **I**nterferometer
UV	**U**ltra**v**iolet
WDM	**W**avelength-**D**ivision **M**ultiplexing

Dedicated to my beloved husband and family.

&

In loving memory of my cousin, my soul sister, whose flame was extinguished far too soon.

Chapter 1

Introduction

1.1 Motivation

In the current digital age, almost all aspects of human life rely on the transmission of information and the Internet. In the past decades, we have seen the great impact of using optical communication systems in the telecommunications industry, giving us access to faster Internet speeds and larger bandwidths [1]. However, with the increasing use of cloud computing, artificial intelligence, and high-definition video transmission, our need for higher bandwidths is constantly increasing [2]. The current optical communication networks make use of both optics and electronics as most of the signal processing is still done in the electrical domain, which means many optical-to-electrical-and-back-to-optical (OEO) converters are required in the system. This also means the transmission speed and bandwidth of our optical communication system are limited by the bandwidth of the electronics that do our signal processing. As such, one major area of research in the integrated photonics industry is the development of photonic integrated circuits (PICs) and devices that can perform signal processing in the optical domain, and thus eliminate the need for OEO converters and other intermediary electronics by using all-optical signal processing [3].

Signal processing operations commonly require the conversion of frequencies, which means the integrated photonics devices used for signal manipulation should have a strong nonlinear optical response. One of the very first materials researched extensively for integrated photonics was silicon [4], [5]. Since this semiconductor is commonly used in the technology industry for transistors and integrated chips, it has the advantage of a low-cost and well-established fabrication method, and easier integration with electronic components on the same circuit. However, a major disadvantage of silicon is its indirect bandgap, which makes it difficult to use as a material for laser sources. This means that silicon-based photonic circuits would require the integration of other materials which have a direct bandgap, such as III-V semiconductors. This makes the

photonic integrated circuits more complicated and costly, and gives rise to compatibility issues; it is therefore more desirable to use a material which can be used for any optical component required in an all-optical signal processing circuit.

III-V semiconductors are one such group of materials currently being researched for this purpose [6]. One promising compound within this family is aluminum gallium arsenide (AlGaAs), which has both strong second-order and third-order optical nonlinearity while boasting negligible two-photon absorption (TPA) in the telecommunication C-band [7], [8]. To be a good candidate for an all-optical signal processing circuit, the material should perform well in both the linear and nonlinear optical regimes while also having flexibility regarding optical response parameters, such as the refractive index. One method of manipulating the refractive index without a change of material platform is through subwavelength engineering [9].

Miniaturization is yet another important feature when designing PICs used for several applications, such as telecommunication, because it reduces the amount of required space and material. Subwavelength meta-material engineering is a technique that has been extensively used for silicon photonics in the past years and has proven itself to be advantageous for both device compactness and efficiency [9]. One emerging area in this field is the creation of highly transmissive Huygens' meta-waveguides, which are achieved by engineering Mie-resonant modes using periodically structured waveguides [9].

In this thesis, I design several essential photonic components such as waveguides, couplers, and micro-ring resonators using subwavelength grating (SWG) structures and the AlGaAs-on-insulator platform. These designs are verified through simulations and computational analysis. The motivation of this master's project is to combine the benefits and dispersion engineering of subwavelength grating structures with the advantages of AlGaAs to design fundamental building blocks for integrated photonic circuits. The refractive index engineering inherent to subwavelength structures and III-V compounds can be leveraged for the pursuit of monolithically integrated circuits where the active components, passive devices, and nonlinear processes can all be realized with the same material platform. This work also aims to fill a research gap regarding the use of III-V material for SWG devices.

In addition to the computational work on AlGaAs-OI, this thesis also includes physical nonlinear experiments demonstrating four-wave mixing (FWM) in prefabricated silicon-on-insulator (SOI) Huygens' meta-waveguide ring resonators. Since the fabrication of III-V devices is currently a more involved process that

requires in-house fabrication reliant on university cleanroom availabilities, this thesis only includes experimental demonstrations for prefabricated SOI devices.

The remaining sections of this introductory chapter provide a brief theoretical background on the related concepts, such as a general overview of nonlinear optics and waveguiding principles, followed by the working principles of fundamental photonic components used in this study. The fundamental theory behind periodic waveguides and subwavelength engineering is also concisely explained. I argue for my choice of material platform, AlGaAs-on-insulator, by explaining its advantages and comparing it with other popular materials used in photonics. Some demonstrated applications of III-V semiconductors for optical signal processing applications are also provided as further motivation for my material choice.

1.2 Nonlinear Optics in a Nutshell

One major reason for the use of III-V semiconductors in this project is their attractive nonlinear optical properties which make them compatible with all-optical signal processing applications. Signal processing in communication systems encompasses many tasks and functions, and several of them involve wavelength conversion. Due to the need for wavelength manipulation, optical signal processing will inherently rely on nonlinear optics. A beam of light cannot gain any new frequency components by going through a medium operating in the linear optical regime. Its spectrum will either remain unchanged, or it will actually lose frequency components if the material has absorption losses due to atomic excitations [10].

The main difference between linear and nonlinear optics is in the intensity of light that is being used. At low optical intensities, the interacting medium's induced polarization, $\mathbf{P}$, is related to the incident beam's electric field, $\mathbf{E}$, in a linear fashion:

$$\mathbf{P} = \epsilon_0 \chi \mathbf{E}, \tag{1.1}$$

where χ is the material's linear electric susceptibility and ϵ_0 is the dielectric permittivity of vacuum. At high optical intensities, the nonlinear terms in the material response can no longer be neglected and the induced polarization is expanded with respect to the electric field according to

$$\mathbf{P} = \epsilon_0 \chi^{(1)} \mathbf{E} + \epsilon_0 \chi^{(2)} \mathbf{E}^2 + \epsilon_0 \chi^{(3)} \mathbf{E}^3 + ..., \tag{1.2}$$

where $\chi^{(2)}$ is the second-order susceptibility and $\chi^{(3)}$ is the third-order susceptibility of the material [10]. These coefficients describe the nonlinear properties of the material and how strong or weak their responses are for second-order and third-order nonlinear processes.

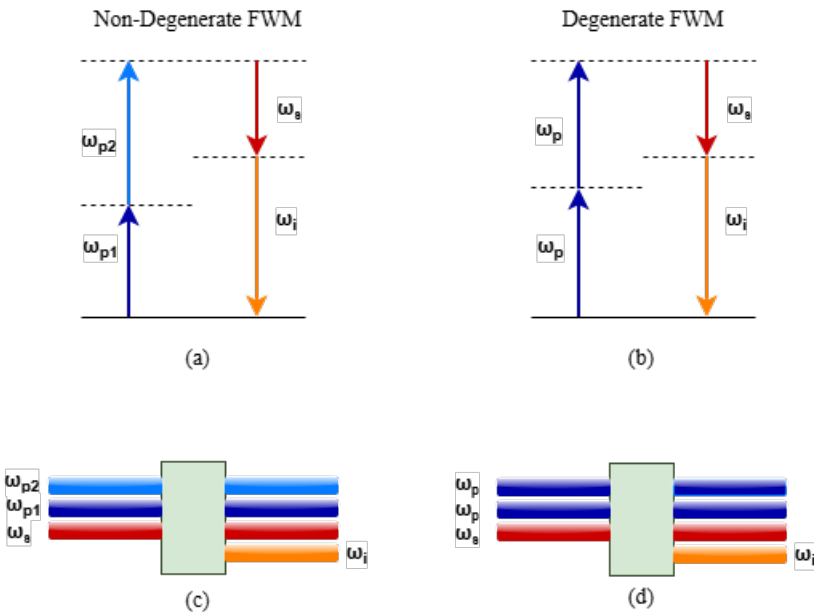


Figure 1.1: Energy level diagrams for (a) non-degenerate and (b) degenerate four-wave mixing. Simplified illustration of (c) non-degenerate and (d) degenerate four-wave mixing processes.

One important third-order nonlinear process that can be useful for optical signal processing (when done purposefully) is four-wave mixing (FWM). This nonlinear optical process is depicted in Fig. 1.1. During FWM, three input beams with distinct frequencies traveling within a nonlinear medium interact with one another and generate a fourth beam. The generated output beam is called the "idler" and its frequency is determined by energy conservation [11]:

$$\hbar\omega_{p1} + \hbar\omega_{p2} - \hbar\omega_s = \hbar\omega_i, \tag{1.3}$$

where $\hbar$ is the reduced Planck's constant, ω_{p1} and ω_{p2} are the "pump" frequencies which make up two of the input beams, ω_s is the frequency of the "signal" which is the third input beam, and ω_i is the idler frequency. The pump pulses are generally more powerful than the other beams, and their power is used for both amplifying the signal beam and generating the idler frequency. FWM is one of several nonlinear processes that can be used for all-optical frequency conversion [6]. FWM is also possible with only two distinct frequency components present at the input of the medium. In this scenario, the pump photons have the

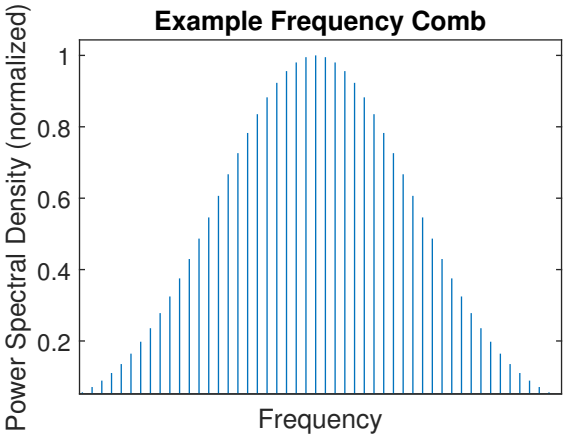


Figure 1.2: Frequency combs have equally spaced spectral components, but the magnitude of each spectral component can be very different.

same frequency and Eq. 1.3 simplifies to

$$2\hbar\omega_p - \hbar\omega_s = \hbar\omega_i. \tag{1.4}$$

The situation where there is only one pump beam is referred to as degenerate FWM, and it is shown in Fig. 1.1b and d, whereas the non-degenerate case is shown in Fig. 1.1a and c.

FWM in nonlinear optical media can also be used to produce what is known as an optical frequency comb. In optics, a frequency comb is an optical spectrum which consists of a set of discrete equidistant spectral lines [12]. In essence, it is a specialized laser (a stabilized mode-locked laser to be precise) which can also be thought of as an optical ruler useful for making precise frequency measurements. A simple illustration of a frequency comb's spectrum is shown in Fig. 1.2.

FWM and many other third-order processes originate from Kerr nonlinearity, also known as the optical Kerr effect. Light that propagates through a Kerr nonlinear medium induces an approximately instantaneous change in the refractive index of the optical medium. This change in refractive index is larger for higher intensities of the incident beam [10]:

$$\tilde{n} = n + n_2 I, \tag{1.5}$$

where $\tilde{n}$ is the total refractive index of the medium, n is the linear refractive index, n_2 is the nonlinear refractive index (also called the nonlinear Kerr coefficient), and I is the intensity of the incident light. The nonlinear refractive index is

proportional to the third-order nonlinear susceptibility through [10]:

$$n_2 = 3\chi^{(3)}/(4n^2\epsilon_0 c), \tag{1.6}$$

where c is the speed of light in vacuum. One application of FWM is the creation of optical frequency combs. These frequency combs can act as optical clock signals (analogous to the electrical clock signal) used for optical signal processing and switching applications [12].

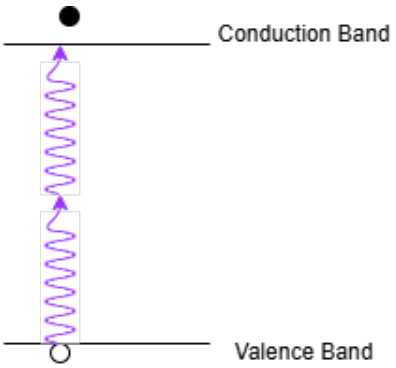


Figure 1.3: Schematic energy level diagram of two-photon absorption.

Another phenomenon that is possible in a material with Kerr nonlinearity is the simultaneous absorption of two photons by an electron moving to an excited state as shown in Fig. 1.3. This is called two-photon absorption (TPA), and it is considered a nonlinear absorption loss when its presence is undesired. The TPA coefficient is generally denoted by α_2 in the literature, and it is proportional to the imaginary part of $\chi^{(3)}$ [10]. For the degenerate case where both photons have the same frequency, the TPA coefficient is given by

$$\alpha_2 = \frac{3\pi\omega}{2n^2c^2\epsilon_0}\text{Im}\ \chi^{(3)}. \tag{1.7}$$

To prevent TPA in a semiconductor material, the bandgap energy must be larger than twice the photon energy corresponding to the operating wavelength. This translates to a bandgap larger than 1.6 eV for a wave operating at the central wavelength of the optical communication C-band (1550 nm). When a semiconductor undergoes TPA, the conduction band gets more populated with electrons that are free to move to higher energy levels by absorbing more photons. This effect is known as free-carrier absorption (FCA), and it is another nonlinear loss that can occur due to TPA.

Second-order nonlinear phenomena related to $\chi^{(2)}$ can also be used for signal processing purposes [13]. The most common $\chi^{(2)}$ processes are second-harmonic

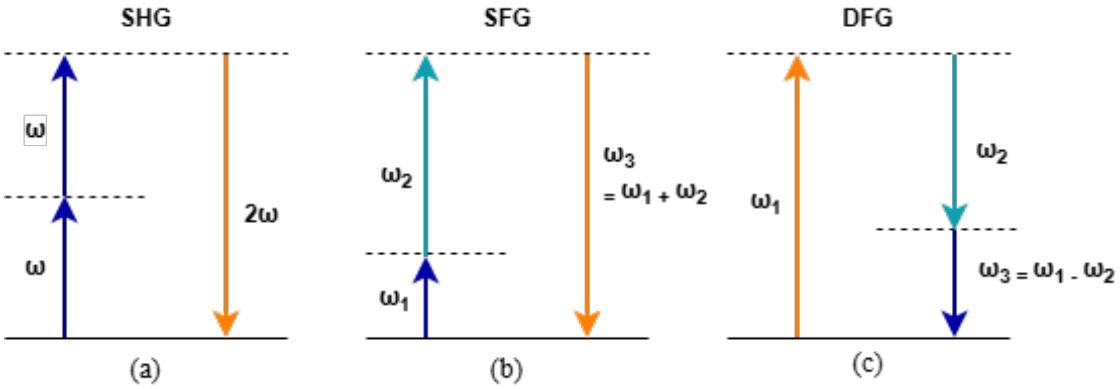


Figure 1.4: Energy level diagram for (a) SHG, (b) SFG, and (c) DFG.

generation (SHG), sum-frequency generation (SFG), and difference-frequency generation (DFG), as illustrated in Fig. 1.4. In addition to being methods for wavelength conversion, these processes can be cascaded to emulate $\chi^{(3)}$ phenomena. In this way, materials with a strong $\chi^{(2)}$ can be used for some of the same applications that require a Kerr medium. Notably, $\chi^{(2)}$ is zero for materials that are centrosymmetric and have inversion symmetry. Such materials will not be able to produce any second-order nonlinear process.

It is important to note that the efficiency of a nonlinear process depends on the phase-matching between its interacting waves. Phase-matching is a direct consequence of momentum conservation, and if the phase-matching conditions are not satisfied, the nonlinear process will have a very low efficiency [11]. For degenerate forward FWM, where both pump beams have the same frequency and direction of propagation, this condition can be expressed as:

$$2\mathbf{k}(\omega_p) - \mathbf{k}(\omega_s) = \mathbf{k}(\omega_i), \tag{1.8}$$

where $\mathbf{k}$ denotes a wave vector. One method of creating devices that are phase-matched over a broad range of frequencies for a certain nonlinear process is through careful dispersion engineering. This is because the source of phase-mismatch is the fact that light at different frequencies experiences different refractive indices [10]. For example, in Chapter 5 of this thesis, FWM is experimentally conducted and reported in meta-waveguide structures which achieve near-zero dispersion in the operating range of wavelengths.

1.3 Waveguide Optics

This thesis revolves around the design and simulation of optical components required in photonic integrated circuits and the most basic fundamental building block of such circuits is waveguides. This subsection introduces the basic theory of waveguide optics.

As the name suggests, waveguides are devices that guide light and control its direction of propagation; they are the "wires" of photonic circuits, and a familiar example is the fiber optic cable. Waveguides operate on the principle of total internal reflection (TIR) and rely on the refractive index contrast between the guiding layer, commonly referred to as the core, and the surrounding material which is usually denoted as the cladding. As illustrated in Fig. 1.5, the guided wave propagates in the core which has a higher refractive index compared to the cladding layer. The refractive index is defined as the ratio of the speed of light in vacuum to that in the medium, thus a higher refractive index means light travels slower [14].

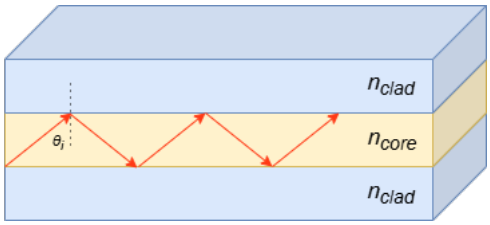


Figure 1.5: A simple planar dielectric waveguide illustrating wave propagation through total internal reflection ($n_{core} > n_{clad}$).

For an incoming wave to be guided, it must undergo TIR at the core-cladding interface which requires incidence angles, θ_i, that are larger than the critical angle $\theta_c = \arcsin(n_{clad}/n_{core})$. This means there is more than one possible angle of propagation for guided light within a waveguide. In ray optics this can be interpreted as a continuous range of allowed propagation angles, but in a full wave description of light only a discrete set of electric field distributions satisfy the boundary conditions and form the solutions to Maxwell's equations for the waveguide structure. These solutions are referred to as the waveguide "modes" [14]. A waveguide mode is an electric field distribution with an unchanging profile in the transverse dimension as it propagates through the medium. They are essentially the eigenfunctions to Maxwell's equations in the waveguide.

In real life, waveguides are finite structures in all three spatial dimensions and their possible electric field profiles of propagating modes cannot be determined through close-formed analytical equations and require numerical mathematical

methods. Thus, the first step to understanding waveguide propagation and modes is to analyze an idealized structure portrayed in Fig. 1.6 where the light is only confined in one transverse direction (x-axis) and the other transverse direction is assumed to be infinite with an unchanging refractive index. This idealization is commonly referred to as the 1D planar or slab waveguide. The

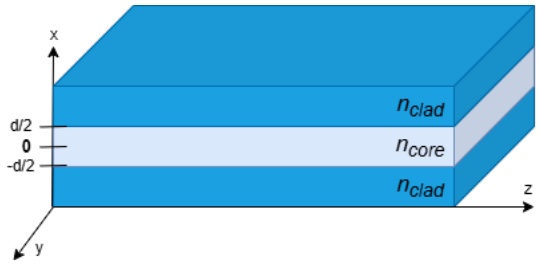


Figure 1.6: 1D planar dielectric waveguide where the core dimension along x is finite while it expands infinitely in the y and z directions.

optical confinement in a dielectric waveguide is via the refractive index difference that occurs at the material interfaces; for the case of the 1D waveguide shown in Fig. 1.6 this boundary occurs at $|x| = d/2$, with the refractive index being equal to n_{core} for $|x| < d/2$ and n_{clad} for $|x| > d/2$.

The behaviour of the electric and magnetic fields of an electromagnetic wave propagating through a medium can be described using Maxwell's equations. For a linear, homogeneous, and isotropic dielectric that has no free charges or currents, these equations become [14]:

$$\nabla \cdot \epsilon \mathbf{E} = 0, \tag{1.9}$$

$$\nabla \cdot \mu \mathbf{H} = 0, \tag{1.10}$$

$$\nabla \times \mathbf{E} = -\mu \frac{\partial \mathbf{H}}{\partial t}, \tag{1.11}$$

$$\nabla \times \mathbf{H} = \epsilon \frac{\partial \mathbf{E}}{\partial t}, \tag{1.12}$$

where $\mathbf{E}$ and $\mathbf{H}$ are the electric and magnetic field vectors and μ and ϵ are the magnetic permeability and electric permittivity of the material. These material parameters can be written as $\mu = \mu_0 \mu_r$ and $\epsilon = \epsilon_0 \epsilon_r$, where μ_r and ϵ_r are the relative permeability and permittivity, respectively. Since the dielectric medium is assumed to be nonmagnetic, the magnetic permeability is simply equal to the vacuum value ($\mu = \mu_0$). Taking the curl of Eq. (1.11) and using the vector identity $\nabla \times (\nabla \times \mathbf{E}) = \nabla(\nabla \cdot \mathbf{E}) - \nabla^2 \mathbf{E}$ along with Eq. (1.9) and Eq. (1.12) yields

$$\nabla^2 \mathbf{E} - \mu\epsilon \frac{\partial^2 \mathbf{E}}{\partial t^2} = 0, \tag{1.13}$$

effectively reducing Maxwell's equations to an electric field wave equation. Assuming a harmonic time dependence, the electric field can be written as $\mathbf{E} = \mathbf{E}(x, y, z)e^{-i\omega t}$, where the spatial and temporal dependence of the field are separate. Substituting this expression into Eq. (1.13) and using $c = \frac{1}{\sqrt{\mu_0 \epsilon_0}}$ leads us to the Helmholtz equation:

$$\nabla^2 \mathbf{E}(x, y, z) + k_0^2 n^2 \mathbf{E}(x, y, z) = 0, \tag{1.14}$$

where $k_0 = \frac{\omega}{c} = \frac{2\pi}{\lambda}$ is the free-space wave number and $n = \sqrt{\mu_r \epsilon_r}$ is the refractive index. To find the modes of the planar waveguide we need to solve this equation for the spatial electric field. Modes where the electric field is transverse to the direction of propagation ($E_z = 0$) are called transverse-electric (TE) and modes where the magnetic field is transverse to the propagation direction ($H_z = 0$) are called transverse-magnetic (TM) [14].

For the 1D slab waveguide, the field is only confined along the x-axis and undergoes no refractive index variation along the y-axis, thus the transverse field profile is only dependent on x ($\frac{\partial E}{\partial y} = 0$), and the spatial dependence of the electric and magnetic fields can be written as

$$\mathbf{E}(x, z) = \mathbf{E}(x)e^{i\beta z}; \mathbf{H}(x, z) = \mathbf{H}(x)e^{i\beta z}, \tag{1.15}$$

where β is the propagation constant. Due to the symmetry and boundary condition for TE modes in a 1D slab waveguide, the only nonzero field components are E_y, H_x and H_y. Similarly, for TM modes, the nonzero field components are E_x, E_z and H_y. Thus, the main scalar wave equations for the TE and TM modes are given by:

$$\frac{\partial^2 E_y}{\partial x^2} + (k^2 - \beta^2)E_y = 0 \quad \text{TE modes}, \tag{1.16}$$

$$\frac{\partial^2 H_x}{\partial x^2} + (k^2 - \beta^2)E_x = 0 \quad \text{TM modes}, \tag{1.17}$$

where $k = k_0 n$ is the wave-number within the material. The type of eigenmode for the wave equations depends on the sign of $(k^2 - \beta^2)$. Within the core layer we want oscillatory behaviour and light propagation, which is only achieved if $\beta < k_0 n_{\text{core}}$. On the other hand, we do not want the light to propagate in the cladding layers, so in these regions we require $\beta > k_0 n_{\text{clad}}$ for the guided modes,

which indicates an exponentially decaying solution to the wave equation and corresponds to the evanescent tails of the guided light in the cladding. Thus, the propagation constant for a stable guided mode travelling in the 1D slab waveguide must satisfy $k_0 n_{\text{clad}} < \beta < k_0 n_{\text{core}}$ [14].

To find the TE eigenmodes of Eq. (1.16), let $\kappa^2 = k_0^2 n_{\text{core}}^2 - \beta^2$ within the core and $\gamma^2 = \beta^2 - k_0^2 n_{\text{clad}}^2$ in the upper and lower cladding. Then solving for each section gives the following general solutions:

$$E_y = A\cos\kappa x + B\sin\kappa x \quad \text{for } |x| < d/2, \tag{1.18}$$

$$E_y = Ce^{-\gamma x} \quad \text{for } x > d/2, \tag{1.19}$$

$$E_y = De^{\gamma x} \quad \text{for } x < -d/2, \tag{1.20}$$

where A, B, C, and D are arbitrary coefficients. The general solution for the

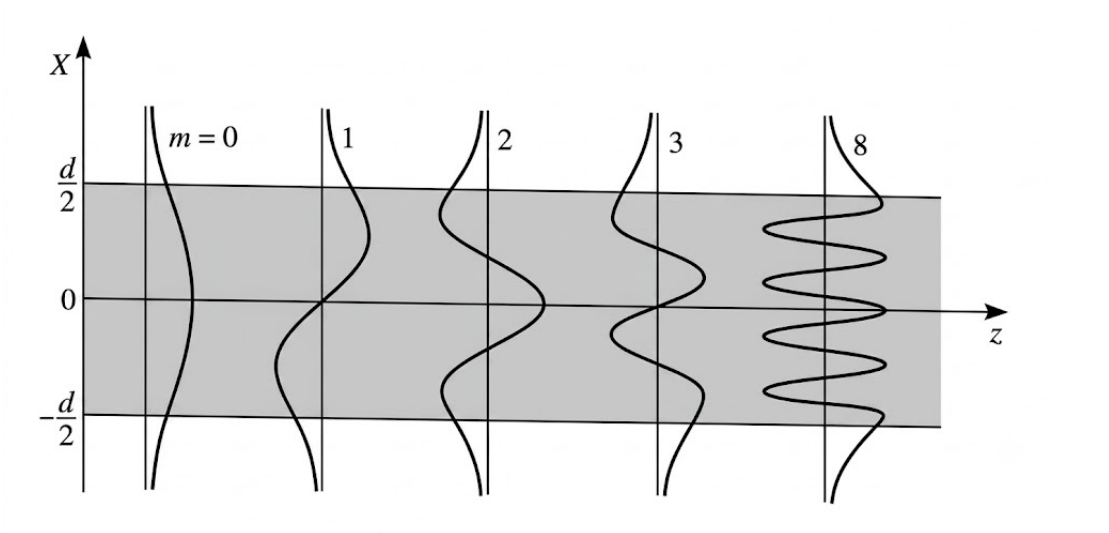


Figure 1.7: 1D planar dielectric waveguide even and odd modes. Adapted from [14].

electric field within the core is a superposition of even (cosine-like) and odd (sine-like) eigenmodes which are visualized in Fig. 1.7. At the core-cladding interface ($x = \pm d/2$), the tangential electric field and magnetic field components, E_y and H_z, must be continuous and consequently the derivative of the electric field, $\frac{dE_y}{dx}$, must also be continuous at the boundaries. Applying these boundary conditions to Eq. (1.18) - (1.20) while separating the odd and even eigenmodes results in the following dispersion relations for the eigenvalues of TE modes in a

1D slab waveguide:

$$\tan(\kappa d/2) = \frac{\gamma}{\kappa} \quad \text{Even TE modes,} \tag{1.21}$$

$$\tan(\kappa d/2) = -\frac{\kappa}{\gamma} \quad \text{Odd TE modes.} \tag{1.22}$$

These transcendental dispersion relations govern the allowed propagation constants with each corresponding to one guided mode in the waveguide. The boundary conditions effectively quantize the valid values for β instead of allowing a continuous range within $k_0 n_{\text{clad}} < \beta < k_0 n_{\text{core}}$. These equations are referred to as dispersion relations because they describe a relationship between the wave number or propagation constant of the wave with its frequency. The term dispersion stems from the fact that light waves at different frequencies experience different propagation constants and refractive indices within the medium and thus travel at different speeds resulting in a dispersed light pulse.

Even though the simple 1D slab waveguide has closed-form analytical solutions for the spatial electromagnetic field profile of its guided modes, the propagation constants of these modes must be solved through numerical or graphical methods. The same process can be applied to Eq. (1.17) for finding the TM eigenmodes and eigenvalues. For TM modes at the core-cladding interface, the tangential electric field and magnetic field components, E_z and H_y, must be continuous and consequently the term $\frac{1}{n^2}\frac{dH_y}{dx}$ must also be continuous at the boundaries. The dispersion relations for the TM modes of the 1D slab waveguide are thus given by:

$$\tan(\kappa d/2) = \frac{n_{\text{core}}^2}{n_{\text{clad}}^2}\frac{\gamma}{\kappa} \quad \text{Even TM modes,} \tag{1.23}$$

$$\tan(\kappa d/2) = -\frac{n_{\text{clad}}^2}{n_{\text{core}}^2}\frac{\kappa}{\gamma} \quad \text{Odd TM modes.} \tag{1.24}$$

In reality, the light confinement in a waveguide occurs over both transverse dimensions while light travels in only one direction, as shown in Fig. 1.8; this realistic dielectric structure that confines light in two dimensions is commonly referred to as a channel waveguide. The principles of operation of channel waveguides are the same as the idealized 1D case, but the mathematics is more involved and it does not possess a closed-form analytical solution. The wave equation for a 2D waveguide essentially becomes a 2D eigenvalue problem. Two approximations that can be used for simple geometries are the effective index method which essentially reduces the problem to two sequential 1D wave equations, or the separation of variables method which solves for the x and y

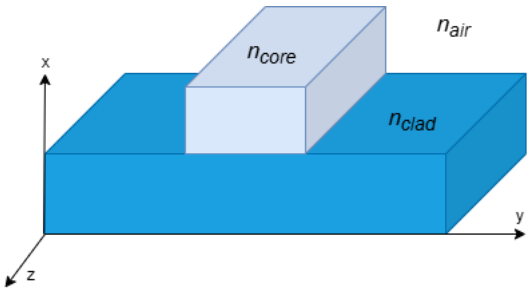


Figure 1.8: Example of a channel waveguide where the guided light is confined in the transverse (x and y) dimensions, surrounded by a lower index bottom cladding and air, while it can freely propagate in the z direction. The light is effectively "channeled" through the core layer of the dielectric medium.

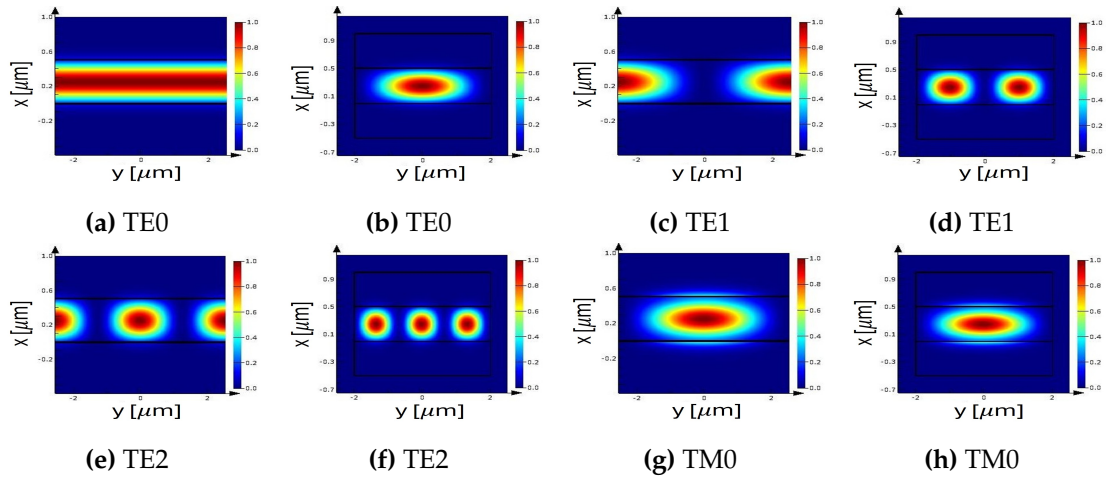
dimensions separately by assuming weak coupling between the two transverse dimensions and separable refractive index profiles. However, these approximations are not valid for all waveguide geometries and require more lengthy calculations compared to the 1D case. In practice, the mode solutions for waveguides and photonic devices are usually determined through computational simulations that implement numerical methods such as the finite-difference time-domain (FDTD) method. In FDTD, the simulation domain is discretized by a mesh and during the simulation Maxwell's equations are solved numerically at each mesh cell, with the electromagnetic fields advanced iteratively in time. Spatial discretization enables the representation of complex geometries, while temporal discretization captures the evolution of the electromagnetic fields.

Unlike the 1D slab waveguide that supports pure TE ($E_z = 0$) and TM ($H_z = 0$) modes, real waveguides have refractive index variations in both transverse dimensions and thus have coupled wave equations for both dimensions; thus, no exact TE/TM separation exists in true 2D waveguides. The guided modes of channel waveguides are hybrid solutions of Maxwell's equations with nonzero longitudinal field components; nevertheless, they are commonly classified as TE-like or TM-like based on the relative dominance of their transverse field components. Some example modes for the ideal 1D planar waveguide and a 2D channel waveguide are illustrated in Fig. 1.9.

Waveguide modes have fundamental parameters that are used to describe and compare their behaviour. One of these is the effective refractive index defined as:

$$n_{\text{eff}} = \frac{\beta}{k_0}, \tag{1.25}$$

where β is the specific propagation constant corresponding to a certain mode. Each propagating mode of a waveguide experiences a different refractive index



(a) TE0 **(b)** TE0 **(c)** TE1 **(d)** TE1

(e) TE2 **(f)** TE2 **(g)** TM0 **(h)** TM0

Figure 1.9: Transverse electric field mode profiles for the 1D slab waveguide ((a), (c), (e), (g)) and 2D channel waveguide ((b), (d), (f), (h)) calculated using the Lumerical FDE solver.

as it travels through the core and a different phase velocity, $v_p = \frac{c}{n_{eff}}$. The phase velocity of a wave is the speed that its wavefronts (surfaces of constant phase) travel. The actual meaningful speed of an electromagnetic wave is the speed that its envelope or wave-packet travels as that corresponds to the speed of the transmitted energy/information. The speed of energy transport for each mode is governed by the effective group index

$$n_g = n_{eff} - \lambda \frac{dn_{eff}}{d\lambda}, \tag{1.26}$$

and the group velocity

$$v_g = \frac{c}{n_g} = \frac{c}{n_{eff} + \omega \frac{dn_{eff}}{d\omega}}. \tag{1.27}$$

Therefore, simultaneously exciting several modes within a waveguide means they reach the end of the device at different times. This form of dispersion is called modal dispersion and it can cause issues in multi-mode waveguides used in optical communication systems where several modes need to be supported within a waveguide and each mode carries a different portion of the same message signal to be transmitted. The effective index is therefore an extremely important property when designing optical devices. Note that for a non-dispersive medium (i.e., no frequency dependence for the refractive index) the effective index and group index are equal and the phase velocity and group velocity are the same.

As shown in the derivation for the 1D slab waveguide, the guided modes have evanescent tails, which means the light is not completely confined to the guiding region (the core) and permeates into the cladding [14]. This can be

problematic for the waveguide performance, and one way of addressing this issue is by increasing the difference in refractive index between the core and cladding in order to obtain tighter confinement of the wave and reduce the leakage in the cladding. This is mathematically observed through the fact that the decay constant in the cladding regions, γ, is reduced when the index contrast is increased. Tighter mode confinement in the core layer results in a smaller effective mode area, A_{eff}. This parameter is used to quantify the effective area covered by the mode in the transverse dimension of the medium. It is called the effective area because the cross-sectional area that the guided mode covers as it propagates through the medium does not have a clear-cut boundary. The effective mode area is mathematically defined as [15]

$$A_{\text{eff}} = \frac{(\iint |\mathbf{E}|^2 \mathrm{d}x\,\mathrm{d}y)^2}{\iint |\mathbf{E}|^4 \mathrm{d}x\,\mathrm{d}y}, \tag{1.28}$$

where $\mathbf{E}$ is the electric field of the wave propagating in the medium and the xy-plane forms the cross-sectional area. At a given optical power, decreasing the effective mode area increases the optical intensity. This means a smaller effective mode area gives us a lower power threshold where we start to observe nonlinear effects in the waveguide. Thus, it is highly important to optimize A_{eff} when designing nonlinear photonic devices.

Another important parameter when dealing with photonic components is the group velocity dispersion (GVD) denoted by β_2. GVD can be mathematically defined as the derivative of the inverse group velocity with respect to angular frequency. It can also be defined as the second derivative of the propagation constant, β, with respect to frequency.

$$\beta_2 = \frac{\partial}{\partial\omega}\frac{1}{v_g} = \frac{\partial^2\beta}{\partial\omega^2}. \tag{1.29}$$

The GVD parameter quantifies the frequency dependence of the group velocity and gives valuable insight into the dispersion behaviour of a device; it is thus highly important when designing integrated photonic devices.

In general, the dispersion experienced by light traversing in a waveguide can be separated into material dispersion and waveguide dispersion. Material dispersion results from the bulk optical media, such as III-V semiconductors or silicon, that are used in the device. The bandstructure and optical properties of the bulk material which dictate how they interact with light are the driving force behind material dispersion. The only way to change this type of dispersion is by changing the chemical composition of the material or performing

manipulations such as doping. The geometry of the waveguide also results in different behaviour for different wavelengths of light and this geometry-derived dispersion is denoted as waveguide dispersion. This type of dispersion can be manipulated during the process of optical component design and is what dispersion engineering refers to. For example, in this thesis I discuss the effects of changing the different dimensions of a subwavelength periodic grating on the photonic bandstructure of the waveguide, and in essence this is dispersion engineering.

1.4 Fundamental Photonic Components

This section provides a brief overview and explanation of different waveguide geometries and the operating principles of the photonic devices that were studied in the thesis project.

1.4.1 Waveguide Geometries

Several geometries exist for optical waveguides, and each of them has its advantages and drawbacks. Fig. 1.10 shows some common configurations used for dielectric waveguides in integrated photonics.

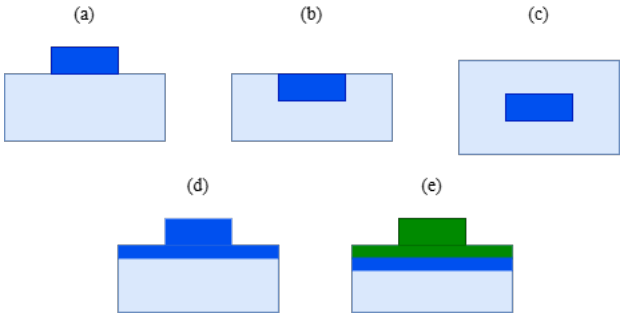


Figure 1.10: Common waveguide geometries: (a) strip, (b) embedded strip, (c) buried, (d) rib/ridge, (e) strip-loaded.

A strip or channel waveguide consists of a high-index core placed on a lower-index cladding and surrounded by air on three sides. This geometry provides the strongest optical confinement in both transverse directions, enabling very compact waveguide bends and dense integration on a circuit. However, the strong confinement also leads to increased sensitivity to sidewall roughness, resulting in higher scattering losses and lower tolerance for fabrication errors. This geometry also typically exhibits strong polarization dependence. In contrast, an embedded strip waveguide retains the same core but is completely surrounded

by cladding material on three sides except for the very top that is exposed to air. This reduces environmental sensitivity and sidewall scattering compared to the more air-clad strips while maintaining high confinement, making it a more stable low-loss geometry commonly used in silicon photonics.

In a buried waveguide the guiding core is entirely surrounded by a lower-index cladding material. This results in weaker confinement and larger mode areas compared to the strip waveguide which is mostly surrounded by air. On the other hand, the buried waveguide geometry undergoes less side-wall roughness sensitivity and lower propagation losses compared to the two strip waveguides. As a result, buried waveguides are typically used in applications prioritizing ultra-low loss. The symmetrical cladding of the buried waveguide also results in a more circular mode shape, which is useful for coupling to optical fibers.

Rib/ridge waveguides are structures where a partially etched high-index core sits on a remaining slab. This configuration allows part of the optical mode to extend into the slab, reducing interaction with the etched sidewalls and thereby lowering scattering loss compared to strip waveguides. However, they require careful control of slab thickness and generally occupy more area due to weaker mode confinement.

Finally, a strip-loaded waveguide modifies a slab waveguide by adding an additional high-index overlay or "load" layer on top, which adjusts the effective index and mode profile without necessarily changing the core geometry. These waveguides look similar to the rib/ridge geometry, but they use two different high-index materials. This approach is often used for tuning devices such as phase shifters or modulators, where controlled perturbation of the optical mode is more important than tight confinement.

The chosen waveguide geometries for this project were the buried and strip geometries (depending on the upper cladding being air or silica). These are the most commonly used geometries for SWG waveguides in silicon photonics and they are more easily fabricated compared to the others.

1.4.2 Optical Couplers

Optical couplers are an essential building block for circuits. They are integrated photonic devices that enable optical power transfer from one waveguide to another within the same circuit, or between two different optical systems such as a fiber and photonic chip. The operation of optical couplers is fundamentally based on the interaction and interference of light waves when waveguides are

structurally joined or brought into close physical proximity with each other. The specific principle of operation depends on the type of coupler.

Directional couplers

Conventional directional couplers usually refer to co-directional couplers (illustrated in Fig. 1.11) where the wave that gets coupled into the secondary waveguide travels in the same direction as the input wave in the first waveguide. This is in contrast to contra-directional couplers where the input and output waves travel in opposite directions. Directional couplers rely on the evanescent field coupling that occurs when two waveguides are brought close together. As mentioned in Section 1.3, the optical modes are not purely confined to the core layer of the waveguide and have decaying tails that extend into the cladding regions. This is actually a useful phenomenon for couplers, since a stronger evanescent field means the coupled waveguides can be positioned further apart and still obtain efficient coupling.

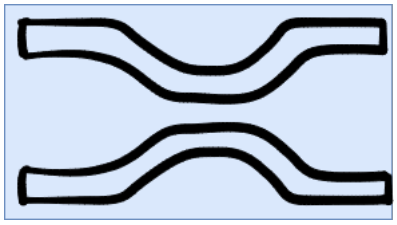


Figure 1.11: A simple co-directional coupler.

The behaviour of a directional coupler is governed by the coupled mode theory and the ratio of power that gets coupled from one waveguide to another relative to the input power is given by [16]:

$$\kappa^2 = \frac{P_{\text{cross}}}{P_0} = \sin^2(CL), \tag{1.30}$$

where P_{cross} is the optical power coupled across the directional coupler, P_0 is the input power, C is the coupling coefficient and L is the coupler length. For a lossless directional coupler, the light can either pass through the original waveguide or get coupled across, so the following conservation relation holds:

$$\kappa^2 + t^2 = 1, \tag{1.31}$$

where t is the fraction of the power left inside of the initial waveguide. Therefore, a lossless directional coupler passes the light waves back and forth between the two waveguides along the entire coupler length. To ensure that the light stays in

the second waveguide after getting coupled, the coupler length should be equal to the cross-over length:

$$L_x = \frac{\lambda}{2\Delta n}, \Delta n = n_1 - n_2, \tag{1.32}$$

where Δn is the effective index difference for the first two eigenmodes of the coupled waveguide structure.

When two waveguides are brought close together, their individual isolated eigenmodes interact and split into two different supermodes with even and odd symmetry known as the anti-symmetric and symmetric supermodes, respectively. In the case of the symmetric mode, the electromagnetic waves in both waveguides are fully in-phase, thus resulting in constructive interference and an intense field in the gap between the two waveguide cores. For the anti-symmetric mode of the coupled system, the electromagnetic fields in the waveguides are completely out of phase, resulting in a node in the middle of the coupled system where the field intensity is zero due to destructive interference. The optical mode is effectively pushed outwards towards the outer bounds of the two coupled waveguides. This phenomenon is illustrated in Fig. 1.12.

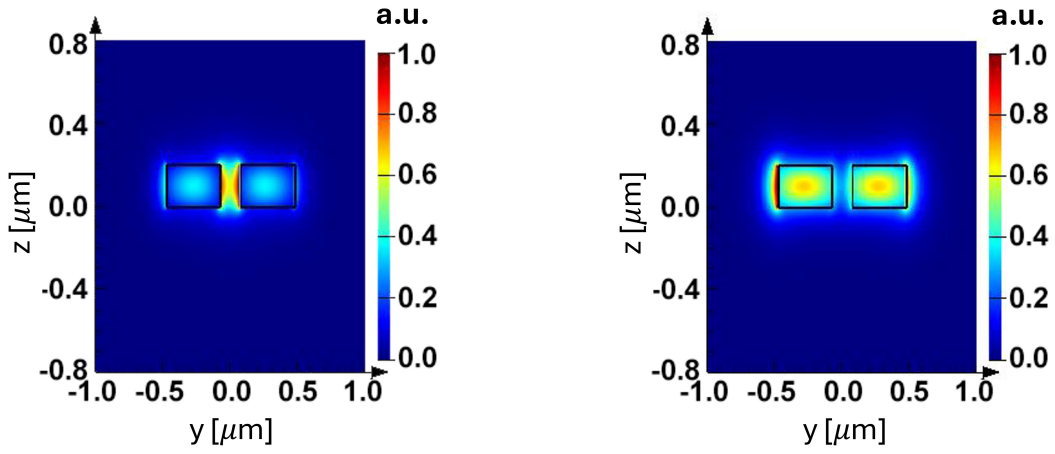


Figure 1.12: Example of the transverse electric field profile of (a) symmetric and (b) anti-symmetric supermodes of a coupled-waveguide system.

Edge couplers

An important category of optical couplers are those involved with coupling light from fiber optical cables into much smaller integrated photonic chips. One such device is the fiber-to-chip edge coupler. An edge coupler does not

operate based on evanescent coupling. It works by directly coupling the light from a fiber into a smaller integrated waveguide on a chip through spatial mode-matching at the coupler tip to match the larger fiber mode. This larger input mode is then transformed in the coupler's mode conversion region into a smaller mode area that matches the mode size on the chip. This process of mode conversion can occur in several ways in an edge coupler, and one common way is through the inverse taper method showcased in Fig. 1.13. By tapering and slowly reducing the width of the edge coupler towards the fiber, we can decrease the modal confinement and thus increase the beam size. This decrease in modal confinement is directly related to the spatial cut-off condition of the waveguide modes. As an optical mode approaches its cut-off condition with a reduction in waveguide width, it becomes less tightly confined and its electric field expands. Edge coupler tapers take advantage of this effect while remaining far enough from cut-off where the light is no longer confined and a guided mode no longer exists. The efficiency of an edge coupler is determined by the fraction of the input power from the fiber that reaches the end of the coupler and enters the photonic chip.

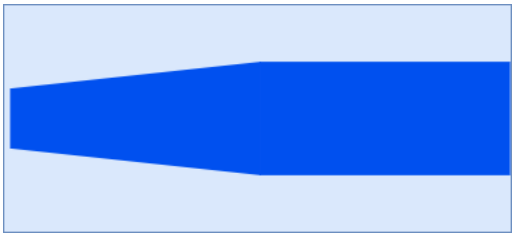


Figure 1.13: A simple edge coupler realized through an inverse taper.

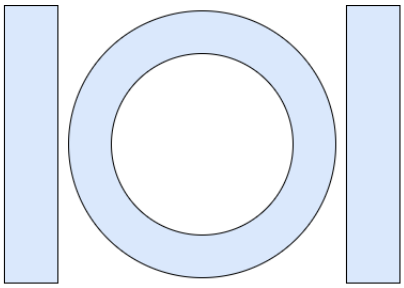
1.4.3 Ring Resonators

Another essential building block for photonic circuits is an optical ring resonator. These versatile devices consist of a ring waveguide coupled to either one or two straight bus waveguides (a simple illustration is shown in Fig. 1.19(a)). Ring resonators operate on the principle of total internal reflection and interference [14]. The geometry of the ring resonator determines which frequencies are allowed to resonate (i.e. undergo constructive interference) and which frequencies get filtered (i.e. undergo destructive interference) within the ring cavity. The transmission spectrum of a ring resonator indicates which frequency components can resonate inside, and it can look similar to Fig. 1.19(b) where the transmitted frequencies are equally separated by a value referred to as the free spectral range

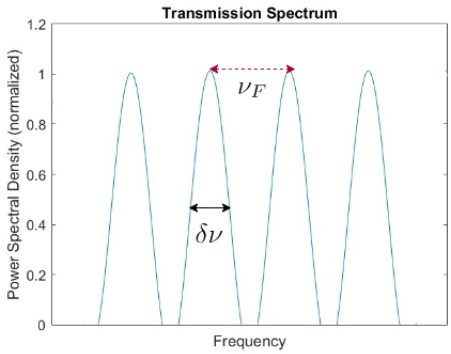
(FSR) and denoted by ν_F [14]. The FSR is given by:

$$\nu_F = \frac{\lambda_0^2}{n_g L}, \tag{1.33}$$

where λ_0 is the resonance wavelength, n_g is the group index that the light experiences in the ring medium, and L is the circumference of the ring. The FSR of a ring resonator is technically not constant because it changes over a broad wavelength range due to dispersion. But over a narrow bandwidth it is generally considered constant.



(a)



(b)

Figure 1.14: (a) Simple ring resonator with two bus waveguides. (b) Illustration of a ring resonator transmission spectrum with equally spaced frequency components.

The coupling region between the bus waveguides and ring are essentially directional couplers and they can be explained using the coupled-mode theory equations described above [16]. When a wave enters and propagates through a bus waveguide its mode is initially isolated to that single medium, but as the light approaches the bent ring section it experiences a modified refractive index as the evanescent tails of the wave can interact with the ring resonator and couple some or all of the light into the ring. The coupling efficiency is

highly dependent on the distance between the ring resonator and waveguide in addition to the coupling length, which is defined as the effective length in the resonator where the coupling interaction happens [14]. After entering the ring structure the light propagates for as many round-trips as possible before it either decays from internal losses in the ring or gets coupled back into a bus waveguide. The ability of an optical ring cavity to sustain light is quantified using the quality factor (Q-factor), which is a measure of how many round-trips the wave survives in the ring. The Q-factor can be mathematically defined as

$$Q = \frac{\nu}{\delta\nu}, \tag{1.34}$$

where ν is the operating frequency and $\delta\nu$ is the full-width-at-half-maximum (FWHM) of the frequency components in the transmission spectrum. Thus, the Q-factor relates the resonance frequency to the line-width of the transmission spectrum peaks. Ring resonators have two main configurations which depend on the number of straight bus waveguides coupled to the ring. The all-pass configuration consists of a ring coupled to a single bus waveguide, while the add-drop configuration includes a separate input and output bus waveguide coupled to either side of the ring. As previously mentioned, the gap between the ring and bus waveguides determines the strength of coupling.

Ring resonators can operate under three different coupling regimes which are governed by the relation between the internal losses of the optical cavity and the coupling strength from the bus waveguide to the ring. The critical coupling regime is when the internal losses in the optical cavity are equal to the amount of light that couples into the ring from the input bus waveguide. This regime has the highest extinction ratio, where the transmission spectrum of the through path goes to zero at the resonance wavelengths, because the light that stays behind in the bus waveguide is completely destructively interfered by the light getting coupled back out of the ring. This type of coupling is ideal for filtering applications where the resonance peaks are fully removed from the input bus waveguide and transmitted through the drop port of the output waveguide. Under-coupling happens when the cavity losses in the ring are higher than the coupling strength, while over-coupling means the opposite.

The transmission spectrum for over-coupled light is much more broadband with wider resonances compared to the under-coupled situation. This is due to the difference in photon lifetime in both situations. Due to strong coupling the light easily enters the ring, but this strong coupling just as easily couples the light back out into the bus waveguide, thus the photons do not spend much time

circulating in the ring resonator. With very weak coupling the light enters the ring with difficulty so not much couples into the ring, but the portion that does enter the ring also cannot leave easily by coupling out, therefore the photons become trapped and circulate for much longer within the ring resonator leading to a higher Q-factor and stronger internal electric field strength.

The transmission spectrum at the output port is actually the result of interference between the light that stays within the bus waveguide and the light that enters the ring, circulates, and then leaks back out by coupling to the bus waveguide. Broadband peaks/dips mean a lower Q-factor. Thus, over-coupled rings have lower Q-factors and wider frequency dips compared to the critically coupled and under-coupled versions. Under-coupled rings have high Q-factors so they can be useful for sensing applications and nonlinear optics. Critically coupled rings are generally useful for filtering applications, but when paired with a high Q-factor they become suitable for efficient nonlinear processes with low input threshold powers.

In Chapter 4 of this thesis, I showcase example designs of ring resonators in each coupling regime using the AlGaAs-OI platform and SWG structures. The nonlinear behaviour of ring resonators with Huygens' meta-waveguide structures is experimentally explored in Chapter 5 for an SOI photonic chip.

1.5 III-V Semiconductors

III-V semiconductors are compounds created from the combination of elements from group III and group V of the periodic table. This family of semiconductors possesses many attractive electronic and optical properties [6]. Many materials belonging to this group, such as $Al_xGa_{1-x}As$ with $x < 0.45$, have direct energy bandgap compositions; this means the minimum energy of the conduction band and highest energy level of the valence band are aligned at the same exact crystal momentum, which results in energy-momentum curves similar to Fig. 1.15. This makes the inter-band electronic transitions easier as the electrons can move to the conduction band by absorbing photons without the need for phonon-assisted momentum conservation. The same is true for electronic transitions from a higher energy level in the conduction band to a lower level in the valence band. Direct-bandgap semiconductors can thus act as efficient laser sources due to efficient radiative recombination between electron-hole pairs [17]. This facilitates the integration of active devices and passive components on the same photonic chip since they can all be made using the same material platform.

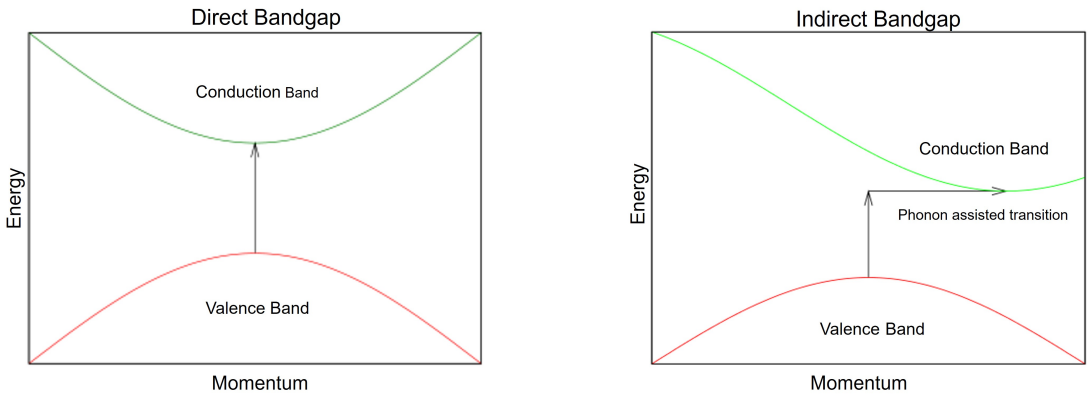


Figure 1.15: Energy-momentum band diagrams of (a) direct and (b) indirect semiconductors.

Another beneficial property of many III-V semiconductor compounds is their adjustable refractive index, which can be tuned by changing the material composition. For ternary compounds composed of three elements, this usually means changing the ratio of the alloy mixture. For example, $Al_xGa_{1-x}As$ is an alloy between GaAs and AlAs, which means the fraction of Ga versus Al is what controls the optical properties of this compound. AlGaAs is only a direct bandgap semiconductor for aluminum concentrations below 45%, and its refractive index can be modified in a relatively broad range (2.9 - 3.4) in the telecom C-band by changing the aluminum fraction between $0 \leq x \leq 1$ [7]. This is useful because it permits flexibility when constructing integrated optical devices using a single III-V semiconductor material. Having control over the refractive index is essential for compatible integration since different devices in a PIC have varying refractive index needs.

Many III-V semiconductor compounds exhibit strong $\chi^{(2)}$ and $\chi^{(3)}$ nonlinearity while maintaining low nonlinear absorption losses when the operating wavelength lies outside their TPA range [6]. Thus, not only is this family of materials suitable for passive and active components, but they are also suitable for both linear and nonlinear functions. This makes them attractive candidates for all-optical signal processing and integrated photonics on a chip [7]. Among III-V semiconductors, AlGaAs is especially useful for nonlinear processes in the telecommunication C-band (1530 - 1565 nm) since its energy bandgap can be made much higher than the photon energies at most of these wavelengths [7]. The $Al_{0.18}Ga_{0.82}As$ composition was specifically chosen for this project as it is transparent to TPA at the wavelengths commonly used for optical communication systems, making it very efficient for conducting nonlinear processes in this

spectral range [7], [8]. The bandgap energy must be larger than 1.6 eV for no TPA to occur at 1550 nm, and the $Al_{0.18}Ga_{0.82}As$ compound has a bandgap energy of 1.65 eV. Another benefit of this AlGaAs composition is its high refractive index (3.28), resulting in tighter mode confinement, especially when paired with an insulator substrate material. Additionally, its Kerr nonlinearity is 3 times stronger than that of silicon at 1550 nm [7].

Table 1.1: Comparison of popular nonlinear photonic integrated platforms

Material	Bandgap Energy [eV]	n_2 [$10^{-18}m^2/W$]	α_2 [cm/GW]	$\chi^{(2)}$ [pm/V]	Ref.
Silicon	1.12	4.5	0.79	0	[7]
AlGaAs	1.42 - 2.16 eV	15	0.05	10-200	[7]
InGaAsP	0.75 - 1.35 eV	19	19		[7]
$LiNbO_3$	3.7 - 4.0 eV	2.5	0	50-54	[18]
Si_3N_4	4.5 - 5.3 eV	0.24	0	0	[19]

To argue for the use of III-V compounds, they should be compared with silicon, which is currently the most commonly used semiconductor in optical communications systems. Table 1.1 summarizes this comparison, and all the values correspond to a wavelength of 1550 nm. Aside from the well-known drawback of being an indirect bandgap semiconductor, silicon is also a centrosymmetric crystal. This means silicon cannot be used for SHG, DFG, or SFG processes. Furthermore, electro-optic modulators commonly use the Pockels effect, which is a second-order nonlinear phenomenon [10]. Thus, a lack of second-order nonlinearity also prevents silicon from being easily used for electro-optic modulators. Inversion symmetry limits the nonlinear operations that can be done when silicon is the material platform for an all-optical signal processing circuit.

Even though silicon showcases strong $\chi^{(3)}$ nonlinearity, the value of n_2 for AlGaAs is more than three times larger. Another important drawback of silicon in the telecommunication C-band is the presence of TPA. Silicon's energy bandgap is not high enough to prevent nonlinear absorption effects. In comparison, AlGaAs can have TPA coefficients that are almost sixteen times smaller than silicon (refer to Table 1.1). Therefore, in terms of nonlinear optical effects, AlGaAs has the upper hand. AlGaAs also has a major advantage over its cousin InGaAsP. Although InGaAsP has a slightly higher Kerr nonlinear coefficient, its large TPA

losses at 1550 nm make it difficult to achieve efficient nonlinear phenomena in the telecom C-band wavelength range.

Other popular material platforms being currently explored for integrated photonics and nonlinear applications are lithium niobate ($LiNbO_3$) and silicon nitride (Si_3N_4). Both of these materials have extremely large bandgap energies and transparency windows; thus, their two-photon absorption at 1550 nm is essentially null. Even though $LiNbO_3$ is a highly nonlinear material with large second and third-order nonlinearity, it is still less nonlinear compared to AlGaAs at 1550 nm. Furthermore, $LiNbO_3$ does not exhibit light emitting properties, so it cannot be used for active devices. Si_3N_4 is used as a low-loss alternative to silicon as it allows ultra-low-loss propagation and is also considered a highly nonlinear medium even though its nonlinear coefficient is the smallest in Table 1.1. Its high nonlinearity stems from its low optical loss and tight modal confinement. However, Si_3N_4 suffers the same drawbacks as silicon, notably the absence of second-order nonlinearity and the inability to emit light.

Thus, this thesis focuses on combining AlGaAs, termed "the silicon of nonlinear optics" [20], with subwavelength grating structures to create designs of fundamental photonic components that can be used for any integrated photonic circuit based entirely on III-V semiconductors for optical communication applications.

1.6 Meta-waveguide Structures

1.6.1 Background Theory

Meta-waveguides are waveguides where the guiding layer is a periodic arrangement alternating between high- and low-refractive-index materials. They are called subwavelength structures when the grating period, Λ, is much smaller than the wavelength, λ, of the propagating light. A simple periodic waveguide is shown in Figure 1.16. The waveguide core is composed of periodic dielectric segments of length a with a refractive index of n_{wg}, and the cladding that fills up the spaces in between with an index of n_{clad}. The waveguide sits on top of a substrate layer with an index of refraction n_{sub}. The duty cycle, or fill factor, is defined as a/Λ; this is the portion of the unit cell filled with the higher index material.

An electromagnetic wave traveling through such a periodic array can be treated with the same methods used for electrons traveling in a periodic potential,

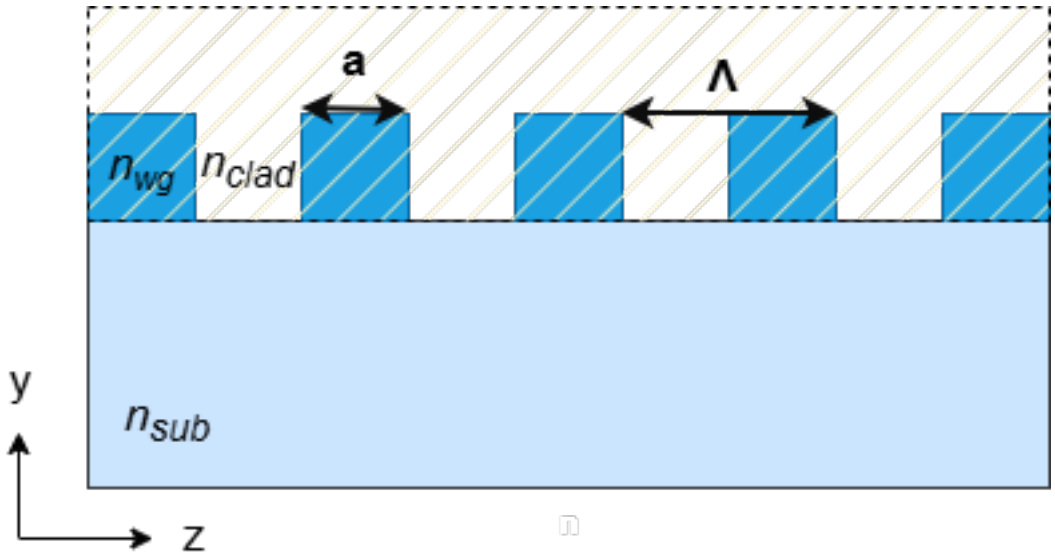


Figure 1.16: Structure of a simple periodic waveguide in 2D. The hashed filling indicates the cladding layer.

and can thus be described by Floquet-Bloch modes [21]. If we assume single-mode propagation in the positive z direction, according to Floquet-Bloch theory, the electric field of the propagating light is given by

$$\mathbf{E}(x,y,z) = e^{ikz}\mathbf{u}_k(x,y,z), \tag{1.35}$$

where $\mathbf{u}_k$ is the periodic function that represents the Floquet-Bloch profile and is defined such that $\mathbf{u}_k(x,y,z+\Lambda) = \mathbf{u}_k(x,y,z)$. The familiar exponential term for travelling waves contains the propagation constant, k, which is assumed to be a complex number that can be decomposed into its real and imaginary parts: $k = k_r + ik_i$. The real part of the complex wave vector describes the propagation properties while the imaginary component describes the losses or gains experienced by the wave.

The guided wavelength of this periodic structure is determined by the effective refractive index seen by the Floquet-Bloch mode as it propagates: $\lambda_g = \lambda/n_{FB}$. Thus, the real part of the wave vector can be written as

$$k_r = 2\pi/\lambda_g = 2\pi n_{\mathrm{FB}}/\lambda. \tag{1.36}$$

Since the imaginary part of the wave vector determines the attenuation or amplification experienced by the electromagnetic wave, for a passive waveguide it can either be zero (lossless) or negative (lossy).

The operation regime of this periodic waveguide depends on the ratio between the grating period and the guided wavelength. These regions of operation

are illustrated in Figure 1.17, where the vertical axis shows radial frequency and the horizontal axis shows the wave vector values. The positive and negative sides of the horizontal axis are used for representing the real and imaginary parts of the wave vector, respectively.

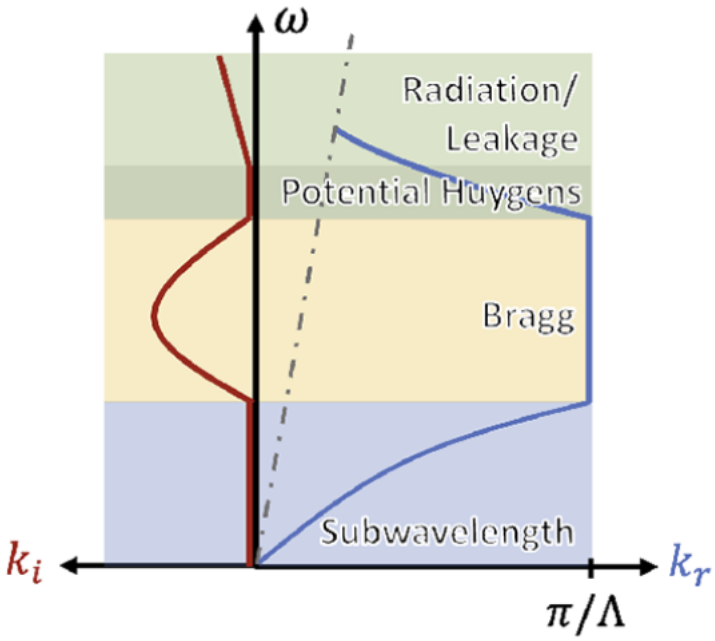


Figure 1.17: Waveguide dispersion relations in different regions of operation. Adapted with permission from [9] © Optical Society of America.

The operation of the periodic waveguide can be divided into three main regimes [9]:

Bragg Regime

The Bragg regime, also called the photonic bandgap regime, occurs when the grating period is equal to half the wavelength of the guided light,

$$\Lambda = (1/2)\lambda_g = \lambda/2n_{FB}, \tag{1.37}$$

which makes $k_r = \pi/\Lambda$ for all frequencies. The photonic bandgap of a device or material refers to the range of frequencies where light cannot propagate in the forward direction; this is due to destructive interference effects that arise from a periodicity of high and low refractive indices that make up the structure [22]. Bragg reflection gratings exploit this phenomenon and often use back reflection as a filtering effect. The attenuation that the forward-propagating light experiences in this regime is showcased in Figure 1.17 with a highly negative k_i .

Radiation Regime

For a grating period of $\Lambda > (1/2)\lambda_g$, some of the electromagnetic wave traversing the waveguide structure gets radiated into the substrate and cladding. This region is thus called the leakage or radiation regime and it is characterized by a negative k_i due to attenuation. However, as shown in Figure 1.17, there is a region above the bandgap frequencies which demonstrates lossless propagation ($k_i = 0$), and this is only possible under certain conditions. One of the possible conditions that allows for lossless propagation above the bandgap is carefully designed resonances that result in the creation of Huygens' meta-waveguides [9]. The potential Huygens' regime is right above the photonic bandgap. Unlike the subwavelength regime, Huygens' meta-waveguides are resonant waveguides that are formed of dielectric nano-antennas that achieve pure lossless forward propagation via the Kerker condition [23]. The forward Kerker condition is satisfied when the Mie-resonant electric and magnetic dipole moments of the nano-antennas are spectrally overlapped for both amplitude and phase. The near-field coupling between the adjacent resonant nano-antennas enables the lossless forward propagation and zero backscattering in theory. The Huygens' band can also be useful due to the nature of its band-structure. As seen in Figure 1.17, this region is characterized by an inverse frequency-wavevector dispersion relationship which results in a negative group index across the entire band. The Huygens' regime was experimentally explored in this thesis for the SOI platform as outlined in Chapter 5.

Subwavelength Regime

Subwavelength engineering refers to design techniques that involve creating structures with dimensions smaller than the wavelength of electromagnetic waves. Even though subwavelength structures have been used for controlling the propagation and properties of electromagnetic waves as early as the 19th century (Heinrich Hertz's wire grid polarizer for radio waves), the use of such structures for waveguides was first demonstrated in 2006 by Cheben *et al.* [24].

The subwavelength regime occurs when the grating period of the waveguide is less than half the guided wavelength ($\Lambda < (1/2)\lambda_g$). This is the operating regime for SWG waveguides. In this regime, there are no diffraction losses, no photonic bandgap effects, and no resonant modes. For an ideal SWG waveguide, the attenuation is zero ($k_i = 0$) for all frequencies below the bandgap. Even though the waveguide core is still periodic, the incident electromagnetic wave propagates as if it were traveling within a homogeneous medium, because the

wavelength of the wave is much larger than the grating period. The optical properties of the waveguide are determined by the geometry of the subwavelength grating and the specific material that is used. The mathematical model for this regime can be derived using homogenization methods that transform the periodic waveguide core into a solid-core waveguide with an equivalent refractive index (as shown in Chapter 2). In these models, the periodic grating layer is modeled as a uniform anisotropic material similar to a uniaxial crystal. Different equations and algorithms have been developed to obtain the effective refractive index and dispersion relations of such structures [25].

One of the key advantages of an SWG waveguide is the customizability of its optical properties. Having control over the effective refractive index and dispersion characteristics of the waveguide enables higher control of the propagating light. Refractive indices have great importance when designing optical devices. In general, the higher the refractive index difference between the core and cladding material, the higher the confinement that can be achieved within the guiding layer. Thus, the effective mode area and confinement of the light, which affects the efficiency of different optical processes, is directly impacted. The ability to adjust the refractive index also allows for using the same material for different applications, because we can change the effective refractive index without the need to look for a completely different material platform. This is useful for compatible device integration in photonic circuits since it is much easier to combine devices based on the same material onto a single chip rather than trying to integrate several devices with completely different material.

SWG waveguide structures are not limited to simple planar waveguides; in fact, these periodic gratings have been implemented in many different optical devices used in silicon photonics as shown below [9].

1.6.2 Enhancements in Silicon Photonics

In this section, the results of a few research papers are summarized to highlight the impact of SWG engineering in the field of silicon photonics for telecommunication purposes.

SWG Couplers

In optical communication systems, a coupler refers to an optical device that transfers light signals from one device to another [14]. Off-chip couplers are important components for efficiently transferring light between fiber optical cables and photonic circuits, especially since the beam radius and size of the

waveguide core is much larger in standard SMF-28 fiber optic cables compared to integrated photonic circuits. This difference in beam size means the optical coupler needs to transmit light from a tight effective mode area to a larger effective mode area (and vice versa) while minimizing leakage losses.

SWG couplers can have different configurations, but the main idea is to increase the spot size of the propagating mode by enlarging its effective mode area before it is sent into the optical fiber. This is essentially done by gradually decreasing the effective refractive index that the propagating mode experiences by adjusting the duty cycle of the subwavelength grating. The waveguide mode is thus expanded until it matches the fiber spot size.

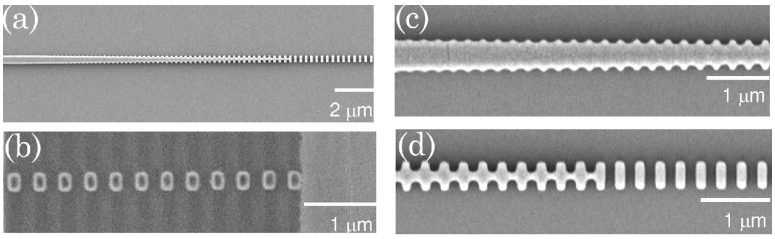


Figure 1.18: (a) SEM image of SWG coupler. (b) Low-confinement section. (c) High-confinement section. (d) Intermediate section. Reprinted with permission from [26] © Optical Society of America.

The first fiber-chip edge coupler that used SWG structures was demonstrated in 2006 by Pavel Cheben *et al.* on the silicon-on-insulator (SOI) platform [24]. This coupler exhibited a coupling loss as low as 0.9 dB. Another SWG fiber-chip coupler, shown in Figure 1.18, was showcased in 2010 and displayed similar coupling losses, but with a broad wavelength bandwidth of 170 nm [26].

It has been reported in the literature that SWG fiber-chip couplers are more forgiving to fabrication tolerances compared to solid-core couplers [27]. This is a counter-intuitive result since one would expect the complexity of adding subwavelength grating structures in the fabrication process to make them less forgiving. Another major advantage for SWG couplers is the compactness that such designs can provide along with high coupling efficiencies [9]. For example, a research paper funded by IBM [27] has demonstrated a fiber-chip edge coupler with a loss of -0.7 dB (TE polarization) and -1.4 dB (TM polarization) from a standard SMF-28 optical fiber to a silicon wire waveguide at the telecommunication O-band.

Chapter 3 of this thesis outlines the design methodology and simulation results for an AlGaAs-OI SWG edge coupler. The device couples light from fiber to a channel waveguide at 1550 nm with a loss of -0.45 dB (TE polarization) and -0.56 dB (TM polarization). The proposed design exploits the refractive index

engineering enabled by subwavelength waveguides to achieve a high coupling and mode conversion efficiency over a total length of 30 μm.

SWG Ring-resonators

Another optical device that can benefit from SWG structures is a ring resonator. Ring resonators operate on the basic principles of total internal reflection (TIR) and interference [14]. The geometry of the ring resonator determines the wavelengths that are allowed to resonate and those which get filtered through destructive interference. Due to their wavelength-selective nature, ring resonators are useful in signal processing applications that require filtering. A ring res-

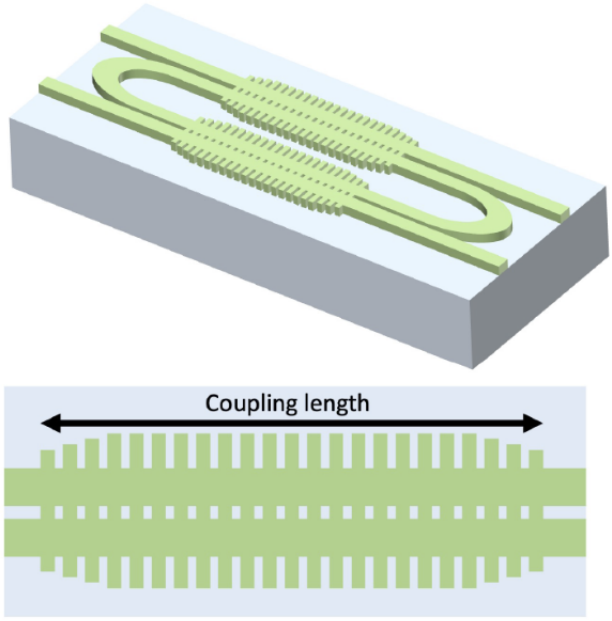


Figure 1.19: Schematic illustration of SWG ring resonator. Adapted with permission from [9] © Optical Society of America.

onator is generally composed of a looped waveguide along with one or two straight waveguides on the sides. The straight waveguides get coupled to the ring through the evanescent field of the light. When a wave enters and travels through one of the straight waveguides, the evanescent field of the wave can interact with the ring resonator and transfer some or all of the light into the ring. This interaction region is referred to as the coupling length. The coupling efficiency of a ring resonator depends on the distance between the looped and straight waveguides in addition to the coupling length [14].

Ring resonators can be made more compact using SWG structures. One reason for higher compactness is that the minimum coupling length is reduced, so the device can shrink in size without reducing coupling efficiency [9]. This is

because the inherent field de-localization that is a characteristic of SWG waveguides allows for shorter coupling lengths and larger spacing between the ring and straight waveguide sections. Figure 1.19 shows a schematic illustration of ring resonators that incorporate SWG structures. The subwavelength grating can be implemented in many ways; the entirety of the looped and straight waveguides can be segmented into SWG structures, or the periodic grating can be limited to a small portion of the device such as the coupling regions.

The first use of SWG structures for ring resonators was done by J. Wang *et al.* [28]. They were able to realize SWG ring resonators with Q-factors as high as 2 x 10^5, which is comparable to conventional SOI ring resonators, while using a ring radius as small as 10 μm. SWG micro-ring resonators have also been demonstrated with a Q-factor of 11,500 and a 5 μm radius [29].

Implementing SWG microring resonators with AlGaAs can potentially lead to highly efficient FWM in integrated circuits for optical signal processing. Micro-ring resonators with high quality factors have already been reported with AlGaAs using conventional designs [30], so subwavelength engineering can be used to build upon this progress. As such, Chapter 4 of this thesis is dedicated to the design and simulation of AlGaAs-OI SWG ring resonators. Additionally, nonlinear FWM experiments were conducted in Huygens' SOI ring resonators with the results and process reported in Chapter 5.

SWG Beam Splitters

Beam splitters have also been demonstrated using SWG structures. One key enhancement that subwavelength engineering offers for beam splitters is the large bandwidth of operation that can be achieved. Broadband optical devices are highly useful for optical communication networks, particularly for wavelength division multiplexing (WDM) systems.

Integrated beam splitters are commonly implemented using multi-mode interference (MMI) couplers. Applying subwavelength engineering to MMI couplers led to the first realization of an SWG slotted MMI which reduced the device footprint by a factor of two compared to conventional MMI couplers, without affecting the device performance [31]. Another paper demonstrates an ultra-broadband SWG beam splitter that has a 500 nm bandwidth that covers all the possible optical communication wavelengths [32]. The authors also claim that their device is three times smaller than the conventional counterpart at the time. The ultra-broadband beam splitter in this study was achieved by exploiting the inherent anisotropy of subwavelength grating structures. The fabricated device is displayed in Figure 1.20.

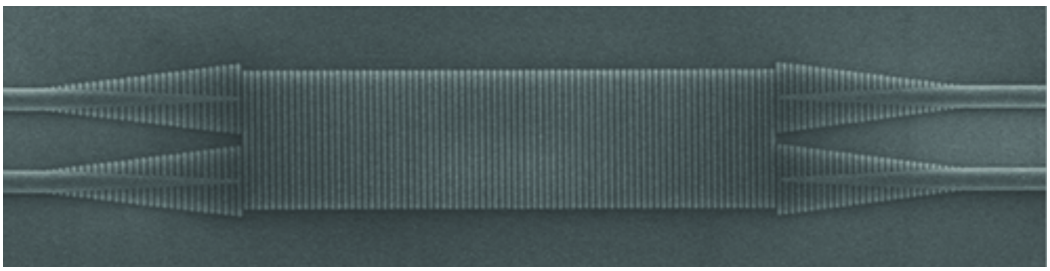


Figure 1.20: SEM image of a fabricated ultra-broadband SWG MMI. Source: [32]

Due to their inherent anisotropic properties, subwavelength gratings act as birefringent material. This property has been exploited for the creation of many devices, such as polarizers, polarization beam splitters, and even polarization-independent devices [9].

1.7 Application of III-V Semiconductors in Optical Signal Processing

There are many processes that need to be realized optically in order to have a fully functional and complete optical signal processing PIC. This section goes over some of the most important of such devices along with examples of how they can be implemented using III-V semiconductors.

1.7.1 Nonlinear Ring Resonators

Ring resonators are arguably one of the most important and versatile optical devices for conducting signal processing in the optical domain. When ring resonators are engineered to have zero or anomalous GVD and are created from nonlinear material, such as AlGaAs and InP, they can be used for frequency comb generation; when a laser source with a single frequency component enters a nonlinear ring resonator made from a $\chi^{(3)}$ material (as illustrated in Fig. 1.21), FWM happens and as a result we can obtain a broad spectrum of equidistant frequency components at our output which is called a frequency comb [7]. Frequency comb generation is useful for optical signal processing in many ways. For example, it can be used as a source for wavelength-division-multiplexing (WDM) systems [33], and it can also be used as an optical clock or an optical ruler for precise frequency measurements [7].

AlGaAs-on-insulator microring resonators have demonstrated highly efficient frequency comb generation at record-low threshold powers [30]. The

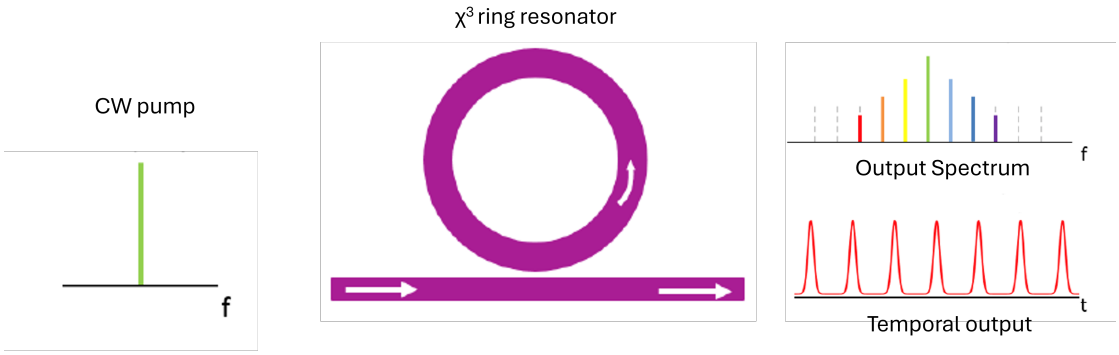


Figure 1.21: Schematic illustration for frequency comb generation in a microring resonator.
Source: [7]

microring resonators realized quality factors up to 3.52×10^6 and finesses as high as 1.4×10^4 when the ring radius was 143 μm. A ring radius of 28 μm resulted in a Q-factor of 3.14×10^6. In general, the AlGaAs-on-insulator platform's nonlinear performance has been shown to outperform other AlGaAs platforms that have been studied thus far [7]. As a comparison, there is a recent study [34] of silicon-on-insulator (SOI) microring resonators with bend radii around 50 μm that reports a quality factor of approximately 2 x 10^6 and a finesse around 1100, which is claimed to be the highest value ever reported for the SOI platform in the telecommunication band.

Aside from ring resonators, frequency comb generation can also occur in nanowaveguides with high modal confinement and small effective mode areas. A single highly nonlinear AlGaAs-on-insulator nanowaveguide has been used to achieve parallel data transmission using a single input laser source [35]. The frequency comb, which acts as a collection of SDM/WDM channels, carries a total of 661 Tb/s over 2,400 parallel channels. Using such a frequency comb as a source of WDM systems can reduce the need for multiple laser sources at different frequencies to a single pump laser [35]. Furthermore, the generated frequency combs are inherently phase coherent, which is an advantage for use in coherent transmission systems [33]. Also, such a system could be easily integrated on a photonic chip based on III-V material which would make the WDM source a part of a compact optical module with several functionalities in one.

In general, nonlinear microring resonators can be used as building blocks for several other optical signal processing modules, such as optical switches, multiplexers, modulators, and optical logic gates. They are also useful for integrated circuits due to their compact size. Their small dimensions and small effective mode area also significantly reduce the threshold power required for

efficient nonlinear processes, making it sometimes as low as a few milliwatts (mW) [36].

1.7.2 Wavelength Conversion and Amplification

Wavelength converters are essential for realizing signal processing because they allow the up-conversion and down-conversion of the operating frequency of our information-carrying beams of light. This is a critical function for WDM systems because they need to be able to manipulate the carrier frequency of optical signals throughout the communication network. As mentioned in Section 1.2, we can manipulate the wavelength of light using several nonlinear processes such as FWM, SHG, SFG, and DFG. For example, the first demonstration of all-optical wavelength conversion for 256-QAM (quadrature amplitude modulation) signals was done using AlGaAs-on-insulator waveguides [37]. In this study, the researchers were able to achieve wavelength conversions of the 256-QAM signal over the entire optical C-band with high efficiency and at 10 Gb/s data rates. This illustrates that high-capacity modulation formats are compatible with optical wavelength conversions using III-V semiconductors.

Signal amplification is another essential operation for any optical signal processing PIC. A popular nonlinear device that is used for optical amplification is called an optical parametric amplifier (OPA). Optical parametric amplification can occur using either second-order nonlinearities or third-order nonlinearities of a material [10]. FWM is actually one way that third-order nonlinearities can lead to optical parametric amplification. In the case of FWM, a signal photon (refer to Fig. 1.1) is generated for every two pump photons that are input into the system. The signal (which carries information) and pump beams are both present at the input of the device, but one gets attenuated while the other is amplified in the nonlinear medium. The presence of the signal photons from the beginning of the FWM process is what guarantees the generation of more signal photons (i.e. amplification) through the mechanism of stimulated emission [10].

In the last two decades, III-V compounds have shown excellent results when used for optical amplifiers and are a popular choice of semiconductor optical amplifiers (SOAs). For example, a recent study [38] reports optical parametric amplification using $\chi^{(2)}$ nonlinearities in AlGaAs waveguides with more than 18 dBs of gain for both TE and TM modes. This polarization-insensitive gain was reported for wavelengths around 1550 nm. Nonlinear media that can be used for $\chi^{(2)}$ phenomena have a power consumption advantage over those whose lowest possible nonlinearity is $\chi^{(3)}$; this is because the second-order nonlinear effects

require a lower intensity threshold compared to third-order processes [10]. Thus, AlGaAs has a great advantage over semiconductors that have no $\chi^{(2)}$ coefficient (like silicon).

1.7.3 Optical Modulation

Signal modulation is another functionality that needs to be performed optically in order to realize fully functional optical signal processing modules. Different types of optical modulation techniques exist, but two of the most important ones are electro-optic modulators (EOM) and all-optical modulators [39].

EOM can be achieved in a material using either the Pockels effect or the Kerr effect [39]. The two processes are similar, but one depends on $\chi^{(2)}$ while the other is related to $\chi^{(3)}$. In both situations, the modulation happens by applying an external electric field to the material which induces a change in the refractive index [39]. This modulation of the medium's refractive index is what modulates the incident light. In practice, EOM is usually done using the Pockels effect since it requires smaller electric field strengths for the same level of response [39]. This means EOMs usually require materials with strong second-order nonlinearity, such as AlGaAs.

EOMs inherently modulate the phase of light waves that propagate through the medium and not the amplitude; however, placing the EOM medium in an interferometric configuration, like a Mach–Zehnder interferometer (MZI), can also modulate the amplitude of the input beam. This is simply done by controlling the phase difference between the two arms of the interferometer and thus the interference pattern at the output [39].

As their name suggests, all-optical modulators can modulate an input beam (usually called the signal) using a control beam (usually referred to as a pump), and thereby bypass the need for electro-optic conversions in the medium [39]. This makes the modulation faster and reduces power consumption.

III-V semiconductors have been used extensively for both optical modulation and switching functions due to their inherent high nonlinearities, direct bandgap, and high carrier mobility which can lead to faster modulation speeds [39], [40], [41]. However, a lot of research in all-optical modulation is currently being focused on using lithium niobate ($LiNbO_3$) [42] or creating hybrid structures with silicon and III-V compounds or 2D material [39], [43].

III-V materials have been successfully used for optical modulation in many device configurations. For example, InP-based PICs have been used to construct ring-assisted Mach-Zehnder interferometer (RAMZI) modulators, where the

generated frequency comb is used as the laser source. The devices under study were able to either modulate all frequency combs with the same modulation signal or to modulate each comb separately. Such devices show the potential of frequency combs to be used as sources for WDM systems. These modulators are also useful for directly modulating radio frequency (RF) signals onto optical waves [40].

To take advantage of the CMOS-compatible manufacturing process of silicon photonics, some researchers integrate III-V material with silicon in an attempt to gain the benefits of both materials [39]. One example of such an approach is the heterogeneous integration of InP electro-absorption modulators (EAM) with silicon waveguides [41]. The active modulation region of the device consists of an InP-based ridge waveguide that contains multi-quantum-well layers. These layers are connected to electrodes which can control the modulation by manipulating the absorption properties of the InP waveguide. The integrated EAM modulators under study were able to demonstrate high data transmission rates, with the ability to modulate signals for both return-to-zero On-Off Keying (RZ-OOK) and pulse-amplitude modulation (PAM). The demonstrated modulations include 256 Gb/s OOK, 340 Gb/s PAM4, 360 Gb/s PAM8, and 375 Gb/s PAM6 [41].

Furthermore, optical switching based on InP photonic-crystal nanocavities is showing progress in ultrafast switching and has already been demonstrated for all-optical modulation of a 10 Gb/s RZ-OOK data signal [44].

1.7.4 Logic Gates

Optical logic gates are an integral building block for optical computing and signal processing. Many different nonlinear effects and configurations have been used to demonstrate different logic functions thus far, but a popular technique is the use of FWM in microring resonators [45].

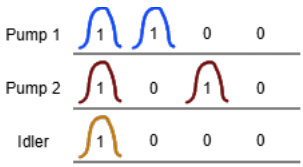


Figure 1.22: Basic principle of an optical logical AND gate.

The working principle behind optical AND gates realized through FWM inside microring resonators is quite simple. As shown in Fig. 1.22, the two pump beams acting as our logical '1' input states interact in the ring resonator through FWM and generate the idler beams which are the logical '1' output state. The

Table 1.2: Data Rates for Signal Processing Devices

Device	Function	Bit Rate [Gb/s]	Ref.
DSP (assuming state-of-the-art)	all signal processing	800 - 1600	[46]
AlGaAs-on-insulator nanowaveguide	WDM source	661000	[35]
AlGaAs-on-insulator waveguide	wavelength conversion	10	[37]
InP EAM	modulation	256 - 375	[41]
InGaAsP/InP microring resonator	AND logic gate	160	[47]

strength of the idler beams in FWM is proportional to the product of the input pump intensities. Thus, when one or both of the pump beams are weak or turned off, the idler beams will be either very weak or non-existent, which corresponds to a logical '0' at the output of the FWM device [45]. FWM optical AND gates have been implemented in devices based on III-V material, such as InGaAsP/InP microring resonators, demonstrating an operating bit rate of 160 Gb/s for the RZ modulation format [47].

In general, the implementation of different optical logic gates using III-V semiconductors can be accomplished in a variety of ways using different optical and electrical properties that this family of materials possesses. SOAs fabricated with III-V material can be used in interferometric architectures such as MZIs and Ultrafast Nonlinear Interferometers (UNIs) to implement logic gates through nonlinear effects like cross-gain-modulation and cross-phase modulation [48]. For example, XOR gates with operating speeds as high as 40 Gb/s and parity generators operating up to 160 Gb/s have been demonstrated using SOA-MZI structures [48]. Numerical studies from the same research suggest that an optical XOR gate based on quantum-dot SOA-MZI structures and optical pumping could achieve operating bit rates up to 4.1 Tb/s.

Another method for implementing optical logic functions is based on using carrier injection in microring resonators made from materials like GaAs and InP to realize logic operations such as OR, AND, NAND, and NOR gates [49]. This has been done by applying a bias to p-i-n diode structures embedded in the ring, which changes the refractive index of the resonator and alters the amount of free-carrier absorption (FCA).

Table 1.2 summarizes some of the optical signal processing devices that were mentioned along with their maximum achievable data rates. The transmission speed for a state-of-the-art digital signal processing (DSP) module used in high-speed optical communication networks is also provided as a reference.

Thus far, this introductory chapter has established the theoretical background and motivation for the research presented in the remainder of the thesis. To summarize, the fundamental principles of nonlinear optics, waveguiding theory, and meta-waveguide engineering were discussed, and the advantages of using III-V semiconductors such as AlGaAs were highlighted. The choice of III-V material was further motivated by the preceding discussion of its applications in optical signal processing. The next subsection provides the outline for the rest of the thesis.

1.8 Thesis Outline

The following thesis chapters focus on a specific category of photonic device designed for this project. Chapter 2 focuses on my proposed SWG waveguide designs for the chosen material platform along with their simulation results. This chapter also explains the design methodology used for creating the structures which includes the effective medium theory and unit cell bandstructure calculations. In Chapter 3, I present my design and simulation results for a fiber-to-chip AlGaAs-OI SWG edge coupler, while Chapter 4 is dedicated to the design of different SWG micro-ring resonators. As the physical experimental side of the project, in Chapter 5 I discuss the laboratory method and physical results derived from a prefabricated SOI meta-waveguide micro-ring resonator received from the NRC. To the best of my knowledge, these experiments are the first demonstration of FWM in Huygens' ring resonators. Finally, Chapter 6 provides a summary and conclusion of the work done in this thesis in addition to the future work that can be done by continuing this project.

Chapter 2

AlGaAs-OI Subwavelength Grating Waveguides

Building upon the theoretical foundations established in the introductory chapter, this section focuses on the design and computational analysis of AlGaAs-OI SWG waveguides. This thesis relies heavily on computational modeling and simulations through commercial software that employ numerical methods for solving Maxwell's equations. Therefore, I begin this chapter by providing a detailed overview of the general simulation methodology, including the relevant computational methods and important simulation settings. I then conclude with a summary of the design and simulation results for four distinct AlGaAs-OI SWG waveguide geometries, categorized by their core heights and cladding materials. One of the primary purposes of this chapter is to establish a systematic design methodology for SWG devices, and to have a set of functional waveguide designs for optical routing in integrated photonic circuits. These SWG waveguide designs can also serve as the building blocks for the more complex optical devices explored in subsequent chapters.

2.1 Methodology

2.1.1 Software and Hardware Resources

The numerical methods used for simulating the optical devices in this thesis were mainly the FDTD and finite-difference eigenmode (FDE) methods. While FDTD solves for Maxwell's equations in the time domain, FDE is a frequency-domain method used for calculating the possible electric and magnetic spatial profiles (the eigenmodes) in a device at specified frequencies. This is done by taking a cross section of the waveguide, thus FDE is inherently a 2D method and assumes the structure does not change locally along the propagation direction. For this project, the computational simulations were mostly conducted using

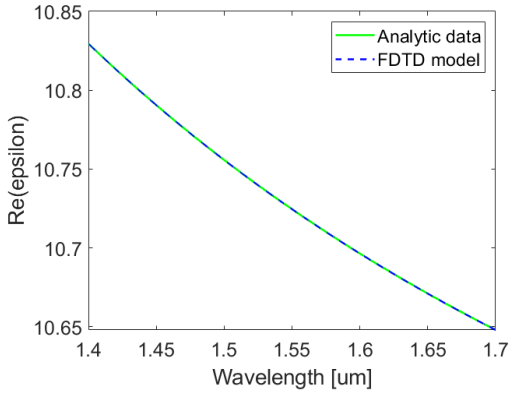
the Lumerical FDTD and Lumerical MODE solvers from the Ansys Lumerical version 2024 R1, and were run on a Windows 11 Enterprise desktop computer with 64 GB of RAM and a 13th Gen Intel(R) i9 CPU with 24 cores.

Material Fit

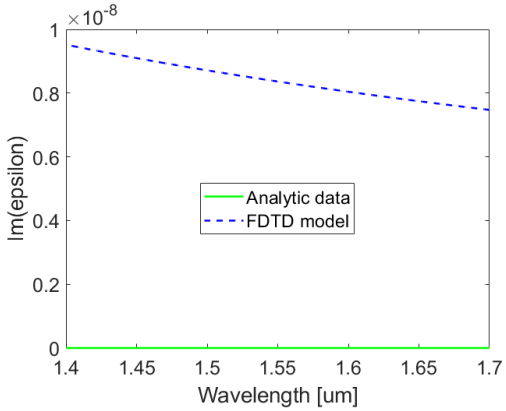
An important aspect of optical device simulations is the modeling of the structure's physical material, especially in the core waveguiding regions. The chosen semiconductor medium for the devices in this study is $Al_{0.18}Ga_{0.82}As$. Ansys Lumerical does not provide AlGaAs in the default material database, but they do provide a script and graphical user interface for adding ternary and quaternary III-V semiconductors to the database with the option of choosing among a few available theoretical models [50]. However, only the Adachi [51] and the more simplified model by Mustafa Güden and Joachim Piprek [52] are available for AlGaAs in this toolbox. Thus, instead of using this Lumerical function I use our own Lumerical material database file created in our group with an analytical expression for $Al_{0.18}Ga_{0.82}As$ based on the semi-empirical model derived by Gehrsitz [53]. This model results in more accurate refractive index values for $Al_{0.18}Ga_{0.82}As$ in the telecommunication C-band.

The predefined analytical material model is not what the FDTD and FDE solvers actually use for running the simulation. In reality, these solvers actually perform a multi-coefficient fit to the data given in the material database (which could be either physical experimental data or analytical sample points like our case). This multi-coefficient fit is necessary for the solvers to properly calculate dispersion curves and for accurate time-domain simulations. This fitting ensures that the mathematical model is smooth and physically causal by obeying the Kramers-Kronig relations. However, this causality condition can actually result in a very small imaginary refractive index value in the material fit, even though the material data assumed zero absorption far away from the bandgap and thus a purely real refractive index. Fig. 2.1 shows the Lumerical FDTD solver's multi-coefficient fit for $Al_{0.18}Ga_{0.82}As$ in the telecommunication C-band range when the fit tolerance is 0.01 or 0.1. One can try to get a better material fit by decreasing the tolerance and increasing the number of coefficients until a reasonable fitting is achieved, or by increasing the simulation bandwidth, but the latter may result in much larger simulation times. The default fit tolerance used in most of my simulations is actually 0.1, since it results in a zero imaginary part for the dielectric constant, thereby preventing nonphysical optical gain in the FDTD simulations. The trade-off is that the refractive index of the FDTD model becomes constant over this wavelength range and is only truly accurate around 1550 nm.

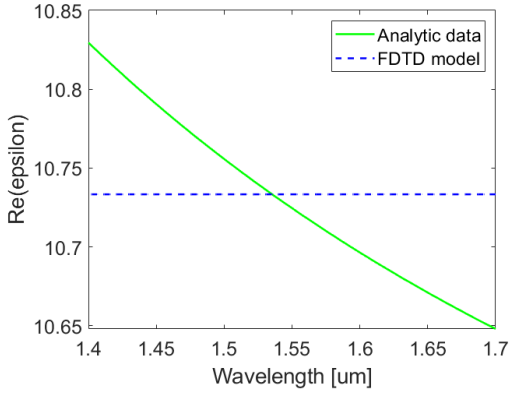
Since 1550 nm is often the wavelength point of interest for my simulations, this is a valid approximation. Preventing this artificial gain is especially important when simulating resonators, since it can result in a diverging simulation. Some simulations, such as the photonic band-structure calculations later described in this chapter, require highly accurate refractive index models; for those instances the simulation bandwidth was increased and an accurate fit to the refractive index is used as shown in Fig. 2.1e.



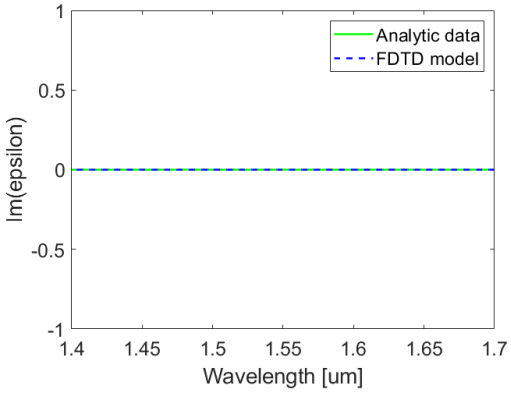
(a) Real part of the dielectric constant when the fit tolerance is 0.01.



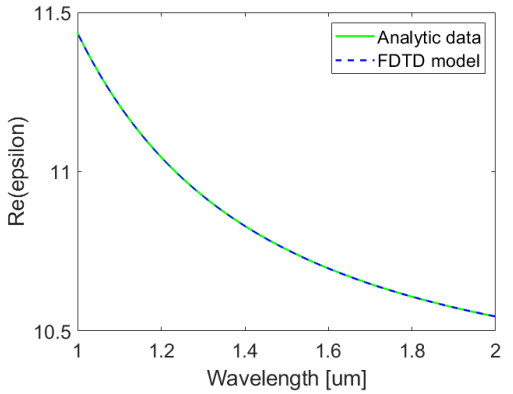
(b) Imaginary part of the dielectric constant when the fit tolerance is 0.01.



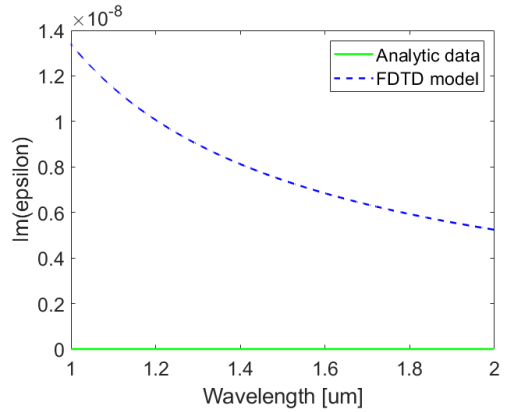
(c) Real part of the dielectric constant when the fit tolerance is 0.1.



(d) Imaginary part of the dielectric constant when the fit tolerance is 0.1.



(e) Real part of the dielectric constant when the fit tolerance is 0.1 and the simulation bandwidth is increased.



(f) Imaginary part of the dielectric constant when the fit tolerance is 0.1 and the simulation bandwidth is increased.

Figure 2.1: Multi-coefficient model fit to our analytical $Al_{0.18}Ga_{0.82}As$ data in Ansys Lumerical.

Boundary Conditions

Unlike a physical laboratory setup where we need not worry about boundary conditions and simply observe how the light waves behave in the medium, an

optical simulation relies heavily on the defined boundaries. Choosing the correct simulation environment is paramount for photonic simulations since they have drastic impacts on the outputs of Maxwell's equations. The most commonly used boundary conditions are the perfectly-matched layer (PML), perfect electrical conductor (PEC), periodic, and periodic Bloch boundary conditions. The PML boundary is a highly absorbent layer that is almost always the chosen boundary condition when simulating full optical components, because it can mimic an infinitely large free space where radiating and scattered waves move away from the device instead of getting reflected back into the simulation domain and interfering with the guided modes or sources. It is similar to performing an experiment on a free-space optical table in a laboratory. On the other hand, the PEC boundary enforces a zero tangential electric field and fully reflects all incident electromagnetic waves. It is commonly used for simulating ideal metallic surfaces. The two periodic boundary conditions are both used for devices that have periodic structures, but the periodic Bloch boundary condition makes sure that the complex phase of the wavefunction is not constantly repeated as it propagates through the device and actually gains a complex phase factor. Getting the boundary condition settings correct is one of the most important things for making sure the simulated results actually make physical sense.

Convergence Testing

Convergence testing is another important part of computational simulations and is one major difference between conducting experiments in the physical world versus a computer. We must have tests and procedures in place that can differentiate simulation artifacts from solutions that correspond to reality. Convergence testing is the act of making simulation setting parameters more accurate at the cost of being more computationally expensive until the final simulation results converge and no longer significantly change with added accuracy [54]. Making the simulation mesh finer until the decrease in step size no longer makes a significant difference in output is one such example of convergence testing. The convergence testing for the AlGaAs-OI meta-waveguides is showcased for several important simulation settings such as the mesh size, as shown in Fig. 2.2. The convergence testing of the number of PML layers in Lumerical FDTD and mesh accuracy setting are given in Fig. 2.3 and Fig. 2.4, respectively. The SWG waveguide simulations always finished with an auto-shutoff status, meaning they automatically terminated when the electromagnetic energy in the simulation domain reached the threshold value that indicates no more light was present

in the simulation. Thus, no convergence testing was deemed necessary for the time duration of these simulations.

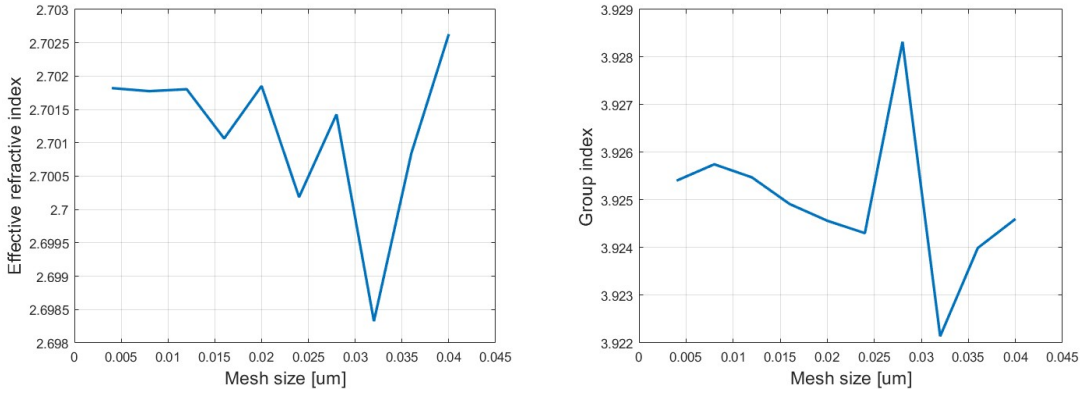


Figure 2.2: The effect of increasing cross-sectional mesh size on (a) mode effective index and (b) group index at 1550 nm using the FDE Lumerical solver.

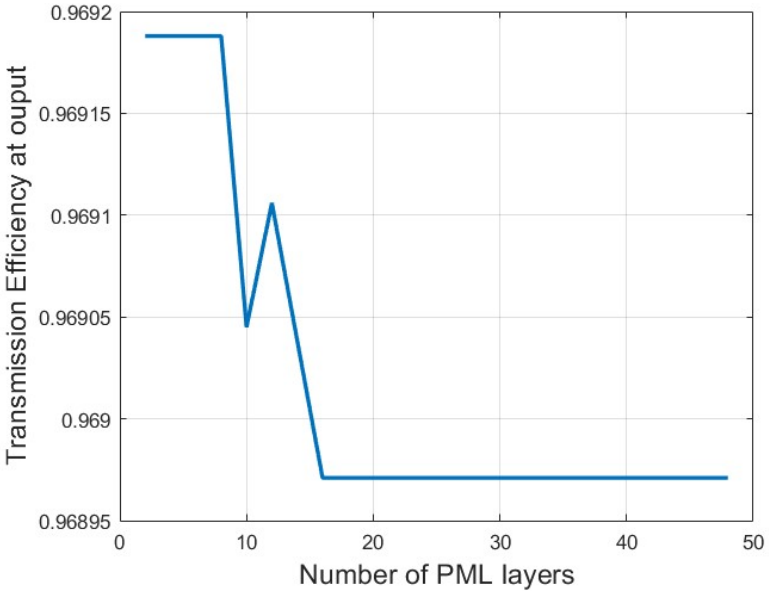


Figure 2.3: The effect of increasing number of PML layers in FDTD simulation for AlGaAs SWG waveguides.

2.1.2 2D Modal Analysis

The first step for designing the SWG waveguides was performing preliminary parameter sweeps using the Lumerical FDE solver to obtain a range of optimal dimensions. Since this solver only considers a 2D cross-section of the device, the

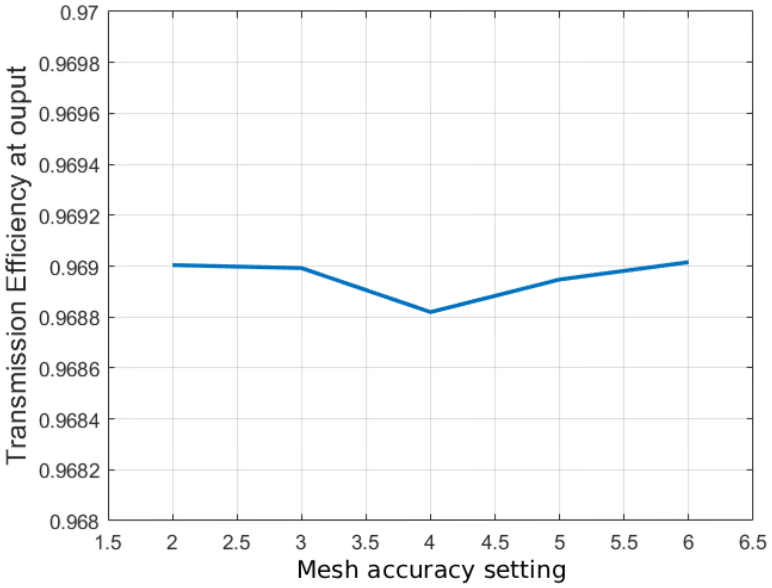


Figure 2.4: The effect of increasing mesh accuracy in FDTD simulation settings for the AlGaAs SWG waveguides.

grating feature of the waveguide must be approximated by an analogous continuous medium. This was achieved by using the effective medium theory [55], where the refractive index of the periodic waveguide core is approximated by:

$$n^2 = (a/\Lambda)n^2_{\text{AlGaAs}} + (1 - a/\Lambda)n^2_{\text{clad}} = \delta n^2_{\text{AlGaAs}} + (1 - \delta)n^2_{\text{clad}}, \tag{2.1}$$

where δ is the duty cycle of the SWG waveguide. Thus, by fixing the duty cycle of the grating I can approximate the refractive index of the SWG waveguide as long as the pitch is small enough to be in the deep subwavelength regime for 1550 nm light.

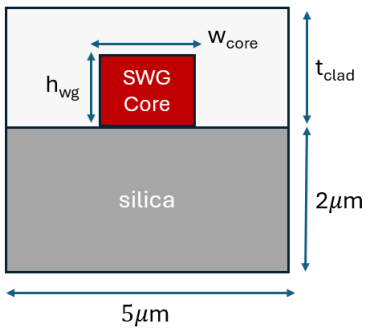


Figure 2.5: Schematic 2D cross-section of the SWG waveguide

When designing integrated photonic devices both the fabrication limitations and desired performance should be considered for determining the design criteria. One design constraint for these waveguides was their height, h_{wg}. The height

of the AlGaAs waveguide core was limited to either 200 nm or 500 nm based on the samples that will be procured by the group in the future and used for device fabrication. Thus, the parameter sweeps were limited to the width of the waveguide core, w_{core}, and the thickness of the upper cladding, t_{clad}, in addition to the duty cycle. The duty cycle was varied from 20% to 100% (corresponding to a continuous waveguide), and for each duty cycle the w_{core} and t_{clad} were swept from 0.1 – 0.5 µm and h_{wg} – 1.2 µm, respectively. Another degree of freedom was the choice of either silica or air as the upper cladding, so the parameter sweeps were done for each case separately. For each simulation, the Lumerical FDE solver calculates the full modal properties of the waveguide, such as the mode effective index, n_{eff}, the group index, n_{g}, and the effective mode area, A_{eff}. The following figures are example results from the conducted parameter sweeps.

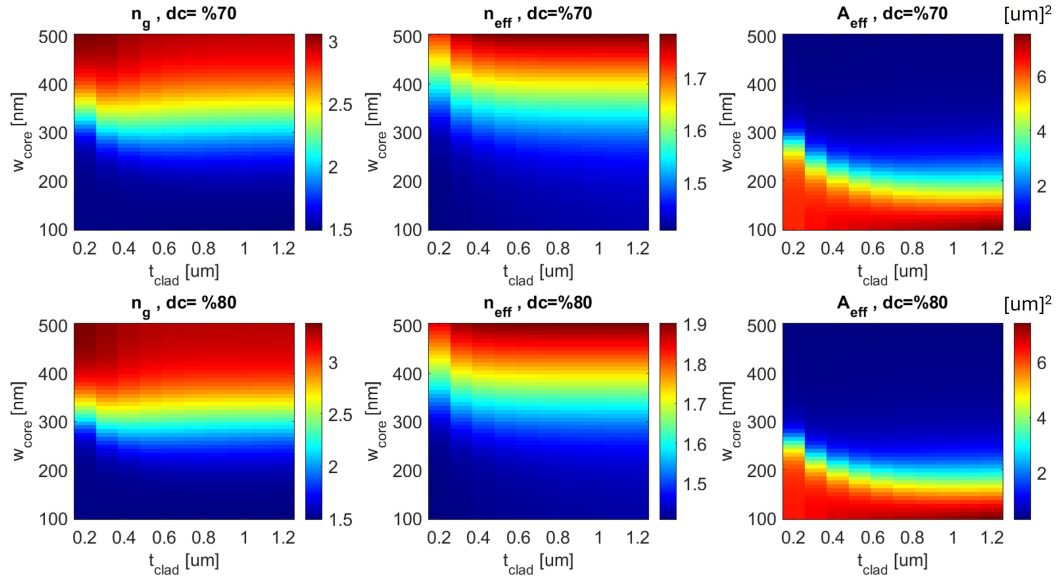
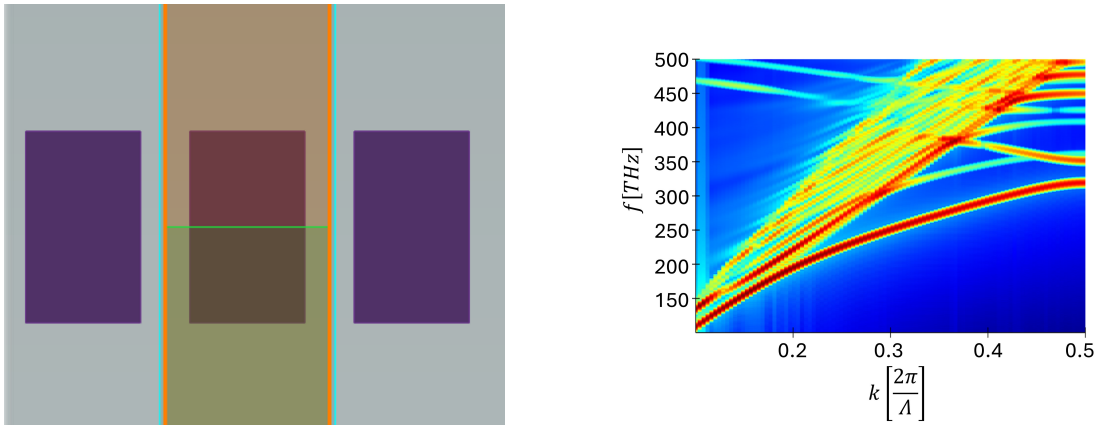


Figure 2.6: The parameter sweep results for the group effective index, mode effective index and the effective mode area when the duty cycle is 70% and 80%. The waveguide height for these simulations is 200 nm and the upper cladding is silica.

The parameters that were used in the final designs were chosen such that the mode effective index is larger than the cladding index of 1.44, while also being larger than 1.55 in order to reduce substrate leakage losses [56]. For example, for the case of 200 nm height and silica cladding used in Fig. 2.6, the waveguide widths were kept above 0.3 µm to reduce potential losses.

2.1.3 Photonic Band-structure Calculation

The next step after the 2D approximation and modal analysis is to analyze the SWG structure more accurately with its full features. Thus, the photonic band-structure of the SWG waveguide designs were calculated using full 3D FDTD simulations of the unit cell, where only a single period of the waveguide is simulated as shown in Fig. 2.7. It is important to note that the boundary conditions for these simulations must be the Bloch-periodic boundary conditions in the propagation direction.



(a) **(b)**

Figure 2.7: The (a) unit cell of an SWG waveguide and (b) its simulated photonic band-structure.

In the pursuit of an optimal value for the SWG pitch size, several band-structure simulations were conducted. The desired behaviour of the band-structure depends on the application at hand. For the SWG waveguides that are meant for regular linear transmission the goal is low transmission loss and no back-scattering or reflection of light, so I need a band-structure where the operating wavelength range is placed within the subwavelength regime and far away from the photonic bandgap. The subwavelength regime corresponds to the linear region of the first-order band in the band-diagrams illustrated in Fig. 2.8. For meta-waveguides optimized for nonlinear phenomena, regions of anomalous dispersion are desired, which makes the Huygens' regime ideal. The Huygens' band corresponds to the guided modes right on top of the photonic bandgap. For slow light applications, the operating wavelength range should fall within the flat region right below the bandgap in the dispersion band-diagram.

The effect of solely varying the pitch or duty cycle of the unit cell is illustrated with a few examples in Fig. 2.8. Increasing the pitch results in the band diagram

curves shifting downwards. This is because the higher frequency (smaller wavelength) waves are no longer sufficiently larger than the waveguide structure and are not experiencing a "continuous" medium; thus, they experience heavy dissipation and no longer have guided modes below the bandgap. It is also to be expected that increasing the duty cycle reduces the gap in the band-structure as the structure approaches a more continuous medium. Based on these tests a pitch size of 0.2 µm was chosen for the waveguides in this study.

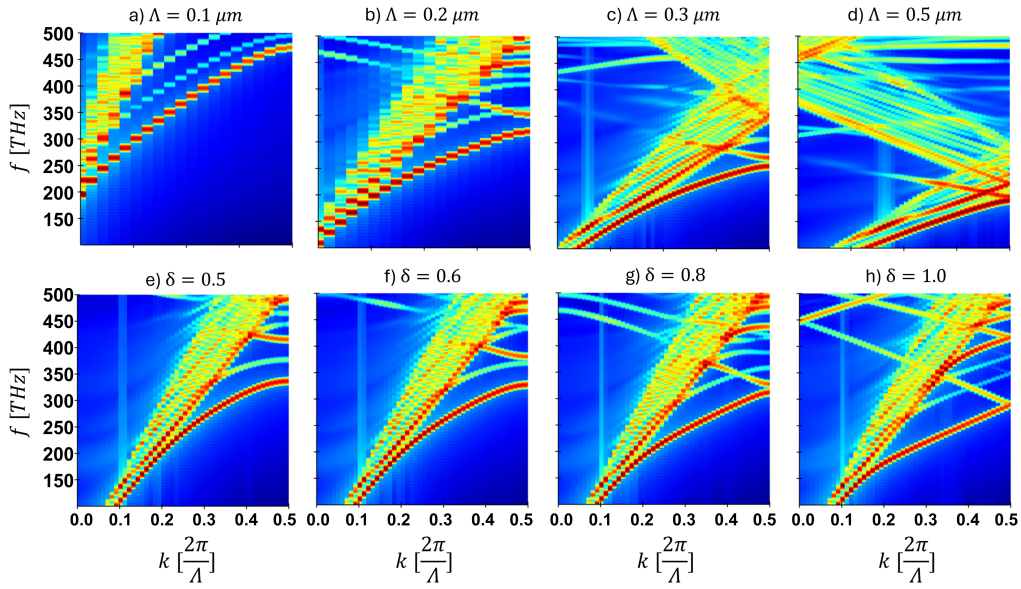


Figure 2.8: The effect of varying either the a)-d) pitch or e)-h) duty cycle

After obtaining a reasonable band-structure for the unit cell where our operating wavelength is properly within the subwavelength regime, the next step is extracting the excited Bloch mode at 1550 nm. This is done by pinpointing the k-vector that corresponds to the desired Bloch mode in the band-structure and using this value as the source k-vector in the Lumerical FDTD settings. The mode profile extracted from the cross-section of the unit cell (shown in Fig. 2.9) is then used as a custom Bloch mode source which will get injected in the complete SWG waveguide and should propagate with low loss.

2.2 Design and Simulation Results

The aforementioned design process was used for four separate groups of waveguides differentiated by their combination of AlGaAs height and cladding material. These categories were decided based on the future AlGaAs samples that will be available to the group for device fabrication and testing. The dimensions

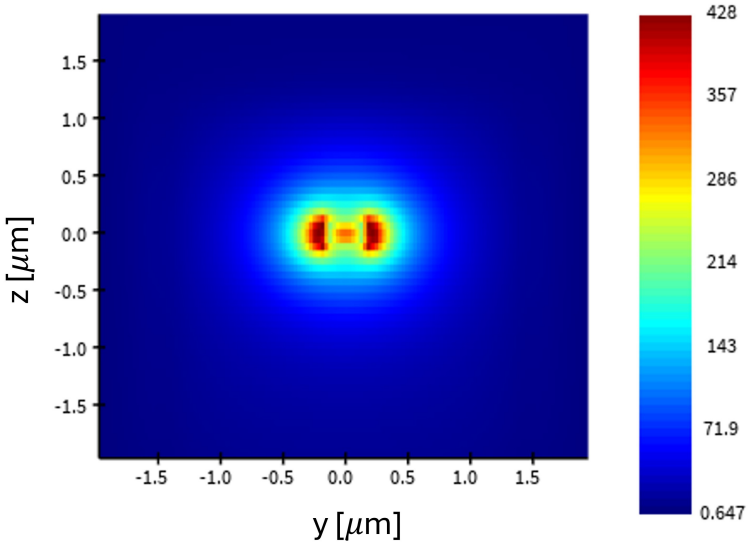
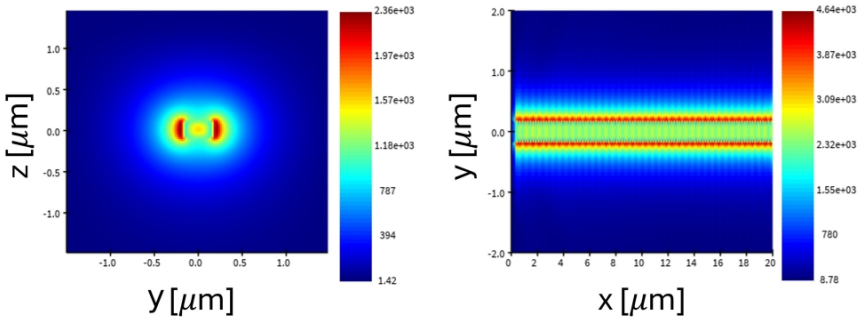


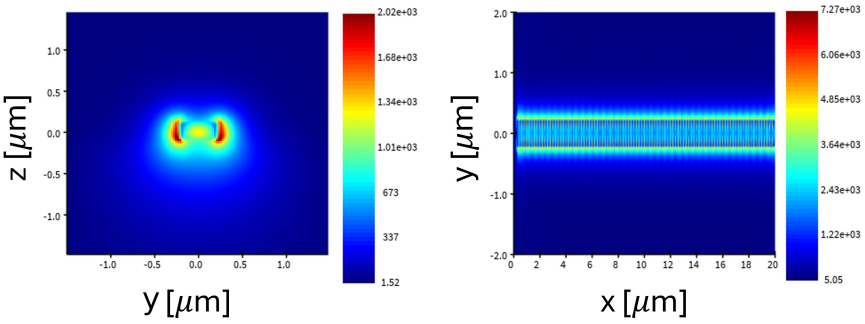
Figure 2.9: The mode profile of the excited Bloch mode at 1550 nm at the centre of the unit cell shown in Fig. 2.7. The colourbar represents the electric field magnitude in arbitrary units.

and measured performance of an example design from each category are provided in Table 2.1 and Fig. 2.10. All the waveguide simulations were conducted with a mesh accuracy level of 2, a maximum mesh step size of 0.0214 μm in all three dimensions (using mesh override), and a time step of 0.0403573 fs. The transmission efficiencies reported in Table 2.1 are over a span of 40 μm. The duty cycle required for reducing substrate leakage is larger for the waveguide with no upper cladding because the core is now comprised of AlGaAs and a much lower refractive index medium (air). Despite the larger duty cycle the air cladding designs still demonstrate lower transmission efficiency for their fundamental Bloch mode at the output of the device. The asymmetry in the vertical dimension of the waveguide resulting from two different cladding materials makes the Bloch mode asymmetrical as well, as seen in Fig. 2.10; the electric field profile is more intense near the substrate boundary due to the higher refractive index of silica compared to air and this itself results in more losses due to light leaking into the substrate material.

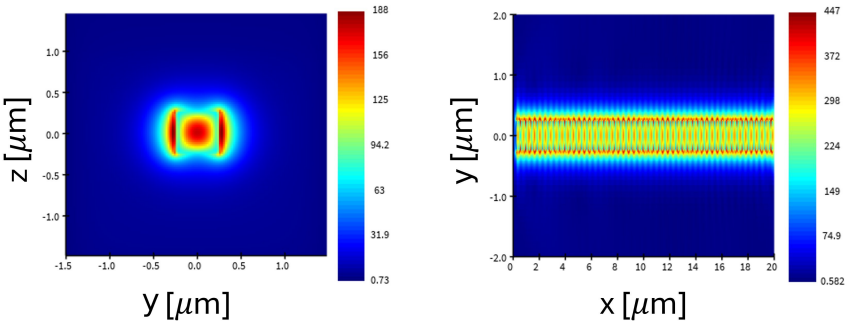
Despite the differences in measured transmission efficiencies, all of the simulations illustrate the proper operation of the SWG waveguide designs in the subwavelength regime. As seen in Fig. 2.10, the Bloch modes propagate with minimal to no back-reflections from the grating structures, and the light treats the periodic waveguide as a continuous medium. Thus, this chapter demonstrates the successful design of AlGaAs-OI SWG waveguides for various core heights and cladding configurations.



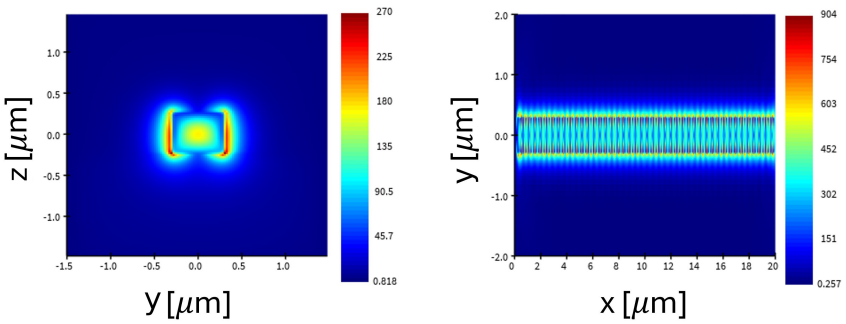
(a) Waveguide with 200 nm height and upper silica cladding.



(b) Waveguide with 200 nm height and upper air cladding.



(c) Waveguide with 500 nm height and upper silica cladding.



(d) Waveguide with 500 nm height and upper air cladding.

Figure 2.10: Bloch mode propagation in four different SWG waveguide designs.

Table 2.1: Summary of the AlGaAs-on-insulator SWG Waveguide designs

$h_{wg}[nm]$	Upper clad.	$w_{core}[\mu m]$	$t_{clad}[\mu m]$	δ	$\Lambda[\mu m]$	Transmission Efficiency [%]
200	silica	0.35	1.2	0.7	0.2	96.5
200	air	0.45	NA	0.85	0.2	89.9
500	silica	0.5	1.2	0.5	0.2	91.8
500	air	0.4	NA	0.65	0.2	83.1

A principal feature of SWG waveguides established from the methodology outlined in this chapter is the use of the grating pitch and duty cycle as extra tuning knobs for manipulating the effective refractive index. This is in contrast to conventional waveguides where the width and height are the primary means of altering the refractive index. Furthermore, the results demonstrate that symmetric index profiles, such as those using a silica upper and lower cladding, significantly reduce substrate leakage for SWG waveguides and yield higher transmission efficiencies.

To conclude, waveguides are the most fundamental component of photonic circuits, and the parameters established here form the core building blocks for the more complex devices explored in this thesis. Specifically, the SWG parameter sweeps of suitable SWG dimensions and the design methodology derived in this chapter are directly used and expanded upon in the design of the efficient fiber-to-chip edge coupler presented in Chapter 3, and the microring resonators discussed in Chapter 4.

Chapter 3

AlGaAs-OI Subwavelength Grating Edge Coupler

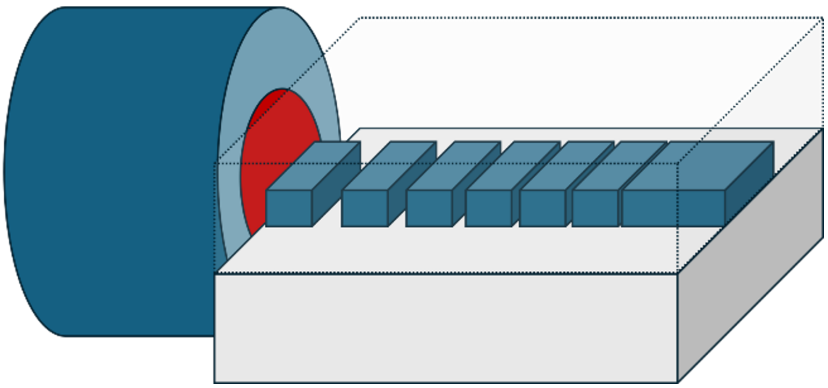


Figure 3.1: A simplified illustration of an SWG edge coupler and input fiber.

Having established the design and fundamental characteristics of AlGaAs-OI SWG waveguides in the previous chapter, which are used for routing light on-chip, the focus now shifts to using SWG structures for efficient light coupling. A crucial component for any integrated photonic circuit is the coupler used for coupling light from optical fibers into the chip. A circuit is not truly functional without an efficient method for light input and output. The most common types of couplers used for this purpose are edge couplers and surface-grating couplers, with each having its own advantages and drawbacks. As their name suggests, edge couplers are placed at the very edge of a chip and convert the much larger optical mode diameter of a fiber to the smaller mode of an on-chip waveguide. This mode conversion can be done in many ways, but incorporating an inverse-tapered waveguide is a popular choice. No matter the chosen method, all edge couplers tend to be more sensitive to fiber alignment because we are coupling into an integrated waveguide with sub-micron cross-sectional dimensions.

An alternative to the in-plane edge coupler is to use an out-of-plane coupling strategy such as a surface-grating coupler. These devices work by vertically shining the light on a Bragg diffraction grating surface in the chip which then couples and redirects it to an integrated waveguide. The surface-grating coupling mechanism is less susceptible to alignment sensitivities because instead of aligning the fiber to a waveguide facet, the fiber mode is incident from above the chip and has more coupling surface to couple into. However, edge couplers are much more broadband, while grating couplers suffer from having a smaller range of wavelengths that they can efficiently couple since their optimal radiation angle is wavelength-dependent. Thus, the edge coupler geometry was chosen for the fiber-to-chip coupler designed in this project. SWG edge couplers have already been successfully demonstrated for silicon photonics [24], [26], [27], with the best coupler achieving coupling efficiencies over 92% and a loss as low as -0.32 dB at 1550 nm [57]. To my knowledge, there has yet to be an edge coupler design for AlGaAs or AlGaAs-OI using SWG structures reported in the literature; hence, this topic is explored in this chapter of the thesis project.

The general strategy for designing an SWG edge coupler is to progressively decrease the mode effective index and increase the effective mode area along the coupler via an SWG taper to expand the waveguide mode until it matches the spot size of the optical fiber near the chip edge. To design the AlGaAs-OI SWG edge coupler, the device was divided into two sections, illustrated in Fig. 3.2, and a methodology based on the process described in [57] was utilized for achieving the adiabatic mode conversion between the fiber and rectangular integrated waveguide. The first section is the coupler tip, which is in direct contact with the optical fiber at the chip edge, and the second portion is the transition region where the mode is converted to match the continuous AlGaAs-OI waveguide in the chip. The objective was to achieve efficient coupling from an optical fiber with a mode field diameter (MFD) of 3.2 μm to a rectangular slab waveguide with a 200 nm height and 450 nm width. A standard single-mode fiber was not chosen because such fibers have an MFD around 9 – 10 μm and that results in extreme substrate leakage in devices where a 200 nm layer of AlGaAs is sitting on a 2 – 3 μm silica substrate. Thus, a more specialty fiber such as the Coherent UHNA7 single-mode fiber with a much smaller MFD of 3.2 ± 0.3 μm at 1550 nm was chosen as the input.

To successfully couple the incoming light into the chip, the boundary between the fiber and chip needs to be designed properly. The first interface of the fiber is the coupler tip; thus, ensuring mode-matching at this point is crucial for edge coupler performance. The mode overlap is achieved at the tip of the edge

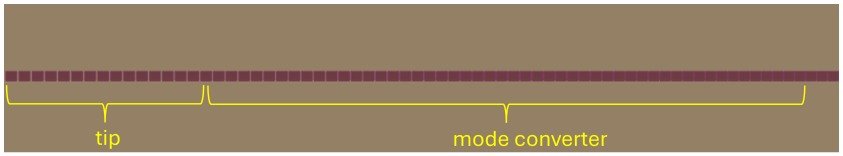


Figure 3.2: The fiber-to-chip edge coupler can be designed in two parts: one dedicated to the taper region at the tip and one for the taper section that fully transitions the inputted mode into the integrated waveguide at the coupler output.

coupler by using the Lumerical FDE solver to calculate the fundamental TE and TM modes of the optical fiber. The fundamental guided mode at the edge coupler tip is simulated using the FDE solver and the effective medium theory approximation described in Chapter 2, where the value of the duty cycle is used for estimating the effective refractive index of the waveguide as if it were a continuous slab and not a grating. To find the optimal duty cycle and width for the coupler-tip, parameter sweeps were conducted in Lumerical MODE, and the results are shown in Fig. 3.3. The modal overlap is calculated at every sweep step using Lumerical's built-in mode overlap function which determines how much of the optical power from the input mode can be coupled into the modes of the output waveguide.

As seen in Fig. 3.3, the extra degree of freedom provided by having a duty cycle makes it possible to have a broader range of tip widths available for optimal coupling. Without the subwavelength gratings, with alternating low and high refractive indices, the taper would require a smaller width in order to achieve the same large effective mode area to match the fiber mode. This is because the smaller effective refractive index at the tip is achieved through more of the mode leaking into the cladding layers and thus experiencing a lower refractive index. In the SWG case, light is already experiencing a lower refractive index in the core layer itself, and requires less leakage into the upper and lower cladding to achieve an effective index matching that of the fiber. There are several optimal points shown in Fig. 3.3, and for this device an initial duty cycle of 0.8 and accompanying tip width of 226 nm were chosen, resulting in an overlap of about 92.5% between the incoming fiber mode and the guided modes of the coupler tip. The actual duty cycle used at the beginning of the edge coupler tip was decided through more thorough 3D simulation sweeps in Lumerical FDTD.

To check the tolerance of the edge coupler to fiber alignment, a sensitivity test was conducted in Lumerical FDE by shifting the fiber mode in the y and z dimensions (propagation is along x) and calculating the subsequent modal overlap between the tip of the coupler and input fiber. From the results, shown

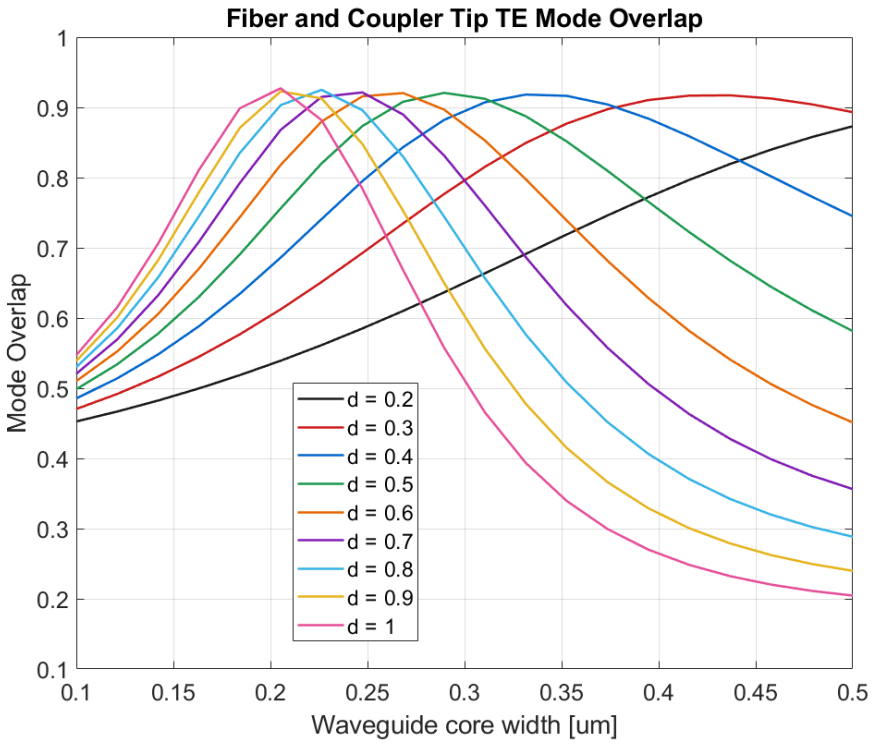
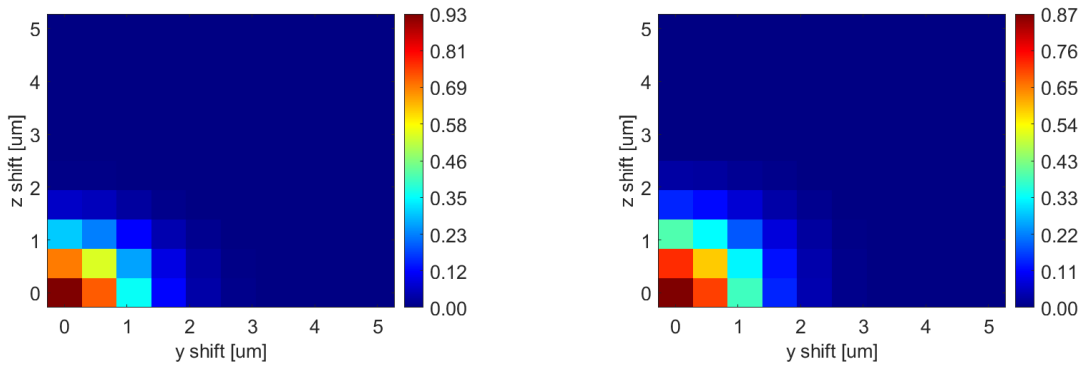


Figure 3.3: The fiber to coupler tip mode overlap calculated using Lumerical FDE and the effective medium theory approximation. The duty cycles are represented by different coloured curves.

in Fig. 3.4, it is clear that retaining high coupling efficiency is dependent on the fiber being exactly aligned to the chip edge within a sub-micron degree of tolerance.

Assuming a width of 226 nm at the coupler tip and a length of 10 µm for the taper that forms the tip section, a parameter sweep was conducted to determine the optimal duty cycle fraction of 0.8 and grating pitch of 400 nm to achieve the highest coupling efficiency at the end of the first taper. This optimization process was done assuming a pitch of 300 nm and duty cycle of 0.7 is adiabatically reached at the end of the first taper through linear chirping. This is a requirement for keeping the coupled light guided as the effective refractive index is varied to match the solid-core AlGaAs-OI wire at the end of the edge coupler.

The next section that requires careful design is the junction between the two coupler tapers. In order to minimize back-scattering and radiation losses that occur due to sudden changes in the effective refractive index of the guided modes, this junction is designed such that the volume ratio of AlGaAs to silica is the same both before and after the interface of the two tapers. This is done by adding an AlGaAs bridge waveguide between the gratings in the coupler's mode size conversion region. This waveguide bridge starts from a width of 75 nm and



(a) **(b)**

Figure 3.4: The calculated modal overlap between the fiber and edge coupler tip for both TE and TM modes as a function of fiber misalignment.



Figure 3.5: Schematic showing the parameters used in the different segments of the edge coupler design.

is increased until 450 nm as it transitions into the AlGaAs wire waveguide. The second taper of this edge coupler starts with a pitch of 300 nm and gradually reduces it to 200 nm while the duty cycle is increased from a value of 0.6 to 1 right before the solid-core waveguide is reached. The taper width in this mode-converter region is also gradually increased from 300 nm to 450 nm where it seamlessly merges into the dimensions of the AlGaAs waveguide at the output. The edge coupler design parameters are summarized in Fig. 3.5 and Table 3.1.

The simulations for this AlGaAs-OI SWG edge coupler were conducted using Lumerical 3D FDTD with a mesh accuracy setting of 3, simulation time of 2000 fs, and time step stability factor (i.e. Courant factor) of 0.99 which translates to a time step of 0.0403515 fs. The full simulation domain was $50 \times 8 \times 6$ µm and the boundary conditions were 8-layer stretched coordinate PML on all sides. This domain includes the input fiber, the edge coupler, and the conventional integrated waveguide at the output. The simulation was automatically terminated early using an auto-shutoff value of $1 \times 10^{-}5$, meaning the total electromagnetic energy in the simulation region had dropped to below 0.001% of the peak energy that was injected into the system. The propagation of the quasi-TE mode from the fiber-to-chip edge coupler is demonstrated in Fig. 3.6a, and the coupling

Table 3.1: Summary of the AlGaAs-OI SWG edge coupler design parameters

Coupler tip length	10 μm
Mode converter length	20 μm
w_1	226 nm
w_2	320 nm
w_3	300 nm
w_4	450 nm
Λ_1	400 nm
Λ_2	300 nm
Λ_3	200 nm
δ_1	0.8
δ_2	0.7
δ_3	0.6
δ_4	1
w_{b1}	75 nm
w_{b2}	450 nm

efficiency as a function of wavelength for this mode is given in Fig. 3.6b. The edge coupler was also tested for the fiber's fundamental quasi-TM mode, and the corresponding results are shown in Fig. 3.7. This AlGaAs-OI SWG edge coupler achieves a coupling efficiency as high as 90.2% (-0.45 dB loss) at 1550 nm for TE modes, and the mode conversion is fully achieved over a length as small as 30 μm. This is a significantly smaller footprint compared to the common conventional edge coupler lengths that exceed 100 μm. Furthermore, the SWG edge coupler retains a coupling efficiency above 85% for the fiber fundamental TE mode over a broad bandwidth of 200 nm centered around 1550 nm. For the fundamental TM mode, the SWG coupler undergoes -0.56 dB of loss at 1550 nm, and achieves a peak coupling efficiency of 89.4% around 1483 nm. Although the edge coupler was specifically designed for coupling TE polarization, the relatively similar dimensions for the cross-section of the coupler tip (226 nm $\times$ 200 nm) help reduce the polarization sensitivity of the device and consequently

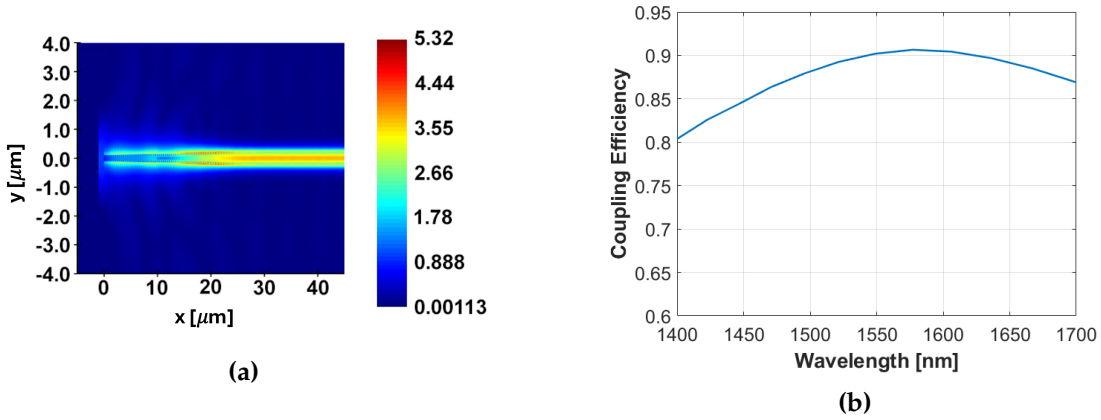


Figure 3.6: The final results for the a) forward field propagation simulation for the fundamental TE mode of the fiber entering the nanowaveguide via the edge coupler at 1550 nm and b) the coupler efficiency as a function of wavelength.

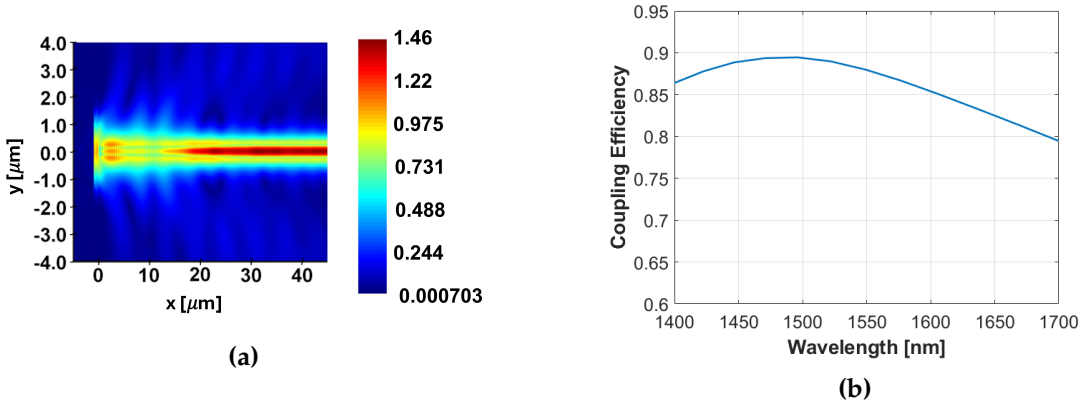


Figure 3.7: The results for the a) forward field propagation of the fiber's fundamental TM mode entering the nanowaveguide via the edge coupler at 1550 nm and b) the coupler efficiency as a function of wavelength.

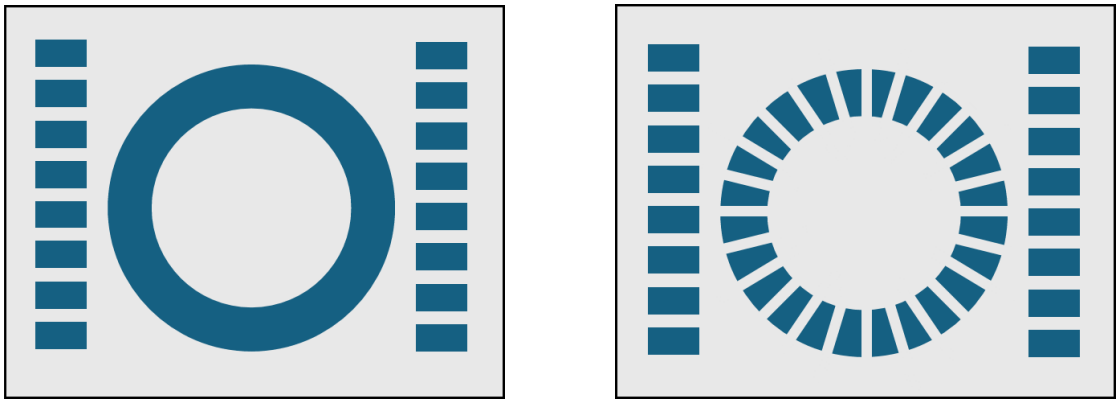
the TM modes are also adequately coupled within ∼0.1 dB of the TE case.

In summary, I have successfully demonstrated the potential of combining SWG structures with the AlGaAs-OI platform for realizing couplers that achieve high efficiencies while taking up extremely small real-estate in a photonic circuit. This was achieved by linearly chirping the grating pitch, duty cycle, and width to design an SWG taper that enables adiabatic mode expansion. With efficient fiber-to-chip coupling covered, the next chapter will explore the design of more complex integrated photonic components, specifically microring resonators, using SWG structures.

Chapter 4

AlGaAs-OI Subwavelength Grating Ring Resonators

Building on the waveguide and coupler designs presented in the preceding chapters, this chapter showcases microring resonators designed using the AlGaAs-OI platform and subwavelength engineering techniques. As previously mentioned in Chapter 1, ring resonators are a highly versatile component in PICs and have applications in both nonlinear and linear optics. In general, there are two areas where the subwavelength components can be incorporated: the bus waveguides and the ring. The choice of making only the bus or the ring SWG or the full structure being SWG depends on the application and performance that we are trying to achieve. Two possible design choices are shown in Fig. 4.1.



(a) (b)

Figure 4.1: Simple illustration of two possible scenarios for SWG ring resonator designs where (a) only the bus waveguides are SWG or (b) the full device uses SWG structures.

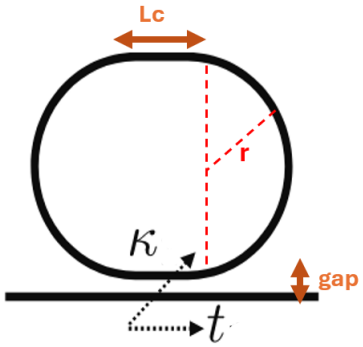


Figure 4.2: Diagram of a ring resonator. Source: Adapted from [16]

4.1 Design Methodology

If we keep the waveguide dimensions constant, the physical geometry of a ring resonator can be simply parameterized in terms of its radius (r), coupling length (L_c), and gap size, as shown in Fig. 4.2. The simulations and calculations outlined in this section all assume an AlGaAs waveguide width of 400 nm and height of 200 nm in both the bus and ring regions sandwiched between two silica cladding layers. The region where coupling occurs between the ring and bus waveguide is essentially a directional coupler, and its behaviour can be explained using coupled-mode theory, as described in Section 1.4.2. The cross-coupling coefficient, κ, and the self-coupling coefficient, t, represent the portion of light that is transferred between the coupled waveguides as opposed to staying in the bus waveguide. In the ideal case where there are no external losses and all of the light either transmits through the bus or successfully couples into the ring, the coupling coefficient is given by

$$\kappa^2 = \sin^2\left(\pi \Delta n \frac{L_c}{\lambda}\right), \tag{4.1}$$

where λ is the free-space wavelength and $\Delta n = n_1 - n_2$ is the effective refractive index difference of the very first two eigenmodes of the coupled-waveguide system between the ring and bus.

The values of n_1 and n_2 can be determined through FDE simulations in Lumerical MODE by placing two straight waveguides that represent the directional coupler region where the bus and ring are closest to each other in the 2D simulation region and calculating the first two fundamental coupled modes which represent the symmetric and anti-symmetric supermodes of the system. As always, the effective medium theory is used for approximating the refractive index of the waveguide core as a function of the duty cycle of the SWG structure.

Figs. 4.3c and 4.3d show these coupled supermodes for a ring resonator which is fully SWG and has a duty cycle of 0.8, a period of 200 nm, and a gap size of 350 nm. If the waveguides are too far apart, no coupling occurs, and the first two modes are simply isolated modes in either waveguide. The allowed gap before the coupling strength is fully diminished is directly related to the refractive index of the two waveguide cores that form the directional coupler, and since the duty cycle can directly tune the refractive index, it has a drastic effect on the coupling strength. For example, using a duty cycle of 1 (i.e. a solid-core AlGaAs waveguide) results in weaker coupling for a 350 nm gap size, as seen in Figs. 4.3e and 4.3f. Lowering the duty cycle ratio results in a lower core refractive index and thus a more delocalized mode with a larger effective mode area that can undergo easier evanescent coupling for the same gap. By varying the gap between the waveguides, the field coupling coefficient can be calculated as a function of gap size, as shown in Fig. 4.4. Even though the ring resonator in question uses point coupling, the calculations assume a coupling length of approximately four SWG unit cells, as visualized in Fig. 4.3a.

One important factor in designing a ring resonator is the losses that occur within the ring due to waveguide bending. Hence, one of the first steps of designing the SWG ring resonators was the calculation of bend losses for different radii and SWG parameters. This was done in Lumerical MODE using the FDE solver and the results are shown in Fig. 4.5. As previously described in Section 2.1.2, the effective medium theory was used for the 2D simulations of SWG structures.

The bend loss calculations are used for determining the minimum radius that can be used for SWG rings without leading to high scattering and radiation losses. The bend losses were calculated based on both radiative losses for the fundamental mode propagating through the bend and the mode mismatch that occurs when the light goes from a straight waveguide portion into a bent section. One issue with using a bent grating instead of a continuous material is the lower refractive index, so there is a limit to how low the duty cycle can be before we end up with zero guided modes.

A duty cycle of 80% with a radius of 10 μm results in a loss of about -0.02 dB per 90 degree bend. This translates to -0.08 dB loss for a full ring, and it means that approximately 97% of the light survives after one cycle through the ring. This theoretical calculation does not take into account the propagation losses due to material absorption since the material is modeled with a purely real refractive index in the simulations; however, these material losses can be assumed negligible since 1550 nm is in the transparent regime for AlGaAs and

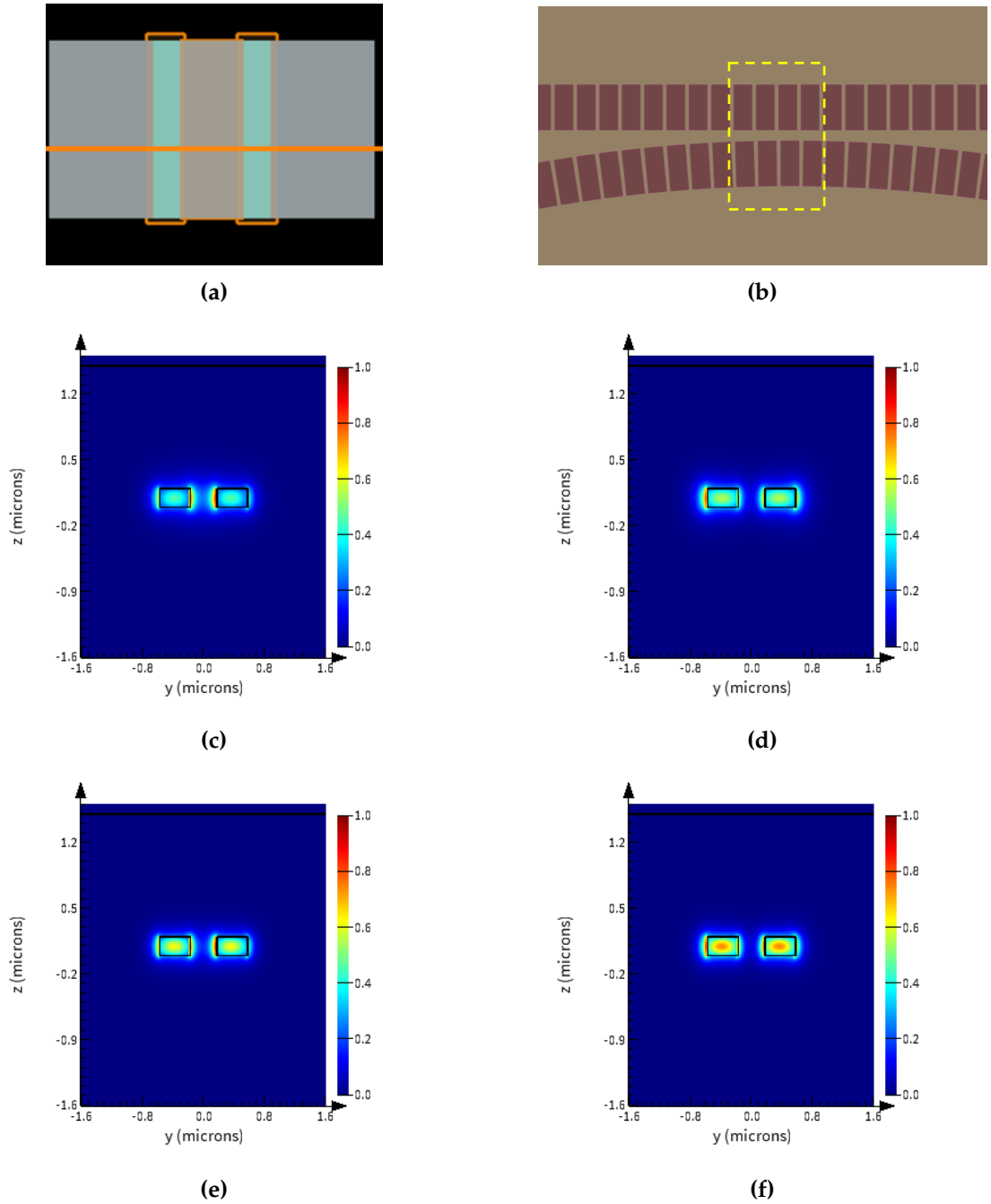


Figure 4.3: The coupling region in the (a) FDE and (b) FDTD simulation environments. The (c) symmetric and (d) anti-symmetric supermodes of the coupled system with a SWG duty cycle of 0.8 showcases stronger coupling at a gap of 350 nm compared to the (e) symmetric and (f) anti-symmetric modes of the solid-core system.

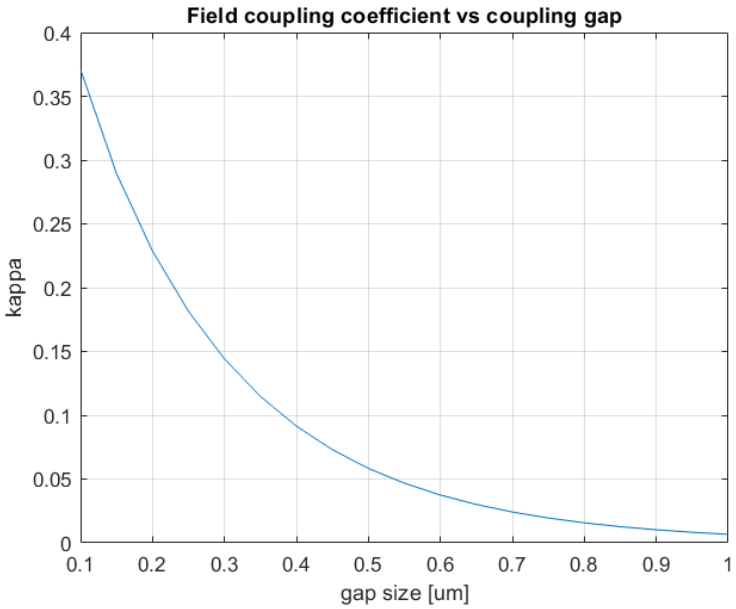


Figure 4.4: The theoretical cross-coupling coefficient for a ring and bus waveguide that are both SWG with a 0.8 duty cycle ratio and 200 nm period for a wavelength of 1550 nm.

AlGaAs-OI can have a propagation loss as low as 0.4 dB/cm even with the presence of scattering losses from sidewall roughness. Based on these 2D FDE calculations, and in order to minimize losses in the ring, a minimum radius of 10 μm was decided for the SWG ring resonator designs. As explained in Section 1.4.3, critical coupling is when the optical power that couples into the ring exactly equals the amount of power lost in one round-trip:

$$\kappa = \sqrt{1 - a^2}, \tag{4.2}$$

where a is the round-trip transmission coefficient for the ring. At resonance, this perfect balance results in complete destructive interference in the through port of the input waveguide, dropping the transmitted power to exactly zero. As mentioned above, the portion of transmitted light after one round-trip is theoretically about 97% for a ring resonator with a width of 400 nm and height of 200 nm where both the bus and ring are SWG structures with a period of 200 nm and fill factor of 0.8. With $a = 0.97$, the critical coupling for this resonant structure theoretically occurs when $\kappa \simeq 0.243$, which corresponds to a gap size around 188 nm according to the curve in Fig. 4.4. Note however that these calculations all assume an ideal solid-core ring with no external losses, and they do not take into full consideration the delocalized field effects inherent to SWG structures which enable stronger coupling at larger distances. This is why the

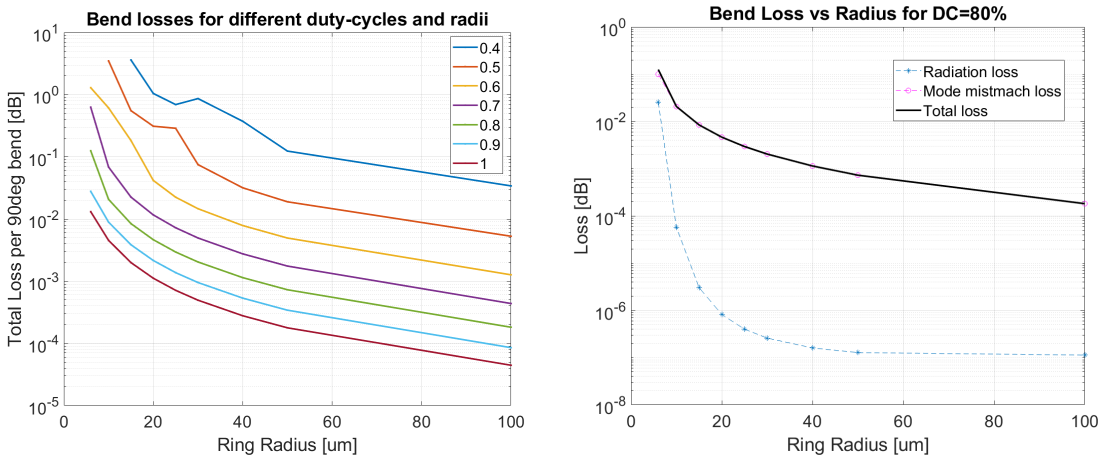


Figure 4.5: (a) Total bend loss calculations from 2D MODE simulations. The total loss is calculated from adding the mode mismatch losses from entering and exiting the bent waveguide with the radiative losses from propagating in the bend. Each curve corresponds to a different duty cycle. (b) Bend losses for an 80% duty cycle.

critical coupling observed in the next section occurs at larger gaps.

Other design parameters that affect the exact ring geometry are the desired FSR and resonance wavelengths. These parameters are already explained in Section 1.4.3; however, one nuance when designing ring resonators where the ring incorporates subwavelength structures is that the radius must be chosen such that a discrete number of SWG unit cells can properly fit in the ring circumference. Proper care should also be given to ensure that the SWG unit cells in the directional coupler are aligned to ensure proper mode overlap and coupling. The radii for the ring resonator designs provided in this chapter were calculated using the following equations.

$$\begin{cases} L = \dfrac{\lambda_0^2}{n_g FSR} \\ L = \dfrac{m\lambda_0}{n_{\text{eff}}} \end{cases} \implies \frac{\lambda_0}{FSR} = m\frac{n_g}{n_{\text{eff}}}; m \in \mathbb{Z}, \tag{4.3}$$

$$\frac{L}{\Lambda} = n; n \in \mathbb{Z} \text{ (for SWG ring)}, \tag{4.4}$$

where L is the ring circumference, n_{eff} is the effective refractive index experienced in the ring at the resonance wavelength, λ_0, and n_g is the group index in the ring at resonance.

Lastly, simulating ring resonators and obtaining physically sound results requires careful management of the simulation settings and environment. For

example, the distance between the simulation domain's PML boundaries and the resonator cavity can lead to significant errors. If the PML boundaries are too close to the structure, the electromagnetic fields can get absorbed and prematurely leave the ring, or there could be parasitic reflections that re-enter the ring from the PML boundaries. Thus, care must be taken to sufficiently increase the distance between the PML boundaries and the ring resonator until the outputted spectra and calculated Q-factors converge and stabilize. The minimum distance to use as a starting point should be no smaller than half the largest wavelength used in the simulation. Another important thing to note is that the SWG bus waveguides should be fully extended through the PML layer and not abruptly terminated. This ensures that no artificial back-reflections occur at the output boundary of the simulation.

4.2 Design and Simulation Results

4.2.1 Observing Different Coupling Regimes

Every coupling regime for a ring resonator has its uses. Filtering applications require higher extinction ratios and thus benefit from a critically coupled system, while nonlinear optical applications need high Q-factors to enhance the optical power in the ring cavity and lower the threshold power for observing nonlinear phenomena. Controlling the operating regime of the device is mostly dependent on the gap between the straight waveguide and the ring. Thus, several different SWG AlGaAs-OI ring resonators that differ only in gap size were simulated based on the theoretical loss and coupling calculations outlined above with a target FSR of 10 nm and resonances centered at 1550 nm. These SWG rings all have a radius of 12.7 μm, and SWG unit cells with a period of 200 nm and a fill factor of 0.8. They have a 1.2 μm thick silica upper cladding and 3 μm lower cladding. These ring resonators were simulated using Lumerical FDTD with a mesh accuracy setting of 3, a simulation duration of 20000 fs, and a Courant factor of 0.9, which translates to a time step of 0.05608 fs. The simulated transmission spectra at the through port of all five devices are presented in Fig. 4.6, and their calculated performance measures are given in Table 4.1. Even though 1550 nm was used as a target resonance for all of the devices, the simulated spectra are evidently not aligned, and the smaller gaps result in resonances further away from target. This is because the required ring circumference was calculated based on the effective index within the ring's guiding layer according to the resonance condition $2\pi L n_{\text{eff}}/\lambda = 2\pi m$. However, this refractive index does not

take the loading effects of the bus waveguide into account. As the gap is reduced and the bus is brought closer to the ring cavity, the refractive index experienced by the guided modes in the ring becomes more affected due to stronger mode coupling. Additionally, this interaction results in a phase shift every time the light goes through the coupling points and the resonances in the ring are now more accurately governed by $2\pi L n_{\text{eff}}/\lambda + \phi_{\text{coupler}} = 2\pi m$, where ϕ_{coupler} is the phase that is accrued when passing through the directional coupler portion of the ring cavity [16], [58].

Table 4.1: Performance of simulated AlGaAs-OI microring resonators with different gap sizes around 1550 nm

Gap [nm]	Coupling Regime	FSR [nm]	Q-factor	Extinction Ratio [dB]	Resonance Wavelength [nm]	Finesse
100	Under-coupled	∼11.06	1917.25 ± 0.17	−7.79	1552.07	13.66
200	Near critical coupling	∼10.82	273.31 ± 75.20	−26.55	1554.52	1.90
300	Near critical coupling	∼10.82	343.03 ± 70.22	−27.86	1548.49	2.40
400	Under-coupled	∼11.03	706.24 ± 1.32	−22.29	1549.89	5.03
600	Under-coupled	∼11.04	2979.34 ± 13.58	−10.33	1550.33	21.22

Table 4.2: Results for the small gap size simulated with finer mesh settings

Gap [nm]	Mesh setting	FSR [nm]	Q-factor	Extinction Ratio [dB]	Resonance Wavelength [nm]	Finesse
100	mesh accuracy of 4	∼11.24	1819.53 ± 2.05	−8.69	1550.51	13.19
100	mesh accuracy of 5	∼11.17	1955.88 ± 8.19	−8.80	1552.06	14.08
100	mesh override	∼11.13	2011.21 ± 2.74	−7.4	1549.87	14.44
150	mesh override	∼10.96	568.17 ± 65.55	−20.87	1550.55	4.02

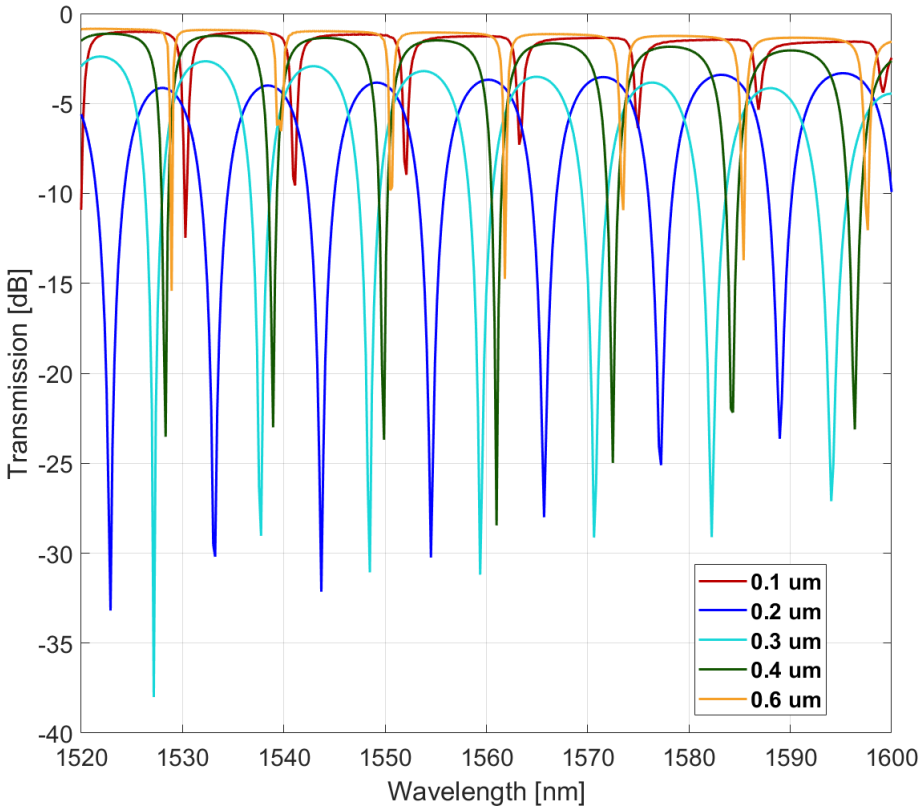


Figure 4.6: The transmission spectrum as observed at the through port of the SWG ring resonators with varying coupling gaps.

The light and dark blue spectra in Fig. 4.6, which correspond to a gap size of 300 nm and 200 nm, portray the deepest resonance dips out of all five devices. For resonances near 1550 nm, their extinction ratios are -27.86 dB and -26.55 dB, respectively. The extinction ratios below -25 dB around 1550 nm indicate the presence of a critically coupled system for both rings. The 400 nm and 600 nm gaps both result in under-coupled systems, but the yellow transmission spectrum exhibits sharper dips due to the light getting trapped in the ring cavity for a longer duration and not being able to escape due to weak coupling. As expected, the device with the largest gap size has the highest Q-factor around 1550 nm. The FSR in the simulated spectra are all above the targeted 10 nm; this discrepancy arises from using the effective medium approximation when calculating the refractive indices used for determining the required ring radius for a target FSR.

For a gap of 100 nm, illustrated in red, the ring resonator exhibits a larger Q-factor and narrower line-width compared to most of the other rings. This behaviour is the opposite of what was initially expected; a smaller gap usually translates to stronger coupling and entering the over-coupled regime, where the

line-width broadens from a short photon lifetime in the resonator. The observed shallow dip and higher Q-factor would imply that the SWG ring resonator is actually in the under-coupled regime. This weak coupling could potentially be attributed to near-field effects that occur when the periodic grating structures are brought closer together such that the proximity is reduced below the grating period. When the gap is reduced to such extents, perhaps the coupling interaction is less "smooth" due to the grating segments actually interacting with other individual unit cells and undergoing interference effects that are not present for the solid-core case. This could make the relation between the gap size and κ less monotonic. Another possible reason is the presence of a very slight mismatch in the alignment of the unit cells at the coupling point, which can potentially reduce the coupling efficiency due to being out of phase. However, the five devices were created in the simulation domain in an identical manner and they only differ in gap size, so such a mismatch should have an effect on all rings.

Another different possibility would be that the simulation requires a much smaller mesh size compared to the other rings. On that note, significantly longer simulations with a finer mesh resolution were performed for a coupling gap of 100 nm and 150 nm to investigate this matter, and the results are shown in Table 4.2. One method used for enhancing the mesh resolution was increasing the mesh accuracy level in the Lumerical FDTD settings, while another method was to use a mesh override region with a maximum step size of 0.0214 μm in all three dimensions. The tabulated results provide further confirmation for the 100 nm coupling gap being truly in the under-coupled regime. Nevertheless, a more comprehensive study should still be conducted to ascertain the exact behaviour of such rings for gaps below their grating pitch before fabrication.

All of the Q-factors reported in this chapter were calculated using the Q-analysis group template provided by Lumerical. This analysis group uses several time-domain monitors placed at different locations within the ring cavity to keep track of all the resonating fields in the structure. A post-processing script then computes the Q-factors by calculating the slope of the time-domain electric field envelope for each resonance as it decays. This tool is especially useful for high-Q ring resonators, as it is neither feasible nor computationally efficient to run FDTD simulations until the optical fields fully decay. Because these high-Q simulations often do not reach the auto-shutoff threshold, the frequency spectrum generated at the simulation output is artificially broadened, since it is the Fourier transform of a prematurely truncated time-domain signal. Even the ring resonator simulations that do successfully terminate via auto-shutoff can suffer from this artificial broadening because the shutoff value is not exactly

zero, meaning some signal truncation still occurs.

Also note that the Q-factors reported in the tables are not the highest calculated Q-factors for each ring; they are simply the value corresponding to the closest resonance around 1550 nm. The smaller resonant wavelengths achieve much higher Q-factors (assuming they still fall safely in the subwavelength regime of the band-structure), because their modes are more confined and thus more weakly coupled, but also because they are at a higher frequency. The Q-factor of a ring resonator actually increases with the operating frequency and is dependent on the choice of resonance, so a less biased performance measure is the finesse, F, which is defined as

$$F = \frac{\nu_F}{\delta\nu} = \nu_F \frac{Q}{\nu}, \tag{4.5}$$

where ν_F is the FSR, ν is the resonance frequency, and $\delta\nu$ is the FWHM linewidth of the transmission spectrum peak. The finesse was calculated using the measured Q-factor and FSR values and is included in both Tables 4.1 and 4.2. As expected, it follows the same trend outlined for the Q-factor since the device comparison is being performed around a single resonance frequency.

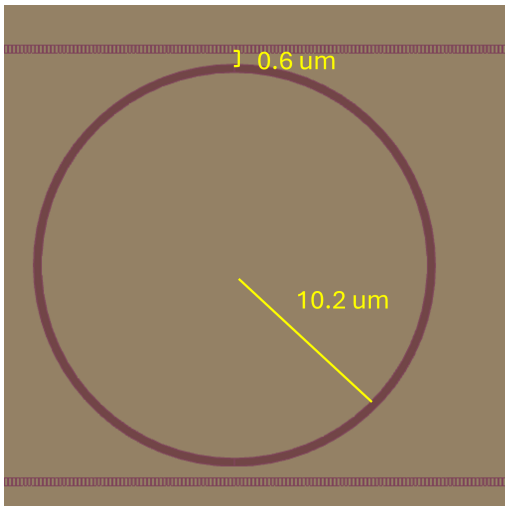
4.2.2 High-Q SWG AlGaAs-OI Ring Resonator

With a high quality factor in mind, a ring resonator with a solid-core AlGaAs-OI ring and SWG bus waveguides was designed and simulated. This was a conscious choice to benefit from the easier evanescent coupling due to the SWG structures in the bus waveguide while reducing the scattering and bend losses that become worse when the ring cavity is segmented. This way the ring can retain a high quality factor owing to the tight mode confinement of AlGaAs-OI while achieving enough coupling at larger gap sizes compared to conventional solid-core AlGaAs-OI devices.

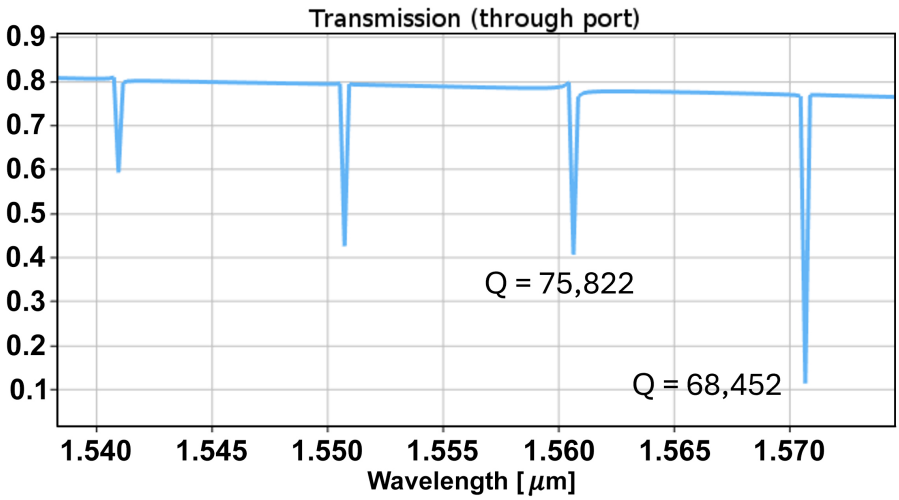
The ring resonator, shown in Fig. 4.7, has a radius of 10.2 μm for a target FSR of 10 nm and resonances centered around 1550 nm. The coupling gap of 600 nm makes the resonator operate in the under-coupled regime. The SWG parameters of the bus are the same as the devices from the previous section. The calculated Q-factor is approximately 75,822 at a resonance wavelength of 1550.69 nm, the FSR is 10 nm, and the corresponding finesse is approximately 488.96, as seen in Fig. 4.7b.

In summary, SWG structures can benefit AlGaAs-OI ring resonators by providing extra degrees of freedom for changing the refractive index of the guiding layers and thus controlling the coupling interactions between the resonator and

input/output waveguides. The use of these periodic gratings in the ring itself poses extra losses that lower the inherent Q-factor of the device, but incorporating these gratings in the directional couplers enables more relaxed gap sizes that are more fabrication friendly. This is why the hybrid design with the solid-core ring and SWG bus waveguide achieves the highest Q-factor and finesse among all of the simulated devices. In general, the under-coupled resonators always had the highest Q-factors while the critically coupled devices exhibited the largest extinction ratios. Another observation from these simulations is the peculiar behaviour for the coupling gap much smaller than the SWG pitch, which showcased an under-coupled system. This behaviour is unexpected because the coupling strength usually increases with a reduction in the gap between the bus and ring. However, this theory is based on conventional solid-core devices, so the encountered deviation might be attributed to near-field effects that can no longer be ignored when the distance between the grating structures of the bus and ring is significantly reduced below the SWG period. The behaviour persisted even as the simulation mesh was refined, but the topic still deserves further investigation. While this chapter was focused on the theoretical design and computational simulation of different AlGaAs-OI SWG ring resonators, the next chapter shifts toward physical nonlinear experiments that investigate FWM in prefabricated SOI Huygens' ring resonators.



(a)



(b)

Figure 4.7: The (a) structure of the high-Q AlGaAs-OI SWG ring resonator and (b) its transmission spectrum observed at the through port.

Chapter 5

Four-Wave Mixing in Silicon-OI Huygens' Microring Resonators

While the AlGaAs-OI SWG microring resonators presented in the previous chapter offer promising simulated performance, physical experimentation is required for validating the potential of subwavelength-engineered structures in nonlinear applications. As previously mentioned, this thesis project was a predominantly simulation-based endeavor due to the nontrivial and slow fabrication process for custom AlGaAs-OI devices. Since the SWG AlGaAs-OI components that have been presented so far have yet to be fabricated, their physical experimentation and verification is currently impossible. However, as part of a broader collaboration between our group and researchers at the National Research Council (NRC) of Canada, we are in possession of a prefabricated SOI photonic chip containing several meta-waveguide devices. These components were designed at the NRC, and the results of their linear characterization have already been published [23].

The devices of interest for this study were the microring resonators. The goal was to achieve four-wave mixing and frequency comb generation in the rings and to see the effect of engineered meta-waveguide structures on these nonlinear processes. It is well known that silicon suffers from high nonlinear absorption losses around 1550 nm such as TPA and FCA [59]. These losses make it difficult to observe nonlinear phenomena such as frequency comb generation in the telecommunication C-band, with many opting for silicon nitride as a low-loss alternative for nonlinear applications. Despite these inherent losses, we believed that a ring resonator created with an alternating pattern of silicon and insulator would exhibit reduced nonlinear losses due to the reduced amount of silicon material in which absorption could occur. Additionally, in the case of a Huygens' ring resonator, the unique photonic band-structure of the device lends itself to a steady negative group index and thus near-zero GVD. This engineered dispersion enables a flat FSR for the device in the central range of

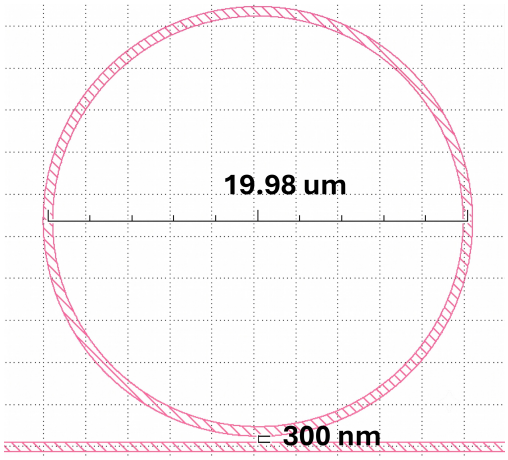
the band diagram and makes it easier to achieve phase-matching conditions for FWM. Near the band-edge and as we approach the photonic band gap the group velocity rapidly changes leading to strong anomalous dispersion [23].

5.1 Devices Under Study

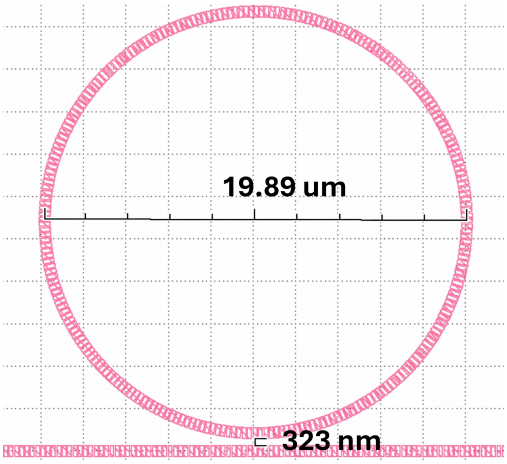
All of the photonic components mentioned in this chapter consist of a silicon core layer with a standard height of 220 nm and an upper and lower cladding of silicon dioxide. The specific devices on the chip that were of interest for this thesis were the SWG, Huygens', and solid-core microring resonators which were each coupled to a single bus waveguide serving as both the input and through ports. Each category included a variety of devices with the same radius of about 10 μm but different gap sizes. Specifically, the Huygens' ring resonator coupling gaps range from 99 – 399 nm, the SWG devices range from 223 – 323 nm and the solid-core rings have gaps in the range of 100 – 300 nm. A sample fabricated device from each category is schematically shown in Fig. 5.1. The Huygens' and SWG structures used for these devices are shown in Fig. 5.2. The Huygens' nano-antenna structures used in these ring resonators are identical to the ones mentioned in a previous study by Bin-Alam *et al.* [23]. However, the coupling gap distances and radii are different for these devices.

The first step before performing nonlinear measurements is to characterize the linear behaviour of the rings. The linear characterization data for all of the ring resonators under study was previously obtained by our postdoctoral researcher at NRC. The resulting transmission spectra from all of the ring resonators is showcased in Fig. 5.3. In order to have efficient FWM within the ring, it is important to choose a pump wavelength that corresponds to a deep resonance close to critical coupling and with a high Q-factor. This ensures that most of the pump power actually enters the ring resonator cavity and is able to get enhanced and lead to the generation of the idler frequency. The next important factor is choosing a signal wavelength that corresponds to an adjacent resonance in the transmission spectrum to benefit from the cavity enhancement while reducing dispersion effects that hinder phase-matching conditions. Lastly, the targeted idler wavelength should also be on resonance to ensure that it can survive and exit from the resonator cavity as an output.

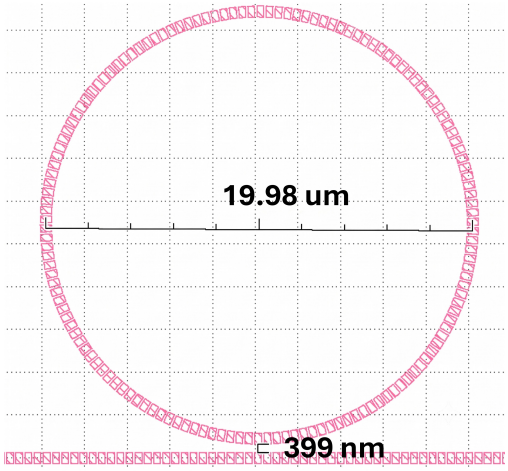
Looking at Fig. 5.3a, it is evident that the solid-core devices with gaps of 200 nm and 300 nm both have deeper resonances and higher extinction ratios. The orange spectrum has an extinction ratio of ∼1.658 dB at 1560.25 nm and the yellow spectrum undergoes an extinction ratio of ∼1.545 dB at 1587.4 nm. Either



(a) Solid-core microring resonator

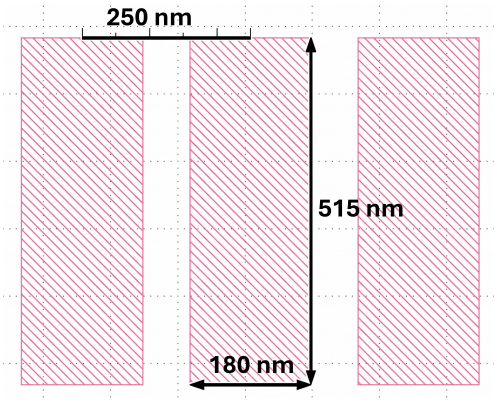


(b) SWG microring resonator

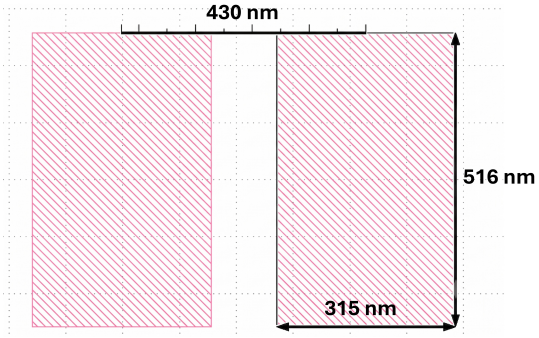


(c) Huygens' microring resonator

Figure 5.1: Example layout files for the fabricated ring resonators under study.



(a) SWG structure



(b) Huygens' nano-antenna structures

Figure 5.2: The geometry of the Huygens' and SWG structures used in the ring resonators under study.

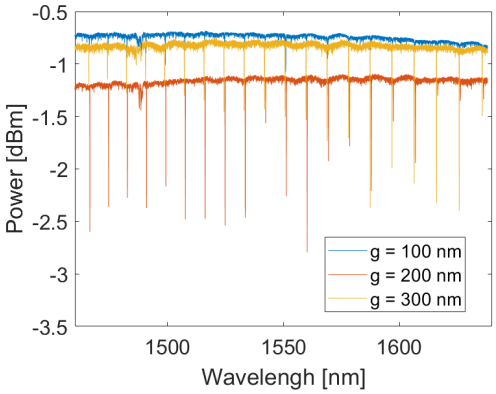
device could be an ideal candidate for FWM depending on the chosen operating wavelengths. For the SWG ring resonators, shown in Fig. 5.3b, the best candidate for FWM would be the device with a gap of 323 nm, which demonstrates the deepest resonances compared to the rest. For this device the pump and signal wavelengths should be adjacent values chosen from the resonances between 1460 – 1511 nm. Lastly, Fig. 5.3a shows the transmission spectra for Huygens' ring resonators with seven different coupling gaps. The output power for these rings falls drastically after 1560 nm due to approaching the photonic bandgap of the structure. For the Huygens case the choice of which device is most suitable for the FWM experiments depends on being able to find three adjacent resonance peaks that are all deep enough, are equidistant from each other (flat FSR), and correspond to wavelengths that are accessible by our bench-top lasers in the lab.

Due to the reasons outlined above in addition to the laboratory constraints mentioned in the next section, only two ring resonators were chosen among the ones showcased here for FWM measurements. The chosen devices are the solid-core ring with a 200 nm gap and the Huygens' ring with a 399 nm gap. Their linear transmission and FSR is shown in Fig. 5.4. None of the SWG rings were chosen because their good resonances lie outside of the EDFA (Erbium-Doped Fiber Amplifier) wavelength range that we use as a pump laser.

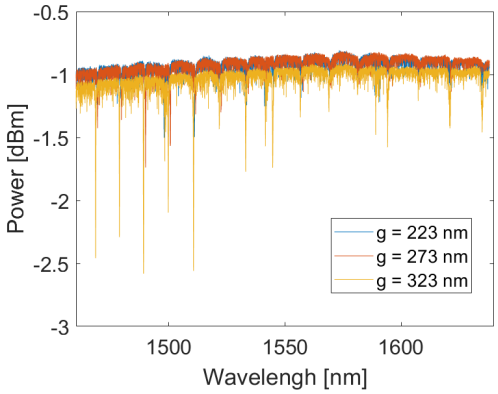
5.2 Experimental Setup and Results

The main goal of this chapter is to verify our assumption regarding the possibility of frequency comb generation in SOI ring resonators that have been dispersion-engineered with Huygens' meta-waveguide structures. Or at least, to witness an increase in the efficiency of the FWM process compared to the solid conventional silicon ring. This was investigated by performing stimulated FWM in both devices and comparing their results.

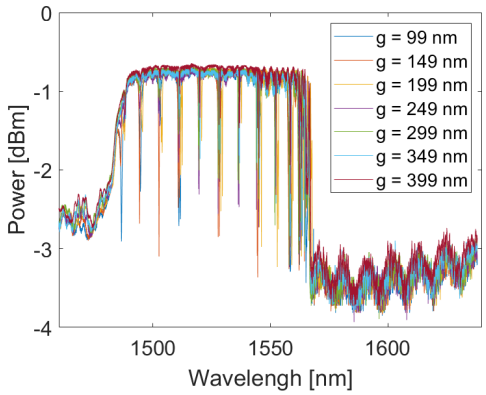
A simplified schematic of the experimental setup is given in Fig. 5.5. Both the signal and pump beams are continuous-wave (CW) lasers. The pump source is the Santec TSL-710 CW laser that is fed into an EDFA with an optimal amplification range of 1540 – 1565 nm. For my signal beam I use the Optilab TLS-C-B, a bench-top laser with 96 discrete channels from 1530 nm to 1560 nm with a wavelength spacing of 0.4 nm. The signal beam also goes through an EDFA. The discreteness of channels for the signal and the accessible amplification range both limit the resonance wavelengths that I can target in each device, and are the main constraint that has resulted in only two of the devices on the chip being measured and presented herein.



(a) Solid-core microring resonators



(b) SWG microring resonators

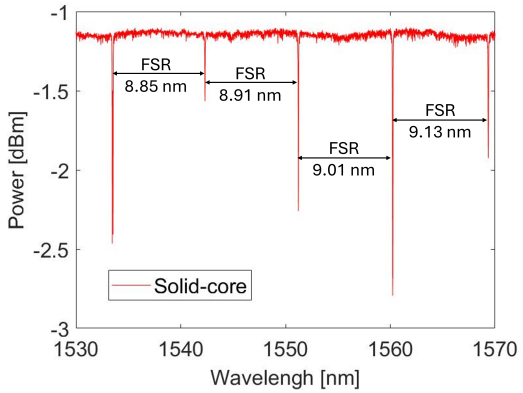


(c) Huygens' microring resonators

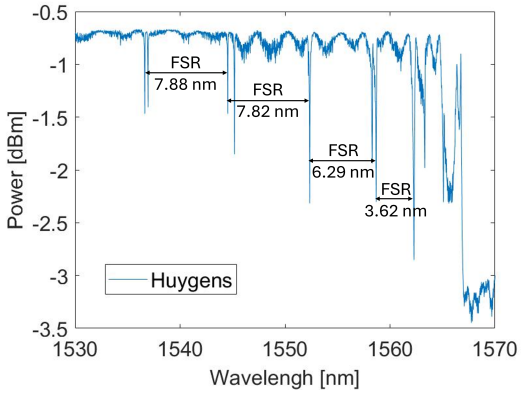
Figure 5.3: Transmission Spectra at the through port of ring resonators with different coupling gap sizes.

The pump and signal beams are combined in an optical fiber coupler junction before being sent into free-space propagation. Most of the transmission is done in free space to simplify the setup. Additionally, good lossless fiber optic cables were limited in the lab. The optical path includes a HWP and linear polarizer used for added power control. Right before entering the coupling stage of the photonic chip, the input beam goes through a 50:50 beam splitter and the resultant reference beam is used for monitoring the input power through a photodetector. Before conducting the nonlinear experiment the chip has to be properly aligned so that I am fully coupled into the device that I wish to study. I use a Luminos PIC alignment stage for controlling the three axes and microscope objectives are placed at the input and output of the chip for optimal light coupling. The output of the stage is monitored via a photodetector while alignment is in progress. After the desired device has been excited, the combined pump and signal beams are sent through the bus waveguide, and the resulting output is measured with an optical spectrum analyzer (OSA).

For the solid-core silicon ring resonator measurements, the signal wavelength



(a) Solid-core microring resonator with a gap of 200 nm.



(b) Huygens' microring resonator with a gap of 399 nm.

Figure 5.4: Transmission Spectra of the two devices used for FWM measurements.

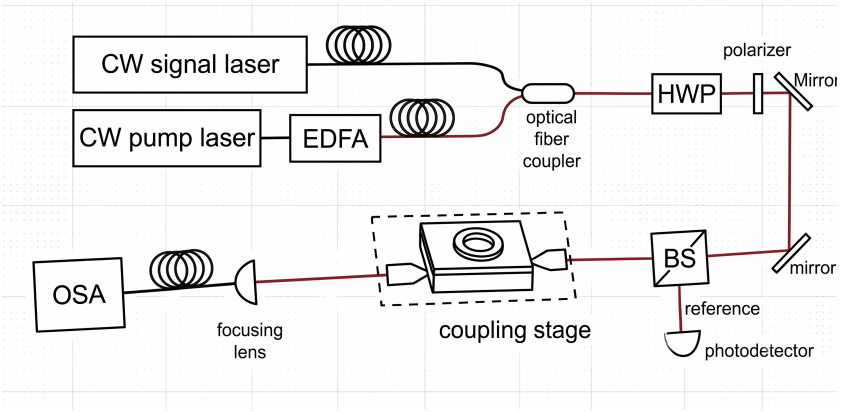


Figure 5.5: A simplified illustration of the experimental setup used for the FWM measurements.

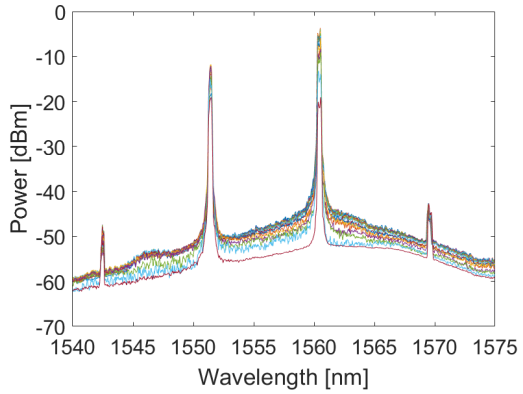
was kept constant at 1551.445 nm, while the pump laser was tuned from 1560.4 – 1560.51 nm. The power of the signal and pump, as measured through the identical reference beam, were kept constant at 1 mW and 3.8 mW, respectively. As seen in Fig. 5.6a, the maximum idler power of -47.39 dBm appears around 1542.52 nm when the pump beam has a wavelength of 1560.444 nm. A second idler is also generated at 1569.575 nm. Both idler peaks disappear at pump wavelengths of 1560.5 nm and above.

For the Huygens' ring resonator FWM measurements, the signal wavelength was always 1554.975 nm, while the pump laser was varied from 1543.9 – 1546.9 nm. The signal and pump powers were 1 mW and 15 mW, respectively. Fig. 5.6b shows the FWM results when the pump is varied from 1543.9 – 1544.148 nm. This subset of measurements includes the optimal results, shown separately in Fig. 5.6c, that were obtained for this device at a pump wavelength of 1544.148

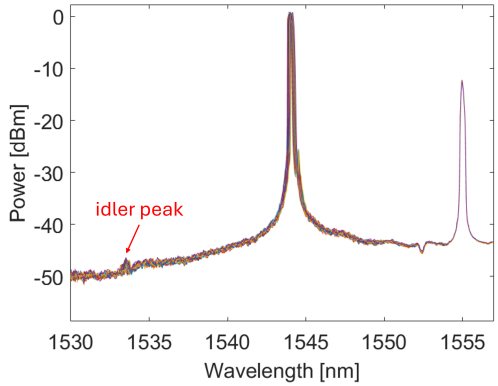
nm and with a −46.36 dBm idler generated at 1533.51 nm. There is only one idler because the other symmetric resonance falls in the photonic bandgap of the device, so the wavelength does not survive as a guided mode in the Huygens' structure. It should be noted that even though the wavelength sweep for the pump laser was set for 1543.9 – 1546.9 nm, the laser itself mode-hopped when it reached certain wavelengths and this led to not having data for ranges such as 1544.148 – 1544.553 and 1545.6 – 1546.2 nm. This mode-hopping phenomenon was, unfortunately, not a one-time occurrence and happened even when we tried to manually set the wavelength range. It is thus possible that another pump wavelength could be the true optimal point for the Huygens' ring, with a slightly higher generated idler power.

The data presented in this chapter is the result of many measurements that were conducted in order to successfully witness the FWM process in both devices. The initial target values for the pump and signal wavelengths were always chosen based on the transmission spectrum data seen in Fig. 5.4, however setting these values for the input beams never generated an idler. This is because the optical power in the ring was intense enough to cause thermal shifting in the resonance peaks. This red-shifts the resonances so the actual pump and signal wavelengths that resulted in successful FWM differ from the resonance peaks of the linear transmission spectra. This shifting becomes even worse when we are near a resonance because more power is confined within the ring. Thus, to find the correct resonance targets for the input beams in order to generate an idler, the signal and pump laser sources were tuned from a wavelength below the target resonance and very slowly increased until an idler was observed. The power levels were also changed to find the minimum pump power that results in a clear generated idler at the output. After the initial manual tuning, the pump laser was then varied through a computer-controlled wavelength sweep, and the OSA readings were recorded.

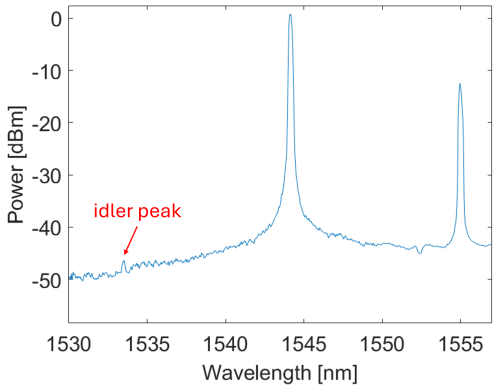
The efficiency of the FWM process is determined by the ratio of the incident pump power to the generated idler power. If we take the pump power recorded before the PIC coupling stage as the incident power, then the maximum FWM efficiency becomes 0.00048% for the solid-core ring and 0.00015% for the Huygens' ring for their respective optimal scenarios. We can already tell by looking at Fig. 5.6 that the solid-core silicon ring resonator has a better nonlinear performance compared to the Huygens' silicon ring. Even though the pump power before the coupling stage is almost four times higher in the Huygens' experiments, the generated idler is still stronger and more clear in the solid-core device. Since both rings are made of silicon, the TPA and FCA losses affect both



(a) Solid-core microring resonator with a signal wavelength set to 1551.445 nm and the pump laser varied from 1560.4 – 1560.51 nm.



(b) Huygens' microring resonator with a signal wavelength set to 1554.975 nm and the pump laser varied from 1543.9 – 1544.148 nm.



(c) The optimal result for the Huygens' ring at a pump wavelength of 1544.148 nm with a generated idler appearing at 1533.51 nm.

Figure 5.6: FWM measurement results.

of them, with the solid-core ring theoretically being affected more due to having more silicon for the light to propagate through. However, the radiative and scattering bend losses in the ring are worse for the Huygens' structure which can affect the efficiency of nonlinear phenomena. Another possible detrimental factor for the Huygens' device is the fact that we are operating a bit close to the band edge where the FSR is no longer flat, and we enter the regime of anomalous dispersion. This can impact the phase-matching between the three beams and thus reduce the FWM efficiency.

Furthermore, the proportion of incident pump power that actually reaches each ring is not the same. The Huygens' meta-waveguide that forms the bus waveguide has higher losses compared to the solid-core bus. The linear loss coefficients for both straight waveguides has been previously measured in the group for other devices on the chip over a range of wavelengths. At its optimal pump wavelength the linear loss coefficient for the solid strip silicon ring resonator's

bus waveguide is 1.2 dB/cm. On the other hand, the Huygens' meta-waveguide has a loss coefficient of about 4 dB/cm for the operating range of wavelengths. Additionally, all of the devices on this PIC use the same edge coupler design at the input and output of the devices. This edge coupler is designed for the solid strip silicon waveguides, so when used for the Huygens' meta-waveguide it includes both a 4.24 mm long strip of solid-core silicon followed by a mode-converter before entering the actual Huygens' section. This is schematically illustrated in Fig. 5.7. The measured efficiencies for the edge coupler and mode-converter are about 27% and 40% around 1550 nm, which are both quite low. The low efficiency of the edge coupler affects both devices the same way, but only the Huygens' ring has the mode converters, thus it has an extra loss both at the input and at the output of the bus waveguide which can affect the measured FWM efficiency.

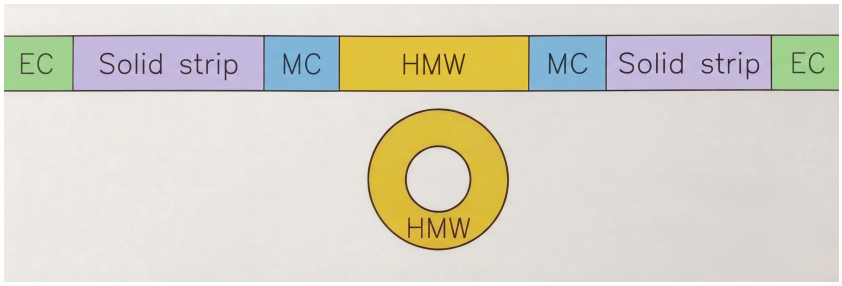


Figure 5.7: Both edges of the chip have edge couplers (EC) that couple into or out of a solid silicon waveguide section. The solid-core waveguides are connected to the Huygens' meta-waveguide (HMW) through mode-converters (MC).

To conduct a more fair assessment of the performance of the two rings, we should consider the power that truly reaches the input of the ring for calculating the efficiencies. In that case, the approximate pump power reaching the Huygens' ring resonator is actually $(0.27)\times(0.4)\times(15\text{ mW}) = 1.62$ mW, and the idler power leaving the device right before the output mode converter is approximately $(0.27)^{-1} \times (0.4)^{-1}\times(23.121\text{ nW}) = 214.1$ nW. This gives a FWM efficiency of $\sim$0.013% for the Huygens' ring resonator. Similarly, the pump power reaching the solid-core SOI ring is approximately $(0.27)\times(3.8\text{ mW}) = 1.026$ mW and the generated idler is $(0.27)^{-1}\times(23.121\text{ nW}) = 85.63$ nW, resulting in a FWM efficiency of $\sim$0.0083%. This means FWM in the Huygens' meta-waveguide microring resonator is almost twice as efficient compared to the solid-core SOI ring. By considering the input/output coupling loss factors, one can see that the Huygens' ring structure is actually not inherently more lossy. To perform a more proper comparison, the devices should be redesigned and fabricated such that they both achieve similar coupling efficiencies at their input and output.

In summary, while the SOI Huygens' ring resonator was not able to generate a frequency comb, stimulated four-wave mixing (FWM) was successfully observed leading to the generation of an idler at 1533.51 nm. At first glance the strength of the generated idlers seems to favor the solid-core device, but when the insertion and mode-conversion losses are accounted for, the Huygens' ring resonator achieves an internal FWM efficiency ($\sim$0.013%) that outperforms the conventional solid-core SOI ring ($\sim$0.0083%). As previously discussed in Chapter 1, the AlGaAs-OI platform has already shown success in the literature for efficient frequency comb generation. Therefore, it is reasonable to believe that a Huygens' microring resonator designed and fabricated with AlGaAs-OI instead of SOI could have more promising results by avoiding the inherent TPA and FCA losses present in silicon. To my knowledge, this is the first instance of FWM being reported in Huygens' microring resonators. These experimental findings, combined with the theoretical designs and simulation results from the preceding chapters, provide a strong justification for the continued exploration of subwavelength-engineered photonic components based on the AlGaAs-OI platform.

Chapter 6

Conclusions and Future Work

With the ever-increasing demand for higher bandwidths and greater data speeds in communication systems, the appeal of transitioning signal processing to the optical domain increases. Such an endeavor requires a material platform with high optical nonlinearity and low losses in the telecommunication band, and it would also benefit from a database of ready-to-use component designs that can be used for forming the required optical circuits for different signal processing applications. To this end, the primary objective of this master's project was to explore the design and simulation of fundamental photonic components that combine the high-contrast AlGaAs-OI platform with subwavelength grating structures for potential applications in the telecommunication C-band.

The combination of efficient light emitting properties, high second- and third-order nonlinearities, and negligible two-photon absorption in the C-band already make AlGaAs a great candidate for monolithic integrated circuits that are specifically designed for signal manipulation applications. Furthermore, applying the same subwavelength engineering techniques that have garnered great success in silicon photonics to III-V compounds can further facilitate monolithic integration by adding extra degrees of freedom to the design and enabling dispersion engineering without the need to change the chemical composition of the material or the height of the structure.

The main contributions of this thesis are structured progressively from the most fundamental and basic component, waveguides, to the more complex devices such as microring resonators. First, AlGaAs-OI subwavelength grating waveguides were designed and simulated for different heights (200 nm and 500 nm) and upper cladding materials (silica or air) based on what can be later fabricated in our group. The waveguide optimization was done through SWG unit-cell band-structure calculations, and full 3D FDTD simulations confirmed the propagation of Floquet-Bloch modes in the subwavelength regime with minimal-to-no back-scattering. These AlGaAs-OI SWG waveguides can be used as a starting point for designing other photonic components, or for use in optical

routing on a photonic integrated chip.

To overcome the coupling bottleneck between optical fibers and sub-micron integrated waveguides, a compact fiber-to-chip AlGaAs-OI SWG edge coupler was designed. By linearly chirping the grating pitch and duty cycle while varying the width, adiabatic mode expansion matching a fiber with an MFD of 3.2 μm was achieved over a total length of only 30 μm. The simulated coupler demonstrated a low coupling loss of -0.45 dB for the fiber's fundamental quasi-TE mode and -0.56 dB for the quasi-TM mode at 1550 nm, maintaining high transmission ($> 85\%$) over a 200 nm bandwidth for TE polarization.

For AlGaAs-OI SWG microring resonators, I analyzed fully SWG resonators in various coupling regimes by varying the gap size between the ring and bus waveguides. Designs and simulation results were provided for both critically coupled and under-coupled rings, which can be potentially used for filtering and sensing applications, respectively. While fully SWG rings exhibited higher radiation and scattering losses in their waveguide bends, a hybrid design featuring an SWG bus waveguide paired with a solid-core AlGaAs-OI ring leveraged the modal delocalization inherent to SWG structures to relax coupling gaps, while reducing the scattering and bend losses in the ring. An under-coupled hybrid SWG ring resonator with a 10.2 μm radius and a 600 nm gap achieved a quality factor of $Q \approx 75,822$ at 1550.69 nm with a 10 nm FSR.

Finally, in collaboration with the National Research Council (NRC) of Canada, nonlinear experiments were conducted on fabricated silicon-on-insulator (SOI) microring resonators incorporating Huygens' meta-waveguides with the goal of observing frequency comb generation. Stimulated four-wave mixing (FWM) was successfully observed in a Huygens' ring, yielding a generated idler at 1533.51 nm with an internal conversion efficiency of $\sim 0.013\%$; however, frequency comb generation was not observed. To my knowledge, this represents the first reported experimental demonstration of FWM in Huygens' meta-waveguide microring resonators.

Building upon the findings of this thesis, several avenues for future research are identified. First, fabrication of the proposed AlGaAs-OI SWG waveguides, edge coupler, and microring resonators should be carried out to validate the numerical simulation models against physical laboratory measurements. Future work can also build upon the reported designs and methodology to create components with optimal nonlinear performance for specific all-optical signal processing applications, which is most relevant for the ring resonator designs. Furthermore, frequency comb generation should be explored in AlGaAs-OI Huygens' ring resonators. While TPA and FCA losses in silicon inhibited frequency

comb generation in the tested SOI Huygens' ring, AlGaAs-OI possesses a larger bandgap (1.65 eV) with negligible TPA at 1550 nm. Designing and fabricating Huygens' microring resonators on AlGaAs-OI offers a promising pathway toward low-threshold frequency comb generation. Lastly, the experimental setup for the SOI Huygens' ring could be improved. Future nonlinear experiments with the SOI devices would benefit from continuously tunable pump lasers with fine wavelength resolution to reduce thermal resonance shifts. The SOI photonic chip could also benefit from a re-design, where the Huygens' meta-waveguide devices are given their very own custom high-efficiency edge couplers and mode converters to minimize input/output insertion losses.

In conclusion, this work demonstrates the potential of combining subwavelength grating structures with III-V semiconductor platforms like AlGaAs-OI to provide a versatile toolkit for index contrast, dispersion engineering, and compactness in integrated photonics, paving the way for monolithic circuits for all-optical signal processing and other telecommunication applications. This thesis serves as groundwork for further exploration and development of subwavelength-engineered devices for the AlGaAs-OI platform.

Bibliography

[1] R. Paschotta, *Optical fiber communications*, RP Photonics Encyclopedia, 2005. DOI: 10.61835/9ec [Online]. Available: https://www.rp-photonics.com/optical_fiber_communications.html

[2] J. Yu, *The Problem with Bandwidth in Optical Transport*, en-US, Sep. 2023. [Online]. Available: https://www.delloro.com/the-problem-with-bandwidth-in-optical-transport/

[3] P. Minzioni et al., "Roadmap on all-optical processing," *J. Opt.*, vol. 21, p. 063 001, May 2019, Publisher: IOP Publishing, ISSN: 2040-8986. DOI: 10.1088/2040-8986/ab0e66

[4] V. R. Almeida, C. A. Barrios, R. R. Panepucci, and M. Lipson, "All-optical control of light on a silicon chip," *Nature*, vol. 431, no. 7012, pp. 1081–1084, Oct. 2004.

[5] S. F. Preble, Q. Xu, B. S. Schmidt, and M. Lipson, "Ultrafast all-optical modulation on a silicon chip," *Opt. Lett.*, vol. 30, no. 21, pp. 2891–2893, Nov. 2005. DOI: 10.1364/OL.30.002891

[6] S. Saeidi, K. M. Awan, L. Sirbu, and K. Dolgaleva, "Nonlinear photonics on-a-chip in III-V semiconductors: Quest for promising material candidates," *Appl. Opt.*, vol. 56, no. 19, pp. 5532–5541, Jul. 2017. DOI: 10.1364/AO.56.005532

[7] E. Mobini, D. H. G. Espinosa, K. Vyas, and K. Dolgaleva, "AlGaAs nonlinear integrated photonics," *Micromachines*, vol. 13, no. 7, 2022, ISSN: 2072-666X. DOI: 10.3390/mi13070991

[8] L. Chang et al., "Ultra-efficient frequency comb generation in AlGaAs-on-insulator microresonators," in *Conference on Lasers and Electro-Optics*, Optica Publishing Group, 2020. DOI: 10.1364/CLEO_SI.2020.STu3H.8

[9] P. Cheben et al., "Recent advances in metamaterial integrated photonics," en, *Adv. Opt. Photon.*, vol. 15, no. 4, p. 1033, Dec. 2023, ISSN: 1943-8206. DOI: 10.1364/AOP.495828

[10] R. W. Boyd, *Nonlinear Optics*. London Academic Press, an imprint of Elsevier, 2020.

[11] K. Dolgaleva, *Introduction to Optics I: Interaction of Light with Matter*. Springer International Publishing, 2021.

[12] T. Fortier and E. Baumann, "20 years of developments in optical frequency comb technology and applications," *Communications Physics*, vol. 2, no. 1, p. 153, Dec. 2019.

[13] L. Chang et al., "Second order nonlinear photonic integrated platforms for optical signal processing," *IEEE Journal of Selected Topics in Quantum Electronics*, vol. 27, no. 2, pp. 1–11, 2021. DOI: 10.1109/JSTQE.2020.3025219

[14] B. E. A. Saleh and M. C. Teich, *Fundamentals Of Photonics*. Wiley, 2019.

[15] R. Paschotta, *Effective mode area*, RP Photonics Encyclopedia. DOI: 10.61835/7c2 [Online]. Available: https://www.rp-photonics.com/effective_mode_area.html

[16] L. Chrostowski and M. E. Hochberg, *Silicon photonics design*, en. Cambridge: Cambridge university press, 2015, ISBN: 978-1-107-08545-9.

[17] J. Yang, M. Tang, S. Chen, and H. Liu, "From past to future: On-chip laser sources for photonic integrated circuits," en, *Light Sci Appl*, vol. 12, no. 1, p. 16, Jan. 2023, Publisher: Nature Publishing Group, ISSN: 2047-7538. DOI: 10.1038/s41377-022-01006-0

[18] C. Wang, M. Zhang, M. Yu, R. Zhu, H. Hu, and M. Loncar, "Monolithic lithium niobate photonic circuits for Kerr frequency comb generation and modulation," *Nature Communications*, vol. 10, no. 1, p. 978, Feb. 2019, ISSN: 2041-1723. DOI: 10.1038/s41467-019-08969-6 [Online]. Available: https://doi.org/10.1038/s41467-019-08969-6

[19] C. J. Krückel, A. Fülöp, Z. Ye, P. A. Andrekson, and V. Torres-Company, "Optical bandgap engineering in nonlinear silicon nitride waveguides," *Opt. Express*, vol. 25, no. 13, pp. 15 370–15 380, Jun. 2017. DOI: 10.1364/OE.25.015370 [Online]. Available: https://opg.optica.org/oe/abstract.cfm?URI=oe-25-13-15370

[20] G. STEGEMAN et al., "Algaas below half bandgap: The silicon of nonlinear optical materials," *Journal of Nonlinear Optical Physics & Materials*, vol. 03, no. 03, pp. 347–371, 1994. DOI: 10.1142/S0218199194000213

[21] P. S. J. Russell, "Optics of Floquet-Bloch waves in dielectric gratings," en, *Appl. Phys. B*, vol. 39, no. 4, pp. 231–246, Apr. 1986, ISSN: 1432-0649. DOI: 10.1007/BF00697490

[22] G. Parker, "Guided-wave optical communications: Materials," in *Encyclopedia of Materials: Science and Technology*, K. J. Buschow and other, Eds., Oxford: Elsevier, 2001, pp. 3703–3707, ISBN: 978-0-08-043152-9. DOI: https://doi.org/10.1016/B0-08-043152-6/00660-4

[23] M. S. Bin-Alam et al., "Directional and Contra-Directional Coupling in Huygens' Metawaveguide Microring Resonators," en, *ACS Photonics*, vol. 13, no. 9, pp. 2408–2419, May 2026, ISSN: 2330-4022, 2330-4022. DOI: 10.1021/acsphotonics.5c02868 [Online]. Available: https://pubs.acs.org/doi/10.1021/acsphotonics.5c02868

[24] P. Cheben, D.-X. Xu, S. Janz, and A. Densmore, "Subwavelength waveguide grating for mode conversion and light coupling in integrated optics," *Opt. Express*, vol. 14, no. 11, pp. 4695–4702, May 2006. DOI: 10.1364/OE.14.004695

[25] J. Luque-González et al., "A review of silicon subwavelength gratings: Building break-through devices with anisotropic metamaterials," *Nanophotonics*, vol. 10, no. 11, pp. 2765–2797, 2021. DOI: doi:10.1515/nanoph-2021-0110

[26] P. Cheben et al., "Refractive index engineering with subwavelength gratings for efficient microphotonic couplers and planar waveguide multiplexers," *Opt. Lett.*, vol. 35, no. 15, pp. 2526–2528, Aug. 2010. DOI: 10.1364/OL.35.002526

[27] T. Barwicz et al., "Integrated Metamaterial Interfaces for Self-Aligned Fiber-to-Chip Coupling in Volume Manufacturing," *IEEE Journal of Selected Topics in Quantum Electronics*, vol. 25, no. 3, pp. 1–13, May 2019, Conference Name: IEEE Journal of Selected Topics in Quantum Electronics, ISSN: 1558-4542. DOI: 10.1109/JSTQE.2018.2879018 Accessed: Nov. 4, 2024.

[28] J. Wang, I. Glesk, and L. R. Chen, "Subwavelength grating filtering devices," *Opt. Express*, vol. 22, no. 13, pp. 15 335–15 345, Jun. 2014. DOI: 10.1364/OE.22.015335

[29] Z. Wang et al., "High quality factor subwavelength grating waveguide micro-ring resonator based on trapezoidal silicon pillars," *Opt. Lett.*, vol. 41, no. 14, pp. 3375–3378, Jul. 2016. DOI: 10.1364/OL.41.003375

[30] W. Xie et al., "Ultrahigh-Q AlGaAs-on-insulator microresonators for integrated nonlinear photonics," *Opt. Express*, vol. 28, no. 22, pp. 32 894–32 906, Oct. 2020. DOI: 10.1364/OE.405343

[31] A. Ortega-Moñux et al., "An ultra-compact multimode interference coupler with a subwavelength grating slot," *Laser & Photonics Reviews*, vol. 7, no. 2, pp. L12–L15, 2013. DOI: https://doi.org/10.1002/lpor.201200106

[32] R. Halir et al., "Ultra-broadband nanophotonic beamsplitter using an anisotropic sub-wavelength metamaterial," *Laser & Photonics Reviews*, vol. 10, no. 6, pp. 1039–1046, 2016. DOI: https://doi.org/10.1002/lpor.201600213

[33] G. P. Agrawal, *Fiber-optic communication systems* (Wiley series in microwave and optical engineering), en, Fifth. Hoboken, NJ: Wiley, 2021, ISBN: 978-1-119-73737-7 978-1-119-73739-1. DOI: 10.1002/9781119737391

[34] J. Nijem et al., "High-q and high finesse silicon microring resonator," *Opt. Express*, vol. 32, no. 5, pp. 7896–7906, Feb. 2024. DOI: 10.1364/OE.514080

[35] H. Hu et al., "Single-source chip-based frequency comb enabling extreme parallel data transmission," en, *Nature Photon*, vol. 12, no. 8, pp. 469–473, Aug. 2018, ISSN: 1749-4893. DOI: 10.1038/s41566-018-0205-5

[36] X. Lu et al., "1 Milliwatt Pumped Error-Free 38 GBaud Wavelength Conversion with AlGaAs Microresonators of 1 GHz Intrinsic Linewidth," in *2023 Asia Communications and Photonics Conference/2023 International Photonics and Optoelectronics Meetings (ACP/POEM)*, Nov. 2023, pp. 1–4. DOI: 10.1109/ACP/POEM59049.2023.10369703 [Online]. Available: https://ieeexplore.ieee.org/document/10369703/?arnumber=10369703

[37] L. Oxenløwe et al., "Optical processing and manipulation of wavelength division multiplexed signals," en, in *Optical Fiber Telecommunications VII*, Elsevier, 2020, ch. 6, pp. 233–299, ISBN: 978-0-12-816502-7. DOI: 10.1016/B978-0-12-816502-7.00007-5

[38] Z. Yan et al., "An Optical Parametric Amplifier via \chi $^{(2)}$ in AlGaAs Waveguides," *Journal of Lightwave Technology*, vol. 40, no. 17, pp. 5943–5951, Sep. 2022, ISSN: 1558-2213. DOI: 10.1109/JLT.2022.3186551 [Online]. Available: https://ieeexplore.ieee.org/document/9807420/

[39] H. Liu et al., "A comprehensive survey on optical modulation techniques for advanced photonics applications," en, *Optics and Lasers in Engineering*, vol. 186, p. 108 773, Mar. 2025, ISSN: 01438166. DOI: 10.1016/j.optlaseng.2024.108773

[40] P. J. Delfyett et al., "InP-Based Device Technologies for Signal Processing Using Ultrafast Frequency Combs," *IEEE Journal of Selected Topics in Quantum Electronics*, vol. 24, no. 1, pp. 1–13, Jan. 2018, ISSN: 1558-4542. DOI: 10.1109/JSTQE.2017.2720973 [Online]. Available: https://ieeexplore.ieee.org/document/7961174/

[41] A. Ostrovskis et al., "Heterogeneously Integrated InP Electro-Absorption Modulator for Beyond 300 Gb/s Optical Links," *Journal of Lightwave Technology*, vol. 43, no. 4, pp. 1826–1836, 2025. DOI: 10.1109/JLT.2025.3526822

[42] K. Hakiri, M. Suzuki, and S. Kakio, "Acousto-optic modulators driven by longitudinal leaky surface acoustic waves on linbo3 thin-plate bonded structures," *Japanese Journal of Applied Physics*, vol. 58, no. SG, SGGA09, Jul. 2019. DOI: 10.7567/1347-4065/ab0ba1 [Online]. Available: https://dx.doi.org/10.7567/1347-4065/ab0ba1

[43] G. Dushaq et al., "Electro-optic tuning in composite silicon photonics based on ferroionic 2D materials," en, *Light Sci Appl*, vol. 13, no. 1, p. 92, Apr. 2024, Publisher: Nature Publishing Group, ISSN: 2047-7538. DOI: 10.1038/s41377-024-01432-2 [Online]. Available: https://www.nature.com/articles/s41377-024-01432-2

[44] Y. Yu et al., "All-optical signal processing using InP photonic-crystal nanocavity switches," en, in *2014 16th International Conference on Transparent Optical Networks (ICTON)*, Graz: IEEE, Jul. 2014, pp. 1–4, ISBN: 978-1-4799-5601-2. DOI: 10.1109/ICTON.2014.6876691 [Online]. Available: http://ieeexplore.ieee.org/document/6876691/

[45] S. Mikroulis et al., "40-gb/s NRZ and RZ operation of an all-optical AND logic gate based on a passive InGaAsP/InP microring resonator," en, *J. Lightwave Technol.*, vol. 24, no. 3, pp. 1159–1164, Mar. 2006, ISSN: 0733-8724. DOI: 10.1109/JLT.2005.863320 [Online]. Available: http://ieeexplore.ieee.org/document/1605317/

[46] J. Yu, "Why So Many Coherent DSPs?" en, *Lightwave*, Jul. 2023. [Online]. Available: https://supplements.endeavorb2b.com/endeavorevents/2307lw_showissue/MobilePagedArticle.action?articleId=1892482

[47] S. Mikroulis et al., "Ultrafast all-optical AND logic operation based on four-wave mixing in a passive InGaAsP-InP microring resonator," en, *IEEE Photon. Technol. Lett.*, vol. 17, no. 9, pp. 1878–1880, Sep. 2005, ISSN: 1041-1135. DOI: 10.1109/LPT.2005.853260 [Online]. Available: http://ieeexplore.ieee.org/document/1498889/

[48] K. Singh and G. Kaur, "Interferometric architectures based All-Optical logic design methods and their implementations," en, *Optics & Laser Technology*, vol. 69, pp. 122–132, Jun. 2015, ISSN: 00303992. DOI: 10.1016/j.optlastec.2014.12.027 [Online]. Available: https://linkinghub.elsevier.com/retrieve/pii/S0030399214003363

[49] F. Kizhakkakath et al., "Realization and optimization of optical logic gates using bias assisted carrier-injected triple parallel microring resonators," en, *Results in Optics*, vol. 4, p. 100 090, Aug. 2021, ISSN: 26669501. DOI: 10.1016/j.rio.2021.100090 [Online]. Available: https://linkinghub.elsevier.com/retrieve/pii/S2666950121000389

[50] *III-V Semiconductor Optical Material Data Tool*. [Online]. Available: https://optics.ansys.com/hc/en-us/articles/4411081333011-III-V-Semiconductor-Optical-Material-Data-Tool

[51] S. Adachi, "GaAs, AlAs, and AlxGa1−xAs: Material parameters for use in research and device applications," *J. Appl. Phys.*, vol. 58, no. 3, R1–R29, Aug. 1985, ISSN: 0021-8979. DOI: 10.1063/1.336070

[52] M. Guden and J. Piprek, "Material parameters of quaternary iii - v semiconductors for multilayer mirrors at wavelength," *Modelling and Simulation in Materials Science and Engineering*, vol. 4, no. 4, p. 349, Jul. 1996. DOI: 10.1088/0965-0393/4/4/002

[53] S. Gehrsitz, F. K. Reinhart, C. Gourgon, N. Herres, A. Vonlanthen, and H. Sigg, "The refractive index of AlxGa1−xAs below the band gap: Accurate determination and empirical modeling," *Journal of Applied Physics*, vol. 87, no. 11, pp. 7825–7837, Jun. 2000, ISSN: 0021-8979. DOI: 10.1063/1.373462 [Online]. Available: https://doi.org/10.1063/1.373462

[54] *Convergence testing process for FDTD simulations*. [Online]. Available: https://optics.ansys.com/hc/en-us/articles/360034915833-Convergence-testing-process-for-FDTD-simulations

[55] S. M. Rytov, "Electromagnetic properties of a finely stratified medium," *Soviet Physics JETP*, vol. 2, no. 3, pp. 466–475, 1956.

[56] J. D. Sarmiento-Merenguel et al., "Controlling leakage losses in subwavelength grating silicon metamaterial waveguides," *Opt. Lett.*, vol. 41, no. 15, pp. 3443–3446, Aug. 2016. DOI: 10.1364/OL.41.003443

[57] P. Cheben et al., "Broadband polarization independent nanophotonic coupler for silicon waveguides with ultra-high efficiency," EN, *Opt. Express, OE*, vol. 23, no. 17, pp. 22 553–22 563, Aug. 2015, ISSN: 1094-4087. DOI: 10.1364/OE.23.022553 Accessed: Aug. 20, 2025. [Online]. Available: https://opg.optica.org/oe/abstract.cfm?uri=oe-23-17-22553

[58] W. Bogaerts et al., "Silicon microring resonators," *Laser & Photonics Reviews*, vol. 6, no. 1, pp. 47–73, 2012. DOI: https://doi.org/10.1002/lpor.201100017 [Online]. Available: https://onlinelibrary.wiley.com/doi/abs/10.1002/lpor.201100017

[59] P. Trocha, J. Gärtner, P. Marin-Palomo, W. Freude, W. Reichel, and C. Koos, "Analysis of Kerr comb generation in silicon microresonators under the influence of two-photon absorption and fast free-carrier dynamics," *Phys. Rev. A*, vol. 103, no. 6, p. 063 515, Jun. 2021. DOI: 10.1103/PhysRevA.103.063515 Accessed: Jun. 18, 2026. [Online]. Available: https://link.aps.org/doi/10.1103/PhysRevA.103.063515